Fabian Gsodam, BSc

Dynamic recrystallization of AISI 304L stainless steel during hot plastic deformation

MASTER'S THESIS

to achieve the university degree of

Diplom-Ingenieur

Master's degree programm:
Advanced Materials Science

submitted to
Graz University of Technology

Supervisor
Assoc.Prof. Dipl.-Ing. Dr.techn. Norbert Enzinger
Institute of Material Science, Joining and Forming

Co-Supervisor
Wang, Peng, M.Eng. PhD

Graz, 07.2024

AFFIDAVIT

I declare that I have authored this thesis independently, that I have not used other than the declared sources/resources, and that I have explicitly indicated all material which has been quoted either literally or by content from the sources used. The text document uploaded to TUGRAZonline is identical to the present master‘s thesis dissertation.

_____	_____
Datum / Date	Unterschrift / Signature

Acknowledgement

I would like to extend my deepest gratitude to the supervisor of this thesis, Professor Norbert Enzinger, as well as the co-supervisor Peng Wang and Professor Cecilia Poletti. Their unwavering patience, invaluable advice, and exceptional guidance were crucial for the successful completion of this work.

Further I want to thank the entire IMAT laboratory staff for their support.

A special thank you goes to my family, who always believed in me and supported me in every situation. Their love and faith in my abilities provided me with the strength needed to achieve this goal.

Finally, I would also like to thank my friends. Their open ears, their encouragement and their constant motivation gave me the drive to persevere even in difficult times.

Abstract

The thesis investigates the effect of hot plastic deformation on the microstructure evolution of an austenitic stainless steel (AISI 304L). The focus of the investigation was on the δ-ferrite content and shape as well as the grain size and the hardness of hot deformed samples. It serves as input for a simulation of a thermomechanical welding process (TMW) in which a weld seam is hammered shortly after TIG-welding.

In order to experimentally simulate this process, the AISI 304L steel was melted using the electron beam welding technique to get similar proportions of δ-ferrite for the as-TIG-welded microstructure. 30 as welded samples were hot compressed at strain rates (STR) between 0.001 s^{-1} and 10 s^{-1} and temperatures between 800°C and 1100°C using the Gleeble-3800 simulator. In order to get the isothermal stress, adiabatical heating correction was performed on the experimental flow stresses.

The samples were investigated using a Light Optical Microscope (LOM) to characterize the microstructure. Wet etching with the Beraha II etchant was used for δ-ferrite while nitric acid with a concentration of 60% HNO_3 and 40% H_2O was used as etchant by electrolytic etching to evaluate the grain size.

The δ-ferrite fraction and the aspect ratio have been determined using image analysis. However, this analysis method was only useful for samples that were hot compressed at a low strain rate or high temperatures, as the image and etching quality deteriorated significantly due to the fine δ-ferrite needles and the difficult etching method. Additionally, the δ-ferrite fraction was measured using a feritoscope. The values for the δ-ferrite fraction matched at low strain rates and high temperatures. The results show that the δ-ferrite fraction decreased with increasing deformation temperature at low strain rates (≤ 0.01 s^{-1}) and with decreasing strain rate at high temperatures (≥ 1000°C) which is attributed to the dissolution of δ-ferrite. The aspect ratio of δ-ferrite became smaller due to globularization at high temperatures and low strain rates. Also, average grain size was analyzed. The related results show that grains with large average grain sizes were found on the samples deformed at low strain rates (≤ 0.01 s^{-1}). and high temperatures (≥ 1000°C) due to significant dynamic recrystallization.

The new grains were clearly noticeable at high temperatures and high strain rates (≥ 1000°C) as well as at low temperatures and low strain rates (≤ 0,01 s^{-1}). At these settings, it was also observed that not the entire surface in the observed area is recrystallized, which indicates that a deformation temperature below 900°C is not sufficient for recrystallization to occur. It can also be seen that at high strain rates (≥ 1 s^{-1}) the compression speed leads to an incompletely recrystallized microstructure. Due to insufficient temperature and high strain rates (T ≤ 950°C, str ≥ 0.1 s^{-1}), the recrystallized grains were hardly visible at several hot compression parameters, which meant that not all values for the average grain size could be determined

using the image analysis method. To obtain these values, an electron backscatter diffraction would have to be carried out. However, this is outside the scope of this work.

The hardness of the hot compressed area of the sample was also investigated by Vickers hardness. The results show that the average hardness is decreasing for deformed samples at decreasing strain rates and increasing temperatures, which was correlated to the profound dynamic recrystallization at such deformation conditions. Due to the work hardening-effect which is increasing with decreasing deformation temperatures and increasing strain rates also the hardness was increasing.

This investigation could provide the database for modeling the microstructure evolution of TMW of austenitic stainless steels and summarize the dynamic recrystallization phenomena of as-welded austenitic stainless steels.

Contents

1. Background

In order to obtain a high-quality microstructure a new welding method, Thermomechanical Welding (TMW), was researched. This welding-process includes TIG-welding followed by hammering of the weld seam during cooling as visualized in Figure 1

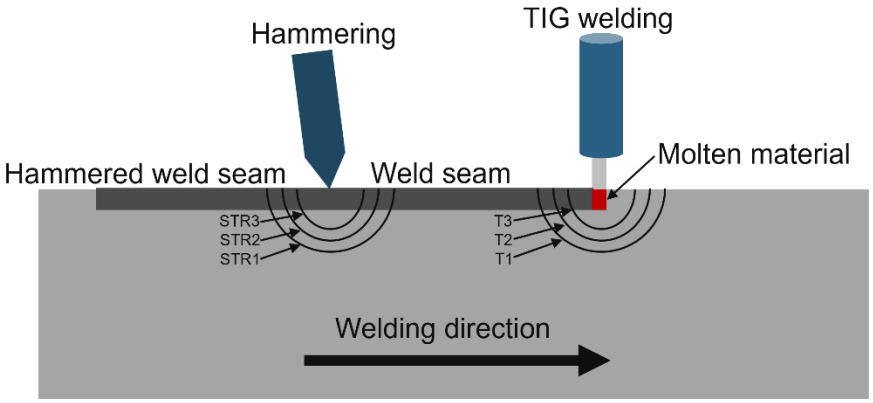

Figure 1: Illustration of TMW

To numerically simulate the welding and hammering, data about the δ-ferrite content and morphology, hardness, and the average grain size are necessary. Figure 1 shows the set-up of TMW, the thermal effect of welding and the effect of hammering in semicircles. Different temperatures occur in different regions during welding. Also, different strains and strain rates are present in different regions around the hammered and post-weld cooling zone. Hammering at elevated temperatures leads to dynamic recrystallization of the microstructure, whereby new strain-free grains are formed. This process varies depending on the temperature and strain rate, which must be taken into account in the numerical simulation. As the molten metal cools, δ-ferrite is formed. Slow cooling leads to dissolution of the δ-ferrite phase into the austenitic phase. The morphology changes from a dendritic, vermicular shape to a globularized shape. This change must also be determined in different regions and should be used as input for the numerical simulation. Due to work hardening by hammering on the weld seam and competing dynamic recrystallization, as well as different δ-ferrite contents in the different affected regions also the hardness changes.

To simulate this process hot compression tests at temperatures between 800°C and 1100°C and strain rates between 0.001 s^{-1} and 10 s^{-1} are carried out on previously EBW treated samples. The applied parameters during the experiment allow different areas around the welded and hammered zone to be analyzed.

2. State of the art

Static and dynamic recrystallization processes are discussed in this chapter. Additionally, nucleation and growth processes during recrystallization are addressed. The background of δ-ferrite evolution as well as the properties of electron beam welding are also covered

2.1. Recrystallization

Recrystallization is a process where new strain free grains are forming at elevated temperatures. These new strain free grains grow by consuming the deformed or recovered microstructure [1].

It is distinguished between primary recrystallization and secondary recrystallization. With primary recrystallization normal grain growth appears whereas abnormal grain growth appears in secondary recrystallization. These will be discussed in Chapter “2.4. Grain Growth” [2].

There are five laws recrystallization follows [3].

(i) **A minimum deformation is needed to initiate recrystallization**. A certain amount of energy is needed to build a nucleus and sustain growth.

(ii) **The temperature at which recrystallization occurs decreases as the holding time at elevated temperatures increases.** Microscopic mechanism which controls recrystallization are thermally activated processes.

(iii) **Temperature at which recrystallization occurs decreases as strain increases.** The driving force for recrystallization is the stored energy. The higher the strain the higher the stored energy. The higher deformed a material is, the lower the temperature must be for the nucleation and growth process.

(iv) **The recrystallized grain size depends primarily on the amount of deformation, being smaller for larger amounts of deformation**. As already mentioned, nucleation and therefore the number of nuclei depends on the strain in the material. Further, for the growth rate of the grains strain is necessary. The nucleation rate and also the number of nuclei is more affected by the strain then the growth rate. Therefore, a higher strain leads to more nuclei resulting in more smaller grains.

(v) **For a given amount of deformation the recrystallization temperatures will be increased by:**

a. A larger starting grain size

Nucleation occurs preferred at grain boundaries. The higher the initial grain size, the fewer sites for nucleation are provided. This leads to a lowered nucleation rate and therefore recrystallization or recrystallization occurs at higher temperatures.

b. A higher deformation temperature

Due to higher temperatures during deformation dynamic recovery has a higher impact on the stored energy. At materials with similar strains and lower deformation temperatures the stored energy would be higher [1].

2.2. Nucleation

Nuclei are small volumes which are pre-existing in deformed microstructures.

The number of nuclei per unit volume (N) is not constant. Therefore, the nucleation rate ($\dot{N}$) must be considered.

$$\dot{N} = \frac{dN}{dt} \tag{1}$$

For single phase metals three nucleation mechanisms are proposed. These are shown schematically in Figure 5.

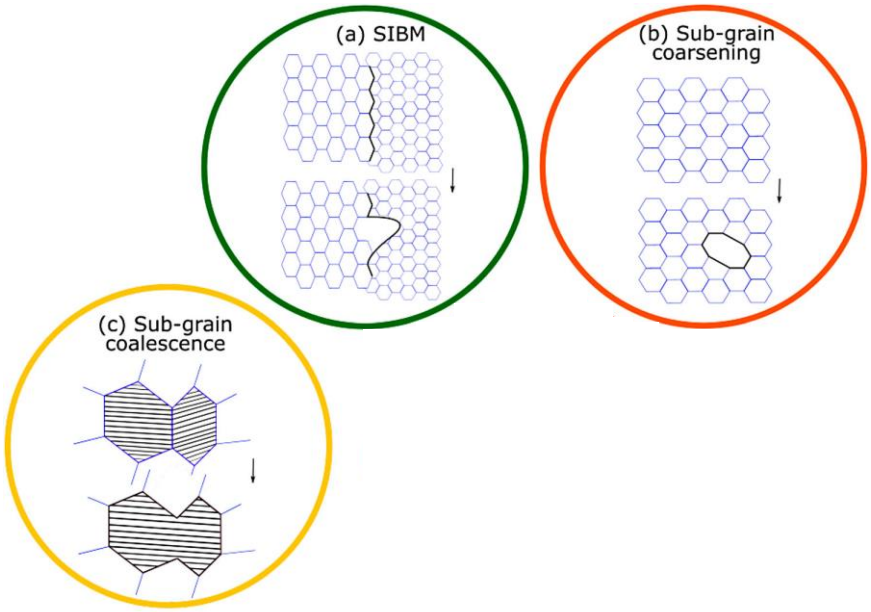

Figure 2: Nucleation mechanisms [4]

(a) Strain induced boundary migration (SIBM)

A high angle grain boundary migrates into neighboring grain and thereby a new strain free region is created. During the deformation strain was built up on each side of the boundary. This induces the migration of the high angle grain boundary.

This mechanism only occurs if the strain difference between the adjacent deformed grains is large. Due to the movement of the boundaries the defects and dislocations are eliminated and the stored energy decreases, while the high angle grain boundary area increases. Figure 5(a) shows the schematic process [4]. This mechanism is assumed to be present as the nucleation process during dynamic recrystallization [1].

(b) Sub grain coarsening

Dislocations are thermally eliminated and relocated, which lowers the stored energy in the material. Sub grain coarsening is thermally assisted migration of low angle boundaries at the expense of neighboring sub-grains as shown in Figure 5(b).

(c) Sub-grain coalescence

Coalescence occurs if two neighboring sub-grains rotate, aligning their crystal lattices with respect to each other as shown in Figure 5 (c) [4].

2.2.1. Static recrystallization

Static recrystallization can occur when an already deformed sample gets annealed [1]. It can be divided in three different mechanisms. Continuous static recrystallization, discontinuous static recrystallization and geometric static recrystallization. (i) During static recovery, the sub-grain structure with low angle grain boundary transforms gradually in a high angle grain boundary structure. This is necessary to form new grains. During this process, continuous rotation of sub-grains as well as a little boundary migration of the sub-grains occurs. This can be labeled continuous static recrystallization. (ii) Static recrystallization can also occur uniformly. If there is also a clear nucleation and growth stage during the nucleation of new strain free grains by migration of high angle grain boundaries the process can be classified as discontinuous static recrystallization. (iii) Geometric static recrystallization was only mentioned for the purpose of completeness. This process is not discussed in detail in this thesis [5].
During static recrystallization, new, almost dislocation-free grains are formed. The new formed grains consume the initial deformed microstructure by forming and migration of high angle grain boundaries [6].
With the Avrami Equation (JMAK) developed by Johnson and Mehl, Avrami and Kolmogorov, the kinetics of static recrystallization of cold worked metals and alloys can be shown.

$$F = 1 - e^{[-B*t^k]} \tag{2}$$

where F is the volume fraction recrystallized, t is the time, and B and k are the model-dependent constants [7].

2.2.2. Dynamic recrystallization

There are several types of dynamic recrystallization occurring in different thermo-mechanical processes (TMP). We distinguish between Discontinuous Dynamic Recrystallization (DDRX), Continuous Dynamic Recrystallization (CDRX) and Geometric Dynamic Recrystallization (GDRX). Although the subject GDRX is not dealt with in this thesis and is just mentioned for the sake of completeness [8]

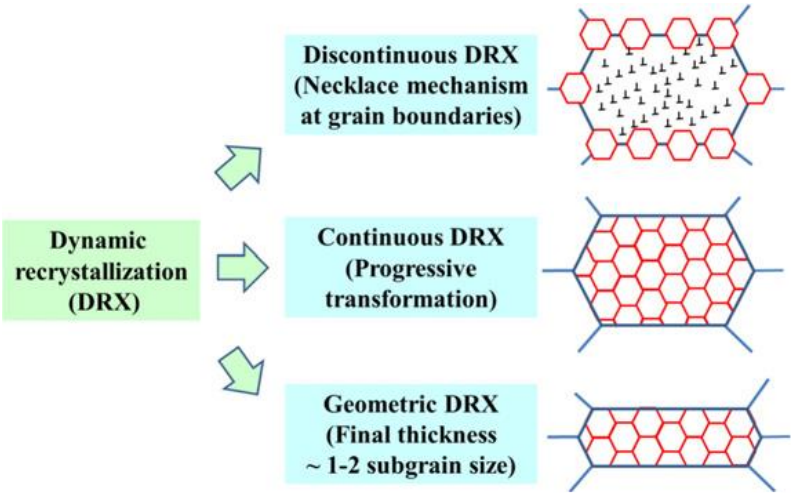

Figure 3: Types of Dynamic recrystallization [8]

Metallic parts are often processed during their life cycle. Especially hot deformation is used to deform a metal at elevated temperatures. During and after the hot deformation, recovery, recrystallization, and grain growth takes place. Also, the number of dislocations and so the dislocation density grows with growing deformation of the material. These defects are accumulating in cells with less defects, surrounded by cell boundaries. In a larger scale the defects are subdivided by the grain boundaries. This results in an increase of stored energy due to the defects and dislocations introduced due to the deformations of the material.

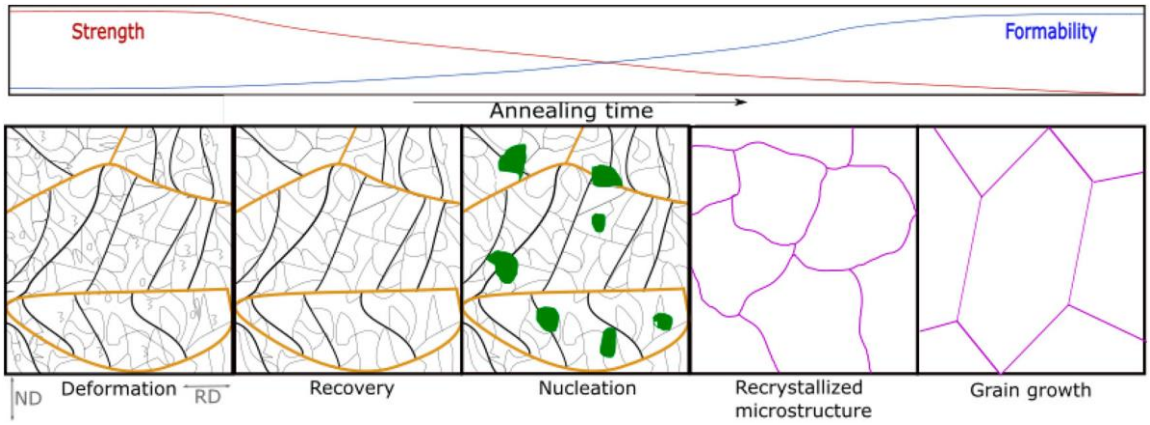

Figure 4: Kinetics of dynamic recrystallization [4]

As Figure 4 shows the dislocations as well as the defects are getting less during recovery. These defects are getting annihilated and rearranged forming sub grain boundaries. During or after the deformation or recovery which slows recrystallization down, the metal can recrystallize, forming new nuclei at different sites with a strain- and defect free crystal lattice. When the nuclei have a critical size, the boundary will migrate, and the former microstructure gets eventually replaced by the recrystallized microstructure [4].

Factors that have an effect on DRX are the initial grain size, stacking fault energy (SFE), the thermo-mechanical processing (TMP) conditions, chemistry, micro chemistry of the material, etc. There is no clear separation between the different dynamic recrystallization processes [8].

2.2.2.1. Continuous dynamic recrystallization (CDRX)

Continuous dynamic recrystallization appears at materials with high stacking fault energy γ_{SFE}. High angle grain boundaries may be formed during deformation by the progressive rotation of sub-grains. The microstructure of the material develops relatively homogeneously over the entire material. At continuous dynamic recrystallization, no noticeable nucleation and growth can be observed on the recrystallized grains.

Strong deformation of the material is required to initiate or perform CDRX [8]. These conditions can often only be created using special equipment.

The main characteristics are shown in the following points:

- Stress increases with the strain of the material. A steady state stress is achieved with large strains. This steady state stress increases with higher strain rate and is independent of the initial grain size.
- Increasing strain leads to increasing sub-grain boundary misorientation.
- The low angle grain Boundaries transform into high angle grain boundaries. During this transformation, the misorientation increases homogeneously.
- The size of the crystallite decreases, as deformation increases

Initially, the CDRX may take place as low angle grain boundaries form from dislocations generated within the grain. As the material undergoes sustained stress, the misorientation angle gradually rises until it reaches the critical angle, resulting in the formation of a high angle grain boundary.

Also, CDRX can occur due to sub-grain rotation recrystallization. The misorientation angle is increasing because of the rotation of the sub-grains. When the misorientation angle is large enough, the previous sub-grain counts as an independent grain.

A third mechanism of continuous dynamic recrystallization is the CDRX by deformation caused by micro shear bands. Sub-grains are formed through dislocations within the grain during work hardening. If micro shear bands are created in the grains, the misorientation of low angle grain boundaries increases very quickly, as the micro shear bands introduce stress into the system. This transforms them into high angle grain boundaries [8].

2.2.2.2. Discontinuous dynamic recrystallization

Usually, materials with low stacking fault energy (SFE) follow the discontinuous dynamic recrystallization process during hot deformation. For these materials, the stacking faults are wider, which make cross slip and climb of dislocations more difficult and hinders dynamic recovery. AISI 304L which is investigated in this thesis is also a low stacking fault material. During the process new strain-free grains occur and grow at the expense of regions which have a lot of dislocations [9]. The process happens at temperatures above half the melting temperature of the materials [6]. The melting temperature of AISI 304L is at 1450°C [10].

A stress-strain diagram is used to show the different steps of dynamic recrystallization in Figure 5 (a). This is divided into several stages.

In Stage I, the accumulation of dislocations caused by hot compression, work hardening plays the major role in this stage alongside recovery (σ_{DRV}). Whereby recovery leads to softening [9]. Work hardening takes place, when a metal is plastically deformed. This leads to an increased formation of dislocations. These dislocations interact with each other and become tangled or pinned. As a result, the dislocations can no longer move, which increases the strength of the metal [9]. From point (σ_c, ε_c) onwards (stage II), also dynamic recrystallization occurs. The stress continues to increase until a peak is reached (σ_p). After the peak, in stage II there is a competition between softening by recrystallization and work hardening. From the diagram you can see that the dynamic recrystallization (σ_{DRX}-curve) has a higher impact on the flow stress than dynamic recovery (σ_{DRV}-curve) [9]. Dynamic recovery is not very significant, as discontinuous dynamic recrystallisation mainly occurs with low stacking fault materials [9]. In stage 3, a steady state is reached where recrystallization and work hardening balance each other out (σ_{ss}, ε_{ss}). The diagram also shows how the different softening mechanisms influence the stress-strain curve. The flow stress curves shape changes with temperature and strain rate. The steady state flow stress decreases with decreasing strain rate [6].

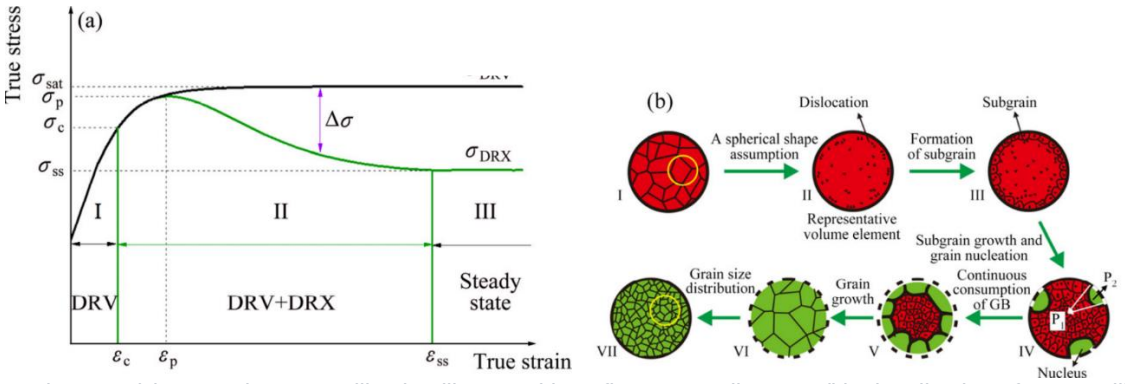

Figure 5: (a) Dynamic recrystallization illustrated by a flow stress diagram, (b) Visualization of recrystallization during hot compression [8]

Figure 5 (b) shows the process of dynamic recrystallization during hot deformation.

In step I, a grain of the microstructure is selected to be investigated.

In step II, only this grain is displayed. Due to the increasing deformation of the material at elevated temperatures, the dislocation density increases. These are displayed as black symbols. Due to the increasing dislocation density, sub-grains form at the grain boundary of the examined grain in step III. If these grow to the critical size of the recrystallized nuclei, dynamic recrystallization occurs. The nuclei form at the grain boundaries and then spread into the interior of the preexisting grain, as can be seen in step IV [9]. Thereby a necklace structure of the new formed grains can be observed if there is a large difference between the initial grain size and the recrystallized grains [8]. The grain boundaries are consumed, and the nuclei grow

until the entire observed system is covered by new grains. These steps are shown in steps V, VI and VII [9].

In general, discontinuous dynamic recrystallization occurs, with low stacking fault materials like AISI 304L when a high amount of deformation is reached. New strain free grains are formed during the process whereby the neighboring grains are consumed in the process. This is due to the difference in stored energy or dislocation density.

2.3. Grain Growth

This chapter discusses grain growth in dynamic and static recrystallization.

2.3.1. Grain growth during DRX

During deformation, new grains form at the previously existing grain boundaries. Further deformation of the material further increases the dislocation density of the new grains. This process reduces further grain growth. In addition, the nucleation of further grains at the migrating boundaries limits growth. The size of dynamically recrystallized grains increases monotonically with decreasing stress. In comparison with SRX, the grain size of dynamically recrystallized grains does not change as recrystallization proceeds. [1]

2.3.2. Grain growth during SRX

After the recrystallization process the microstructure is not stable. By reducing the grain boundary area due to continued annealing the energy of the system can be further decreased in the grain grow process. Two different types of grain growth can occur in AISI 304L:

- **Normal grain growth**

In normal grain growth the grains growth uniform. They maintain their grain size distribution [6]. The grain growth occurs by annihilation of smaller grains which results in grain boundary migration.

- **Abnormal grain growth or secondary recrystallization**

If normal grain growth is hindered, abnormal grain growth often occurs. It is characterized by bimodal grain size distribution, which is due to rapid grain growth [12]. Abnormal grain growth only takes place when the size of the growing grain is already large. Prerequisites and postulates are based on advantageous texture, grain boundary mobility, enhanced diffusion kinetics, and coalescence [2].

The growth process of new grains is well analyzed. The velocity (v) of a high angle grain boundary is also called the growth rate (G). It is given by the equation:

$$v = G = MP \tag{3}$$

Where (M) is the boundary mobility and (P) is the net pressure on the boundary [1].

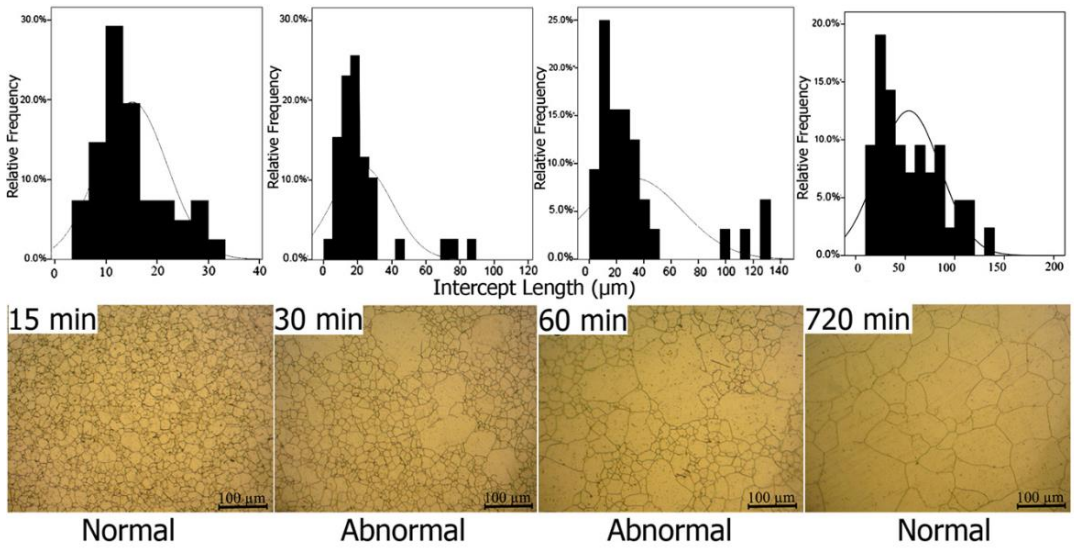

Figure 6: Normal and abnormal grain growth of AISI304L at 900°C at different time frames [12]

Figure 6 shows images and histograms of the grains of AISI 304L annealed at 900°C over different timeframes. The study shows that until 15 minutes normal grain growth occurs. At 30 minutes the abnormal grain grow is stronger. Also, at 60 minutes abnormal grain growth was present. The histogram shows the bimodality of the grains. After 720 minutes of annealing again normal grain growth mode was present [12].

2.4. δ-Ferrite evolution

Austenitic stainless steels solidify with the evolution of δ-ferrite [13]. The chemical composition plays a major role in the δ-ferrite formation. δ-ferrite stabilizer such as molybdenum and chromium promote the formation of the phase during solidification [14]. δ-ferrite has a body centered cubic microstructure [13]. The microstructure of AISI 316L shows about 6-10% δ-ferrite after TIG-welding of AISI 316L [15]. In general, δ-ferrite has a negative effect on the high temperature workability and the corrosion resistance. Also, the ferromagnetic behavior of the FCC δ-ferrite might have a negative effect on the material properties. On the other hand, a certain amount of δ-ferrite must be present to prevent hot cracking [16]. Also, δ-ferrite in austenitic stainless steel promotes nucleation sites in the interface between the δ-ferrite phase and the austenitic phase [17].

However, in AISI 304 austenitic stainless steels, δ-ferrite should be completely transformed into γ-austenite at temperatures below 1200°C during hot compression. In castings, welded parts, and forged parts made of austenitic stainless steels, δ-ferrite can remain as part of the microstructure due to rapid cooling [13].

The properties of austenitic stainless steel are closely linked to its microstructure and phases. Phase transformation between δ-ferrite and γ-austenite in austenitic stainless steels is an important process that affects the mechanical properties and corrosion resistance of the

material. Therefore, the dissolution of the δ-ferrite phase is necessary to get a lower volume fraction. The dissolution can be split into two different stages. In the first step, rapid dissolution of the δ-ferrite occurs through the precipitation of M23C6 carbides. The formation of these carbides decomposes the δ-ferrite phase. This could be observed at samples deformed at temperatures between 500°C and 900°C. When an austenitic stainless steel is heated, the δ-ferrite content also changes. The volume fraction becomes smaller if the material is exposed to a high temperature for a longer time [18]. The highest decrease in δ-ferrite in the structure of AISI 304L stainless steel occurs at the beginning of the exposure. After that, the decrease in δ-ferrite decreases again [16].

With a further increase in temperature, the carbides also dissolve simultaneously with the δ-ferrite grains. The morphology of the δ-ferrite phase also changes due to the energy acting on the microstructure as a result of the high temperatures. The volume fraction is reduced, and the phase becomes rounder [19].

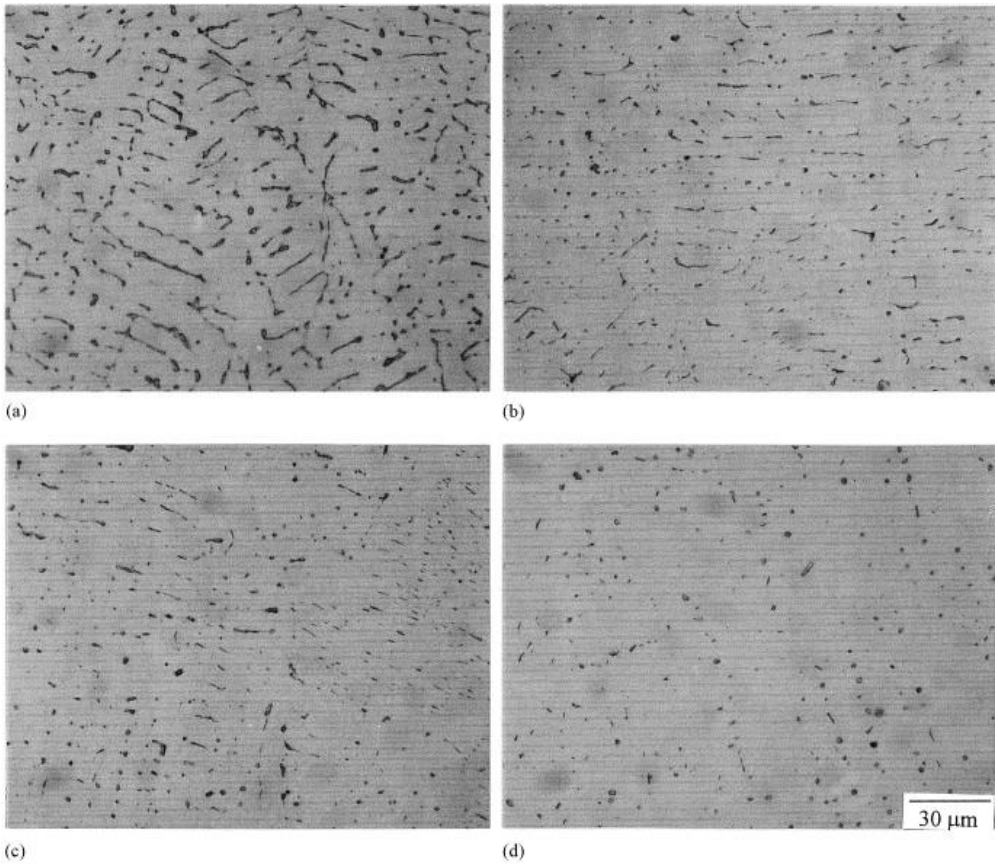

Figure 7: Evolution of δ-ferrite in an AISI 304 stainless steel at a temperature of 1150°C over time a) As cast b) 60 s c) 100 s d) 225 s [15]

Figure 7 shows the evolution of δ-ferrite in an AISI 304 steel over time at a temperature of 1150°C. It can be seen that the δ-ferrite content gradually decreases over time. Also, the geometry of the δ-ferrite changes as expected over time. There are larger δ-ferrite phases when exposed for shorter times. The walls which are visible are thinned until they are completely dissolved into the austenitic phase. At 225 s exposure time the globularized δ-ferrite is visible [16].

2.5. Electron beam welding (EBW)

Electron beam welding is a fusion welding process, as the metal-to-metal joint happens in a molten or liquid state. It has a narrow fusion zone in contrast to TIG or arc welding. This has the advantage that less metal is melted, resulting in less distortion and less heat during the welding process. Several parameters must be considered when carrying out the welding process. These include the Depth of Penetration, Accelerating voltage, Beam Current, Welding speed and more. The chemical properties of the material to be welded and the thickness of the material also play an important role [20].

Electron beams are generated by an electron gun with a power of max. 100 kW. A filament is heated with a high voltage of about 10-200 kV. The electrons leave the filament and get accelerated towards the sample surface with high speed. After leaving the electron gun, the beam is focused on the weld joint via a magnetic lens system. During electron beam-workpiece interaction, the radius of the beam varies between 0.1 mm and 0.8 mm [21].

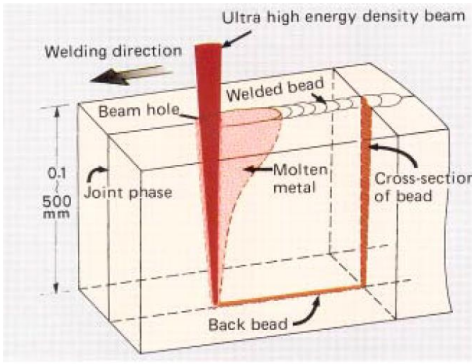

(a) EBW welding (Key-hole effect) [22]

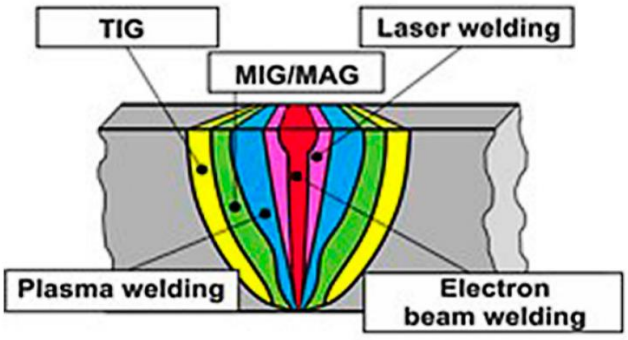

(b) Weld zone of different welding methods [23]

Figure 8: EBW welding (key hole effect), (b) Weld zone of different welding methods

During the workpiece-electron interaction, the material is vaporized due to the high-energy-density-electron beam which is shown in Figure 8 (a). The key-hole effect occurs. This effect describes the deep penetration of the electron beam into the workpiece where a narrow weld occurs. This results in a small heat affected zone [22]. Figure 8 (b) compares different welding methods.

3. Objective of the work

An austenitic chromium nickel stainless steel AISI 304L with low carbon content was chosen for this investigation. The as received material was remelted using electron beam welding to obtain as solidified microstructure representing an as welded condition. The parameters for the following hot compression tests were determined on the basis of a numerical simulation carried out beforehand. Based on this data, the tests were carried out at temperatures between 800°C and 1100°C and at strain rates between 0.001 s^{-1} and 10 s^{-1}. A target strain of 0.7 was found.

Hot compression at different temperatures and strain rates leads to different microstructural changes. During hot compression work hardening and competing recrystallization leads to a characteristic flow curve as a result of the hot compression test. These parameter dependent flow curves should be analyzed. For a proper evaluation, also adiabatic heating during the deformation has to be considered. Therefore, adiabatic heating correction was applied.

During cooling after EBW-welding, δ-ferrite is formed which changes the properties of the microstructure. Different hot compression parameters affect the δ-ferrite content. If the material is exposed to high temperatures for a longer period of time, dissolution and globularization of the δ-ferrite phase into the gamma austenite phase occurs. The phase fractions, aspect ratios and the dissolution and globularization of the δ-ferrite phase must be analyzed and interpreted.

During hot compression dynamic recrystallization occurs. New strain free grains are formed, and a softening of the microstructure can be observed. As it strongly depends on the temperature and strain rate during deformation, where a higher temperature leads to increasing recrystallization, the grain size at different hot compression parameters should be determined. The Vickers hardness of the hot compressed samples is determined.

The data from the experiments will be used as input for the TMW simulation.

The aim of the thesis can be summarized as follows:

I. Flow stress curves

- Creation of adiabatically corrected flow stress curves
- Identify the effects of work hardening and recrystallization during hot compression

II. Delta ferrite

- Find and interpret the δ-ferrite fraction evolution at different hot compression parameters
    - By feritoscope and by image analysis method
- Determine and interpret the change in aspect ratio of the δ-ferrite phase at different hot compression parameters
    - By image analysis method
- Analyze the dissolution and globularization of the δ-ferrite phase

III. Average grain size

- Determination of the average grain size after hot compression at different temperatures and strain rates.
    - By image analysis method
- Determination of the Vickers hardness after hot compression at different temperatures and strain rates.

4. Experimental methodology

This chapter describes how the as received material was processed and analyzed in order to obtain the results of interest. The hot compression test and sample preparation for metallographic preparations are discussed. In addition, the etching methods are examined and the evaluation techniques for the δ-ferrite measurements as well as the average grain size and hardness are explained.

4.1. Sample preparation for hot compression

In order to simulate the microstructure of the samples after the TIG welding process during TMW, the starting material, which was an austenitic stainless steel AISI 304L block was melted using the electron beam welding process. Both the δ-ferrite fraction and the average grain size should be similar to the TIG welded microstructure in as weld condition.

The cutting was carried out via electron discharge machining. Whereby the samples were cut from different positions of the weld seam. During electron discharge machining, there is no contact between the electrode and the sample which prevents the occurrence of mechanical stresses and stability problems due to vibrations and noise during processing [24].

4.2. Hot compression by Gleeble 3800 simulator

Hot compression tests were carried out by a Gleeble-3800 simulator. This Module is shown in Figure 9.

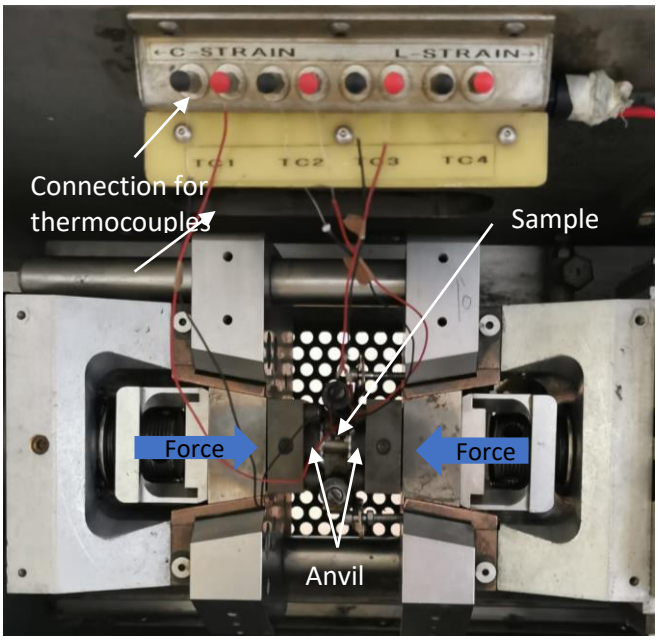

Figure 9: Gleeble simulator chamber

This made it possible to precisely define the temperature curve for the experiment. Resistance heating is used by the simulator to heat up the samples to the intended deformation temperature. Furthermore, uniform deformation could be ensured by compressing the cylindric

sample which had a diameter (d) of 8 mm and a height (h) of 12 mm from both sides at defined strain rates and a target strain of 0.7, as both anvils contributed to the compression. A schematic illustration of the initial welded cylindric sample with the specified dimensions could be seen in Figure 10.

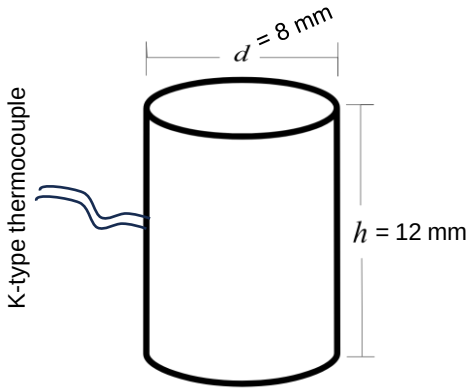

Figure 10: Schematic illustration of the initial cylindric sample before compression

K-type thermocouples were used to measure the temperature during the hot compression test.

4.2.1. Hot compression test

The required parameters and process steps were defined in the "QuickSim2" software. A targe strain of 0.7 was used for the hot compression tests. The temperature was varied between 800°C and 1100°C and the strain rate was varied between 0.001 s-1 and 10 s^{-1}. In the first step, both ends of the cylindrical samples with a diameter of 8 mm and a height of 12 mm were slightly ground to remove corrosion and the thermocouples were spot-welded to the workpiece to get a good temperature measurement. In order to decrease large friction influence, molybdenum sheets were glued to the workpiece using nickel paste. Now the sample could be carefully clamped between the anvils in the Gleeble-3800 simulator. The cover of the machine was closed, and the vacuum was activated. After reaching the maximum vacuum possible, the chamber was filled with argon gas. For the control of the length change the L-gauge was used and for the control of the piston movement the stroke. The simulation was started, and the previously defined simulation steps were executed. The steps involved heating and holding the sample at 25°C for a defined time to make sure it has a homogeneously well-defined temperature at the beginning of the heating step. Subsequently the temperature was increased at a certain heating rate. After that, the sample was held for a certain time to get a homogeneous temperature in the sample. Now the hot compression was carried out at different strain rates and temperatures. After the hot compression, the samples got immediately quenched with water. Now the chamber was ventilated, and the sample could be removed. The thermocouples were removed, and the new dimensions were taken from the hot compressed sample.

Table 1: Hot compression test matrix

Strain rate [s^{-1}]	800°C	850°C	900°C	950°C	1000°C	1100°C
0.001	Sample 37	Sample 33	Sample 34	Sample 35	Sample 36	Sample 52
0.01	Sample 14	Sample 15	Sample 17	Sample 18	Sample 19	Sample 49
0.1	Sample 25	Sample 24	Sample 23	Sample 22	Sample 21	Sample 48
1	Sample 26	Sample 56	Sample 29	Sample 28	Sample 30	Sample 46
10	Sample 39	Sample 53	Sample 41	Sample 42	Sample 44	Sample 45

Table 1 shows which sample was hot compressed at which temperature and at which strain rate. The different parameters during deformation change the microstructure and the phase composition of it. This change should be investigated as part of the work.

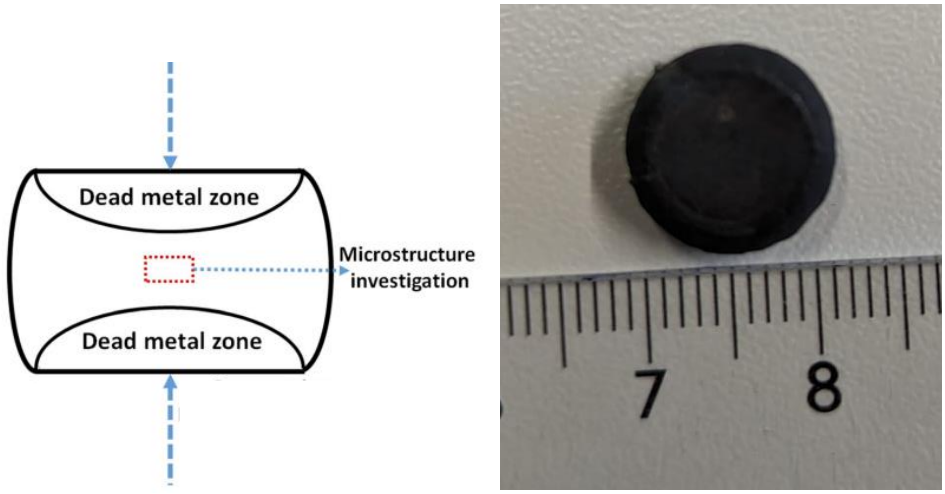

(a) (b)

Figure 11: (a) Schematic illustration of the regions of interest of the deformed [25]*, (b) Hot compressed sample*

Figure 11 (a) shows the zone of interest. The samples were investigated in the area shown in red rectangle, as this is where the highest deformation is found after the hot compression test [25]. Figure 11 (b) shows the hot actual compressed sample, after the hot compression test.

4.2.2. Adiabatic heating correction of flow stress

The deformation that occurs during the hot compression test heats up the alloy due to plastic work. As a result of that, the flow stress curves after hot compression are lower than the flow stress under isothermal conditions [26]. At low strain rates (≤ 0.01 s^{-1}), the material has enough time during deformation to transfer the heat from inside of the material to the outside during the compression and therefore it can be seen as isothermal [27].

At high strain rates, there is not enough time to dissipate the heat. This leads in a higher adiabatic heating in the material when compressed at higher strain rates, which has to be considered.

The adiabatic correction factor is calculated using the following formula:

$$\Delta T = \frac{0.95\eta \int_0^{\varepsilon} \sigma d\varepsilon}{\rho Cp} \quad (4)$$

Whereby ΔT is the temperature difference in °C between the initial measured curve and the corrected curve, η is the adiabatic correction parameter; σ is the stress (MPa), ε is the strain, $\int_0^{\varepsilon} \sigma d\varepsilon$ provides the area under the uncorrected curve, ρ is the density of the material (g/cm^3) and Cp is the specific heat (J·g^{-1}·°C^{-1}) [28].

4.2.3. Work hardening rate

The mechanical properties of stainless steels change with work hardening. Work hardening leads to hard and brittle materials [29]. Further, it promotes a growth of the dislocation density in a material during deformation. Figure 5 shows the critical stress (σ_c) and critical strain (ε_c). This value gives the upper limit of the amount of energy that can be stored within the hot deformed material [30].

The work hardening rate can be calculated by:

$$\theta = \left.\frac{d\sigma}{d\varepsilon}\right|_{T,\dot{\varepsilon}} \quad (5)$$

Whereby θ is the work hardening rate, σ is the true stress and ε which gives the true strain [31]. Temperature T, and strain rate $\dot{\varepsilon}$ are constant.

4.3. Microstructure characterization

In order to find the fraction and the ratio of the δ-ferrite phase in the hot compressed samples and also to get the average grainsize of the sample, the sample had to be ground, polished and etched. After the etching, the prepared surface was investigated under the light optical microscope.

In Figure 12 (a) the microstructure of AISI 304L as received is visible. Figure 12 (b) shows the via EBW remelted area of the reference sample which was not hot compressed.

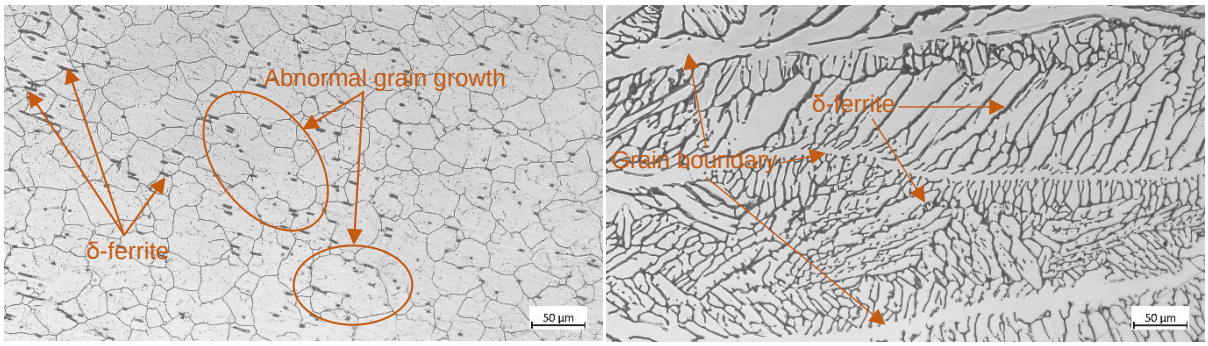

(a) (b)

Figure 12: Comparison between the "as received" microstructure (a) and the EBW-welded microstructure (b) of AISI 304L

In Figure 12 (a) we can see, that abnormal grains are present in the microstructure which is characterized by bimodal grain size distribution, which is due to rapid grain growth. Also, very small δ-ferrite phases are present.

Figure 12 (b) shows the grain boundaries of the large grain in white. The dendritic or vermicular morphology of the δ-ferrite phase can be recognized in the grain. The EBW welding process significantly increased the content of δ-ferrite in the microstructure.

4.3.1. Sample preparation for metallography

After the hot compression test, the samples were cut in half along the compression axis using “Struers Accutom-10” saw. The flash of the sample was removed.

In the next step, they were embedded with the help of the embedding machine "Struers CitoPress-20" which is visible in Figure 13 (a). “Polyfast” was used as the embedding agent. This agent was used because it is electrically conductive, which was necessary for electrolytic etching.

(a) (b)

Figure 13: (a) Struers CitoPress-20 (b) Struers Tegramin-30

In order to be able to identify the workpieces, the workpiece number, the temperature at which the compression took place, and the strain rate were engraved on the back of the embedded sample using the "Signograph 25". For example, the following information was engraved:

T1100°C, STR10, 45. Whereby T1100°C shows the temperature, STR10 the strain rate during hot compression and 45 was the sample number

Now the workpieces were ground and polished. For this a “Struers Tegramin-30” grinding and polishing machine was used which can be seen in Figure 13 (b).

A grit size of 120 was used to remove coarse machining residues. After that the grinding was carried out at a grit size of 220. In the last step, a 9 µm grit size was used. There, also a 9 µm diamond suspension was used to get good surface quality.

After each step, the workpieces were cleaned to prevent contamination on the subsequent grinding wheel or polishing cloth. The surface was also inspected for quality with the naked eye.

After the 9 µm grinding step was completed, the workpieces were polished. For this purpose, the grinding wheels were replaced by polishing cloths. During the grinding and polishing the parameters changed according to the surface quality. The most important parameters were the time of the process step and the force which was used to press the sample onto the grinding discs or polishing clothes. Also, the amount of suspension used was varied dependent on the current situation.

In between the grinding step with 9 µm and the polishing step with 3 µm is the largest difference of the size of the grit. This step was therefore carried out with particular care. If scratches could still be seen with the naked eye, the surface quality was not yet good enough. The polishing time here was between 10 minutes and 20 minutes at different forces. Different polishing cloths were also used in the test. It was found that the polishing speed for an optimum surface varied greatly depending on the disc used, although these were designed for the same grain size of 3 µm. The poor-quality discs were removed from the repertoire. After this step, the sample was cleaned, dried and examined under a light microscope. If no scratches over 3 µm were visible, the next polishing step with 1 µm could be applied. Here the 1 µm suspension was used. The time varied between 5 to 10-minutes dependent on the surface after examining it through the light optical microscope.

In the last step OPS was used to get a surface quality, where the largest scratches are below 0.5 µm. This step was carried out for about 1 minute. The samples were cleaned immediately after the polishing step was finished.

After the polishing steps, the samples had a mirror-like appearance. When investigated with the light optical microscope no or very few scratches were visible. Even when the grinding and polishing was carried out very carefully there were always some scratches on the surface. For the tests regions with less or no scratches were used.

4.3.2. Etching

To make different phases of interest visible etching was done. A clean and polished surface was necessary for the process step. To make the δ-ferrite phase visible, color etching was used. To measure the grainsize, the grain boundary had to be etched out. For this, electrolytic etching was done.

4.3.2.1. Electrolytic etching

The grain boundaries were made visible by using electrolytic etching. Technical nitric acid was used for this. This etchant consists of 60% HNO_3 and 40%H_2O [32]. A voltage of 15V was used. The etching time was set to 11 seconds. The flow rate of the etchant during the etching was set to 12. The samples, which were polished until OPS-quality were carefully placed on the cover and connected to the circuit via the machine's extension arm.
The predefined program was started. After 11 seconds, the workpiece was removed, cleaned and inspected under the light microscope.
Different methods were tried to find the optimal etchant for this.

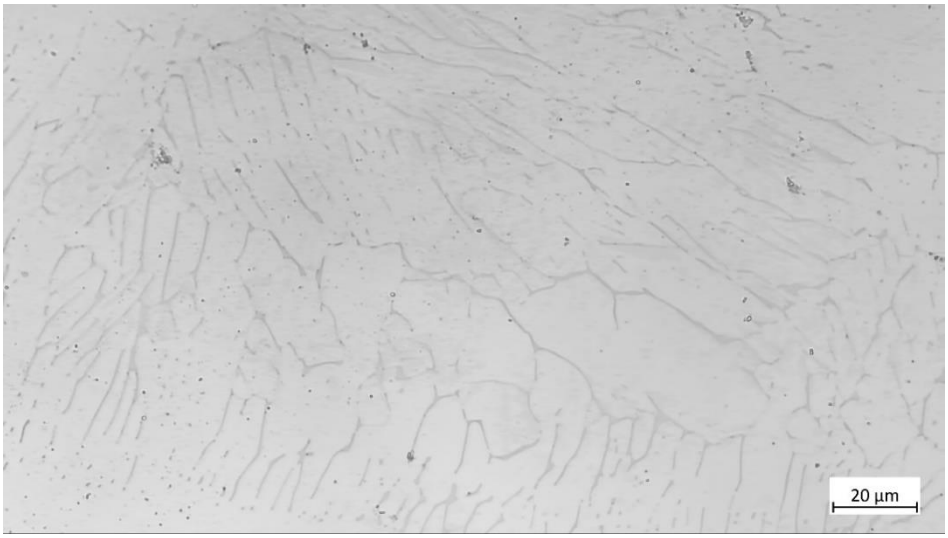

Figure 14: Microstructure of EBW melted AISI 304L austenitic stainless steel after 40% HNO_3, 60%H_2O electrolytic etching

Nitric acid with a concentration of 40% HNO_3 and 60% H_2O was used in the first try. Figure 14 shows the microstructure, where this etchant was used. It was not possible to differentiate between the δ-ferrite phase and the grains in the microstructure. Therefore, this etchant could not be used. In the second step, the concentration was then adjusted to 60% HNO_3 and 40% H_2O.

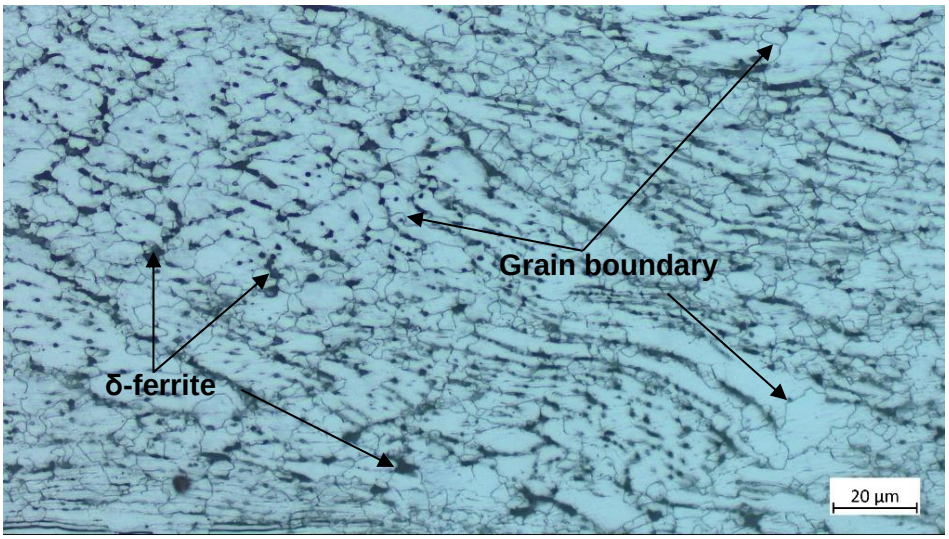

Figure 15: Microstructure of EBW melted AISI 304L austenitic stainless steel after 60%HNO_3 and 40%H_2O electrolytic etching

Here it was possible to clearly distinguish between the δ-ferrite and the grain boundaries at the parameters as visible in Figure 15. The grain boundaries of the recrystallized microstructure could be clearly distinguished from the darker δ-ferrite phase.

4.3.2.2. Color Etching

After grinding and polishing until OPS the samples could be color etched. The goal of this etching was to identify the δ-ferrite phase fraction. Several etching agents were researched in the literature for this purpose. After the process it should be possible to clearly distinguish between the δ-ferrite phase and the other phases present. In a first try Beraha I was used. The microstructure is shown in Figure 16.

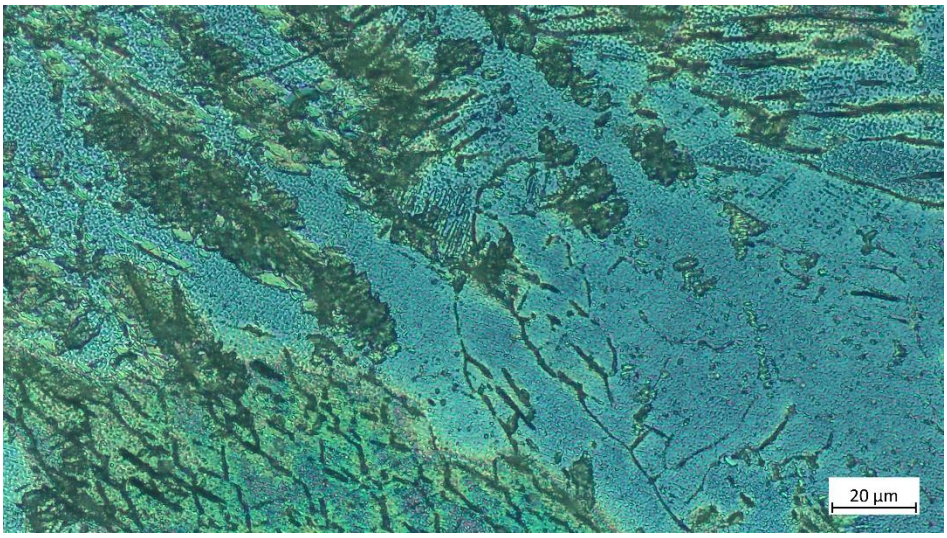

Figure 16: Microstructure of EBW melted AISI 304L austenitic stainless steel after wet etching using Beraha I color etchant

After etching with Beraha I the surface was investigated with the light optical microscope. It was not possible to distinguish δ-ferrite from the other phases. Also, a black layer was visible, which covered parts of the surface. This layer could not be removed by cleaning.
After that an attempt with V2A and Lichtenegger & Bloech was used as etchant where the microstructure can be observed in Figure 17. With this method the sample was electrolytic etched with V2A etchant followed by wet etching with Lichtenegger and Bloech etchant. There the δ-ferrite should have a blueish color [32].

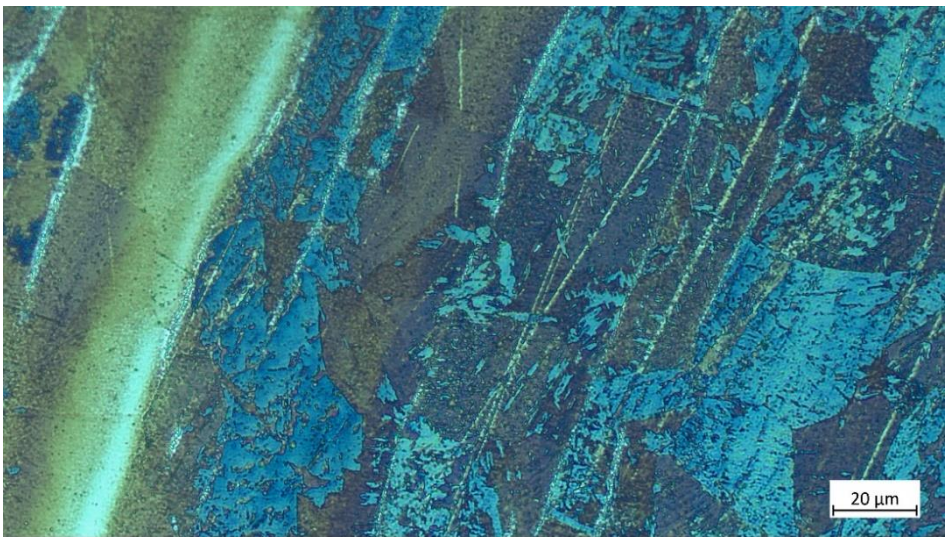

Figure 17: Microstructure of EBW melted AISI 304L austenitic stainless steel after wet etching using V2A and Lichtenegger Bloech color etchant

Unfortunately, no δ-ferrite could be detected here. The blue colored phase was not formed like dendritic or vermicular structure.
Furthermore, Beraha II was tried as an etchant. It consists of a stock solution and additionally a starter chemical. The stock solution consists of 1000 ml distilled water, 400 ml hydrochloric acid 32%ig and 48 g Ammoniumhydrogendifluorid. To start the reaction 1 g potassium disulfite was added while stirring [32]. The sample was submerged in the etchant for several minutes.

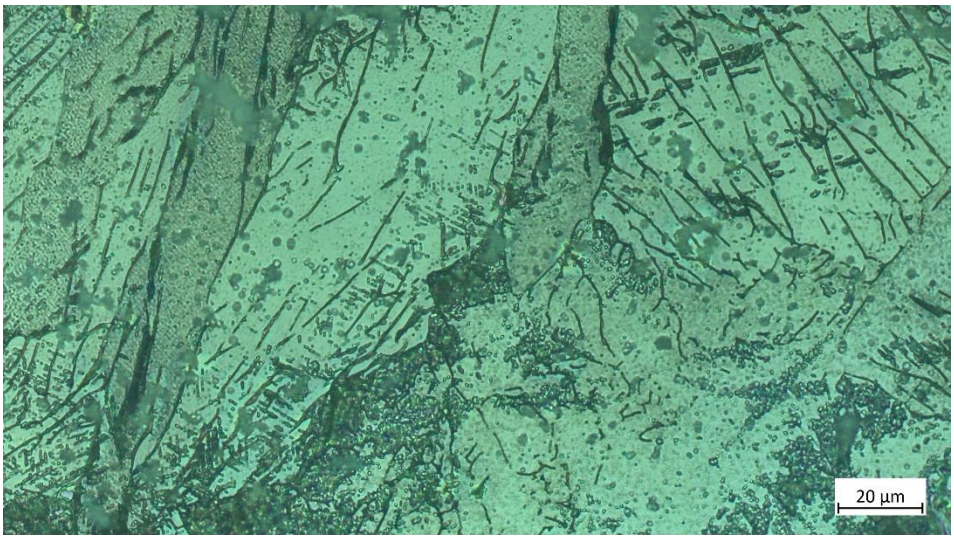

Figure 18: Microstructure of EBW melted AISI 304L austenitic stainless steel after wet etching using Beraha II color etchant (1 g potassium disulfite)

Figure 18 shows, that the δ-ferrite, but also a black layer which partially covers the phase. Unfortunately, it was not possible to remove the black layer by cleaning. To attenuate the etchant and slow down the chemical etching reaction, 0.5 g of potassium disulfite was used as a starter instead of 1 g of potassium disulfite. The sample was also submerged in the etchant for only 5-10 seconds until a blue precipitate was visible in the etching liquid. The etchant was then immediately removed and cleaned.

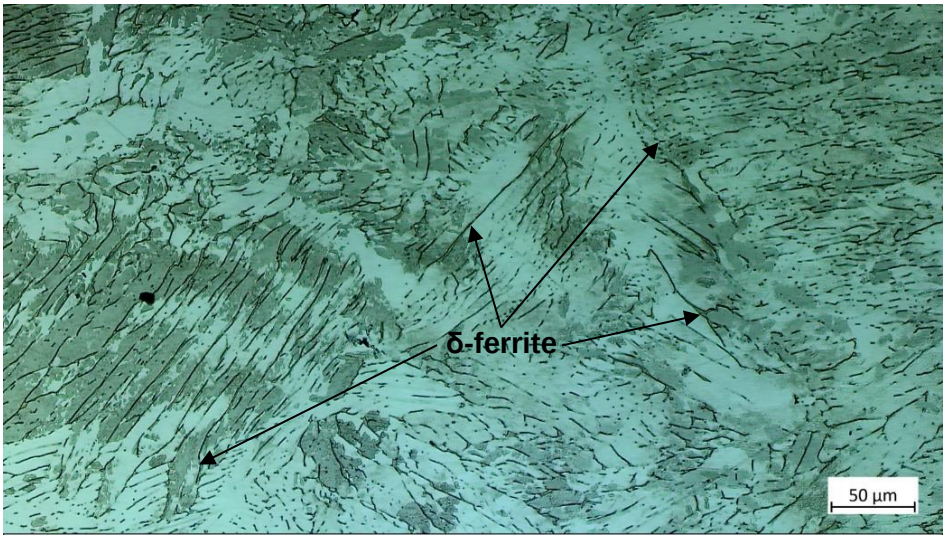

Figure 19: Microstructure of EBW melted AISI 304L austenitic stainless steel after wet etching using Beraha II color etchant (0.5 g potassium disulfite)

As Figure 19 visualizes, the δ-ferrite was now clearly visible and could be distinguished from the other phases when 0.5 g potassium disulfite was used. The resulting images were used to obtain the aspect ratio and the fraction of the δ-ferrite at different temperatures and strain rates.

4.3.3. Grain Size measurement

After the samples had been electrolytically etched with the help of nitric acid 60% HNO_3 and 40% H_2O, the grain size could be determined in the next step. For this purpose, several images were taken with a high magnification of X500 to X1000. It was important to ensure that the grains nearly covered the entire surface of the image for the measurement script to work. This was not a problem in the samples at high temperatures and low strain rates, as the grains had enough time and temperature to grow at these parameters. The new strain free grains due to recrystallization during hot plastic deformation are clearly visible in Figure 20.

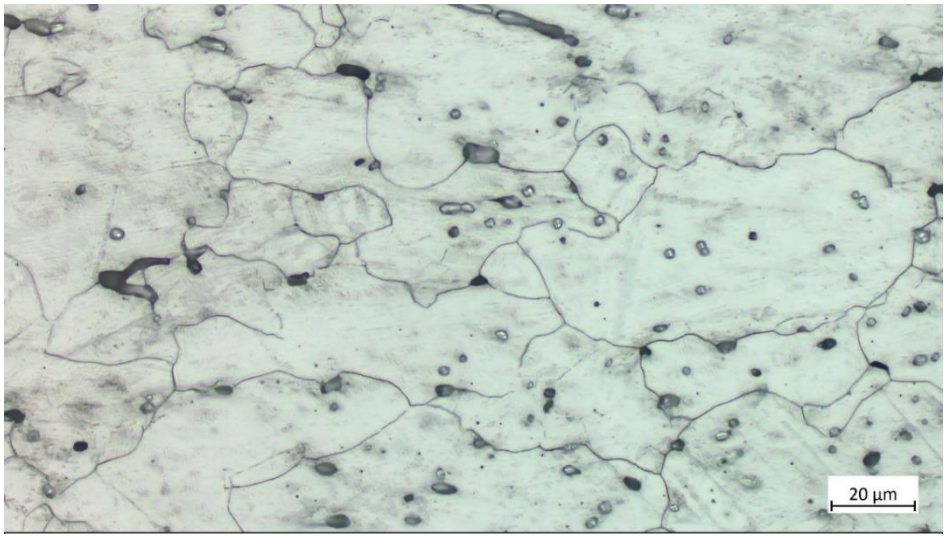

Figure 20: Microstructure of EBW melted AISI 304L austenitic stainless steel: Grains at a temperature of 1100°C and a strain rate of 0.001 s^{-1}, electrolytic etched with 60%HNO_3 and 40%H_2O

The images were then processed using Photoshop. The individual grains were traced, and the image was brought into the correct format for the next step.

With the help of a Matlab model [33] it was now possible to calculate the average grain size [µm], the number of grains and their distribution on the previously processed image which is visible in Figure 21.

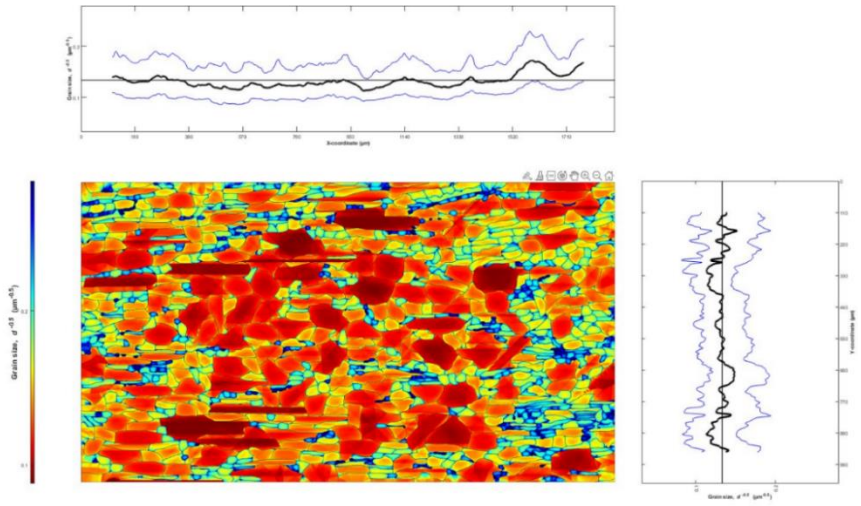

Figure 21: Microstructure of EBW melted AISI 304L austenitic stainless steel: Visualization of the grains

However, this script only works correctly if nearly the entire image is covered by grains. Since this was only the case for samples which were hot compressed at lower temperatures (≤ 850°C) with low strain rates (0.001 s^{-1}) and high temperatures (≥ 1000°C), it was not possible to measure the entire matrix with this method. Figure 22 shows a sample, where it was not possible to use the MATLAB script due to the small grain size visible on the surface. This is the case, because the grains are too small to draw during image preparation. Also, the script couldn't recognize the grains when they were very small.

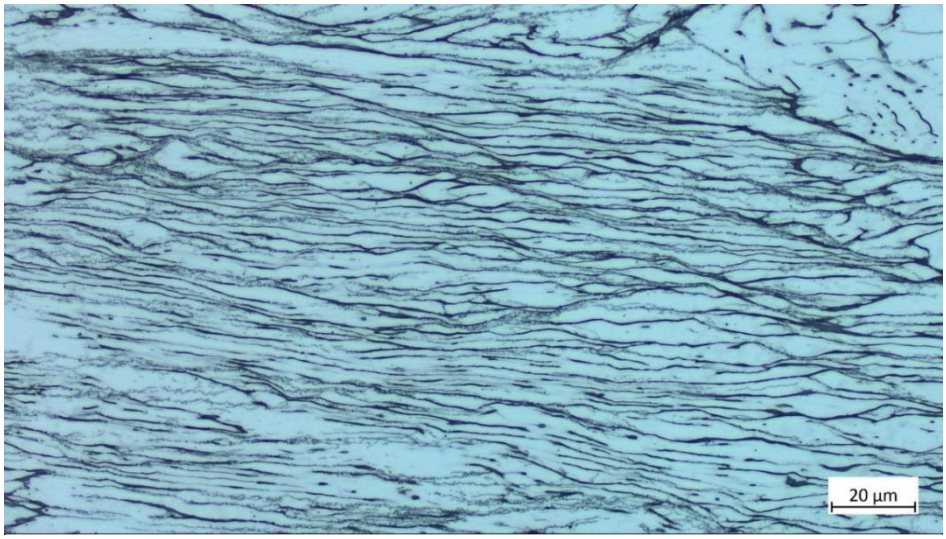

Figure 22: Microstructure of EBW melted AISI 304L austenitic stainless steel hot compressed at 800°C and a strain rate of 0.1 s^{-1}, electrolytic etched with 60%HNO_3 and 40%H_2O

The samples should be analyzed and eventually a trend can be found. Even among the evaluable samples, it is not possible to say whether all grains at temperatures below 1000°C during hot compression are new recrystallized grains or the not yet recrystallized microstructure with a higher dislocation density. Furthermore, the δ-ferrite phase was like a layer on top of the grains. In some cases it was difficult to recognize the grain boundary at all points, especially at lower temperatures (≤ 950°C) or higher strain rates (≥ 0.1 s^{-1}).

4.3.4. δ-Ferrite measurements

After all samples of the matrix were etched with the Beraha II etchant, images were taken using the camera attached to the light optical microscope (LOM). These images were used to evaluate the δ-ferrite evolution and the δ-ferrite aspect ratio of the samples at different temperatures and strain rates. For the image analysis ImageJ software was used. The Labkit plugin has been used for the analyzation. With this plugin it is possible to mark different areas in an image as foreground or background to train a model. The δ-ferrite phase was selected as the foreground. The austenitic phase was the background. The classifier was trained, and the different areas were displayed in different colors. The δ-ferrite was displayed in red and the γ-austenite in blue.

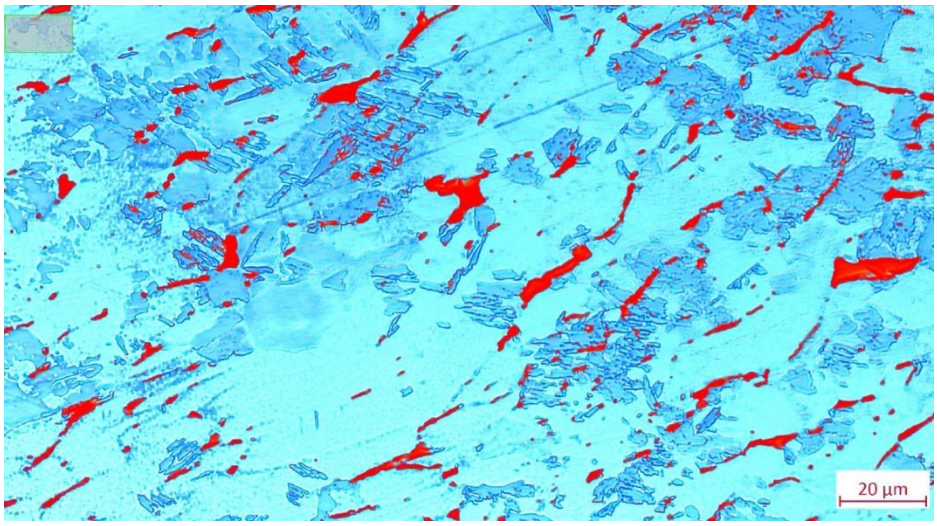

Figure 23: Microstructure of EBW melted AISI 304L austenitic stainless steel during training the ImageJ labkit model

It was then possible to further train the classifier in order to obtain an optimal output. The training file could then be saved. The classifier could now be applied to an entire folder using a macro available within the labkit plugin. The result was a seemingly black 8-bit image.
This image was then opened in ImageJ.

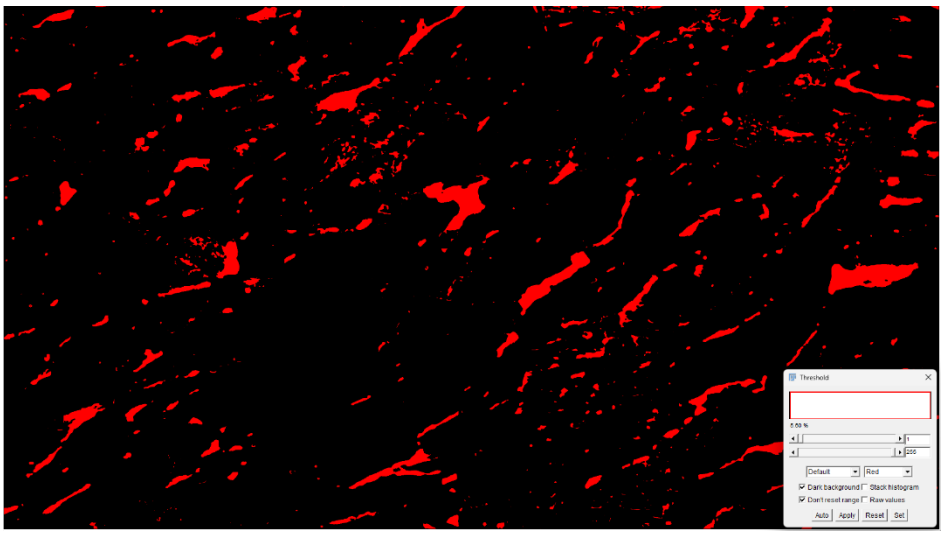

Figure 24: Microstructure of EBW melted AISI 304L austenitic stainless steel: ImageJ threshold

The fraction of the δ-ferrite phase, which is is the red colored phase in Figure 24 was obtained by setting the threshold of the phases of the image. Depending on the magnification, 5-20 images were analyzed per sample. The δ-ferrite fraction was determined for each image. The mean value of the δ-ferrite fractions with its standard deviation was calculated for each sample. Unfortunately, the image quality of the samples was often poor, which is due to the difficult etching method. As a result, the individual 8-bit images had to be compared with the actual images taken with the LOM. Even if each image was checked for correctness and was reworked manually, if necessary, errors cannot be ruled out with such a fine granular distribution of the δ-ferrite on each picture. However, it was recognized that the image quality

improved at high temperatures and low strain rates. Good images were also found at high temperatures with higher strain rates, as can be seen in Figure 25.

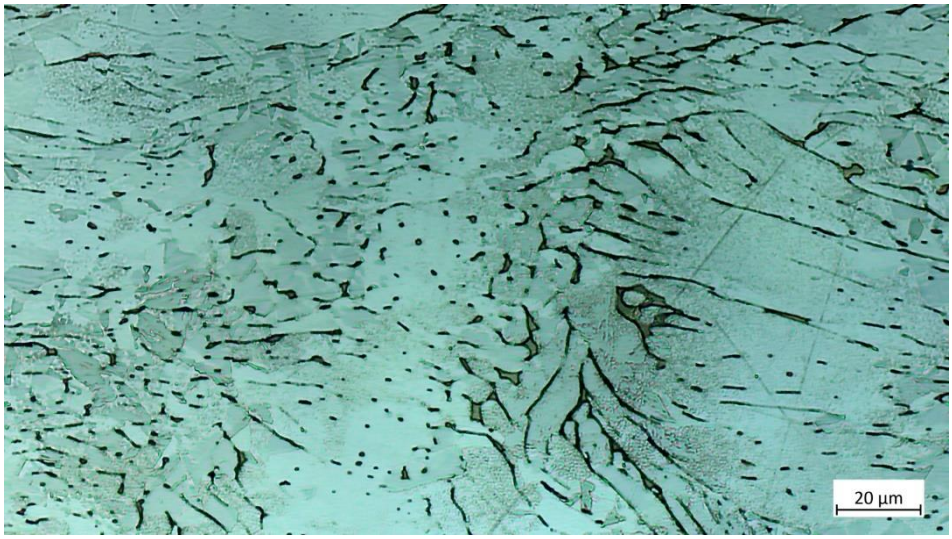

Figure 25: Microstructure of EBW melted AISI 304L austenitic stainless steel after hot compression at 1100°C and a strain rate of 10 s^{-1} and wet etching with Beraha 2

Good image quality at high strain rates above 0.1 s^{-1} could only be achieved at hot compression temperatures of 1100°C. At lower temperatures and higher strain rates the δ-ferrite was partly less visible. There was always a chance that not all of the δ-ferrite would be etched out as visible in Figure 26. On the other hand, it was possible, that the etching was too strong. Then, a black, not removable layer was formed on the surface of the microstructure. Also, here the classifier couldn't always distinguish between the δ-ferrite phase and the layer. In this case, manual reworking of the image with drawing tools was carried out as good as possible.

Figure 26: Microstructure of EBW melted AISI 304L austenitic stainless steel after hot compression at 800°C and a strain rate of 0.1 s^{-1} and wet etching with Beraha 2

4.3.4.1. Aspect ratio

In order to obtain the aspect ratio of the δ-ferrite, the previously prepared 8-bit images were used. For this the particle analyze function was used which is included in ImageJ. The model used for this draws best fitting ellipses around the δ-ferrite phases. The 8-bit output image is displayed in Figure 27.

Figure 27: Microstructure of EBW melted AISI 304L austenitic stainless steel: 8-bit picture for aspect ratio calculation

Figure 28 shows the best fitting ellipses, which are inserted and used for particle measurement.

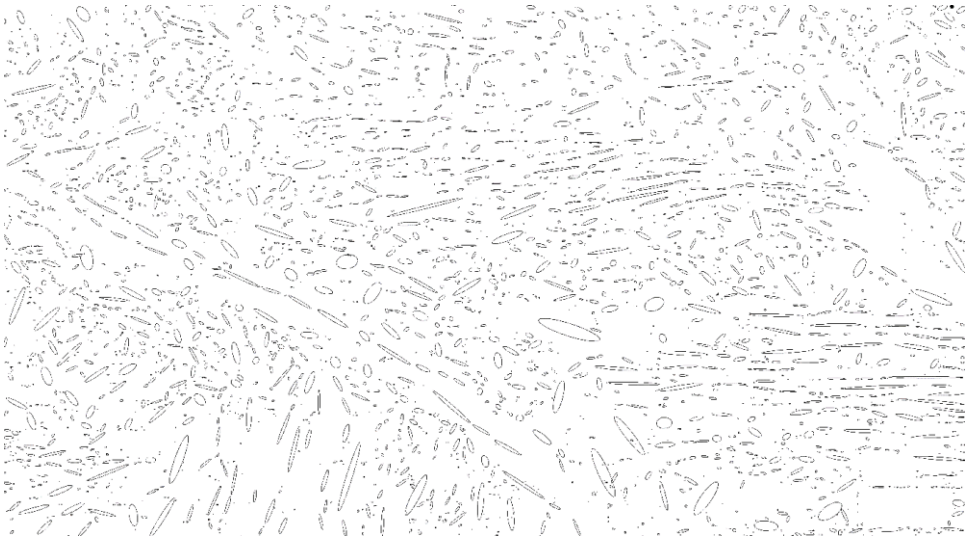

Figure 28: Microstructure of EBW melted AISI 304L austenitic stainless steel: Ellipses for aspect ratio measurement

A CSV file was generated as a result of the measurement. This contained the values required to calculate the aspect ratio of the individual ellipses. The "Major" and "Minor" values of the were necessary for this purpose. These are the primary and secondary axes of the best fitting ellipse.

$$Aspect\ ratio = \frac{Major}{Minor} \quad (6)$$

This is done for the same images, used to determine the δ-ferrite fraction. The results of the individual output-csv-files of a sample were combined and the mean value was calculated.

4.3.3. Feritoscope

Using a feritoscope, it is possible to measure the δ-ferrite fraction in austenitic or duplex steels. It is a non-destructive measurement method [34].
A "Fischer" feritoscope was used for this purpose.
In the first step, the measuring device was calibrating the feritoscope by measuring reference samples that have a certain δ-ferrite content. To do this, the measuring needle was pressed onto different surfaces with a defined δ-ferrite content. If the values were displayed correctly with a minimal deviation, the measurement of the matrix samples could begin. For this purpose, the measuring needle was pressed onto the center of the samples, as the highest deformation was to be expected here.

Figure 29: Feritoscope measurement

Ten measurements were carried out per sample. The results could be read directly from the measuring device. The measurements for the δ-ferrite fractions were noted and the standard deviation was calculated.

4.3.4. Light Optical Microscopy (LOM)

With the light optical microscope, it was possible to check the quality during the entire experimental process. It was used during grinding and polishing to check the surface quality. During etching, it was used to find the correct parameters for the experiments. A camera in the microscope was used to evaluate the results. Pre-programmed models in the microscope allowed templates to be used. The images contained a description of the sample and how they were processed as well as their magnification.
These images were then analyzed using Photoshop and ImageJ and the δ-ferrite fraction and average grainsize could be found.

4.4. Hardeness test

Finally, a hardness test was also carried out. The "EMCO_TEST Durascan" measuring device from Zwick Roell was used for this. The samples were clamped in a holder. The measurement mapping and the parameters were entered in the corresponding "ecos software". The Vickers hardness was measured.

The parameters 0.5 HV and the measuring point distance of 3 µm were set. Whereby 0.5 gives the weight which is applied during the test. 65 measuring points were made in the middle of one sample, where the region of interest was (see Figure 11). The distance indicated the distance between the measuring points.

Now the machine automatically carried out the measurement of six samples in one measurement cycle. The load was applied for 10-15 seconds. After that, the diagonal of the square which is visible in Figure 30 was measured by the machine.

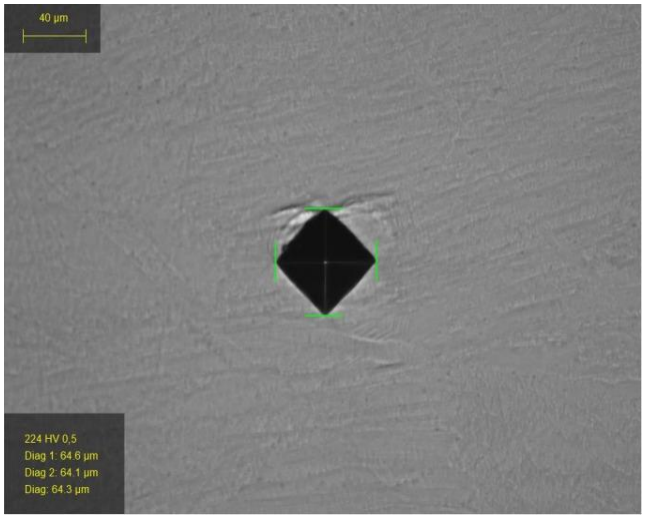

Figure 30: Hardness measurement

An excel file was automatically generated as an output from the measurements. The average hardness of the samples as well as the standard deviation was calculated.

5. Results and discussion

This chapter of the thesis deals with the results that emerged from the experiments and investigations carried out. In the first step, the adiabatically corrected flow stress curves at different temperatures and strain rates are discussed. The adiabatic temperature correction at different strain rates is also reviewed. In the next step, the evolution of the δ-ferrite in the microstructure is investigated. This includes the δ-ferrite fraction and the aspect ratio of the δ-ferrite in the microstructure. The results from the grain size measurement and the hardness test are also discussed.

5.1. Flow stress curves

Flow stress curves are generated by data, measured by the Gleeble-3800 simulator. To get isothermal flow curves adiabatical heating correction was necessary.

5.1.1. Flow stress curves at different strain rates

As a result from the hot compression test, flow stress curves at different strain rates and temperatures were generated. Figure 31 shows the measured and adiabatically corrected flow stress curves at different temperatures and at different strain rates.

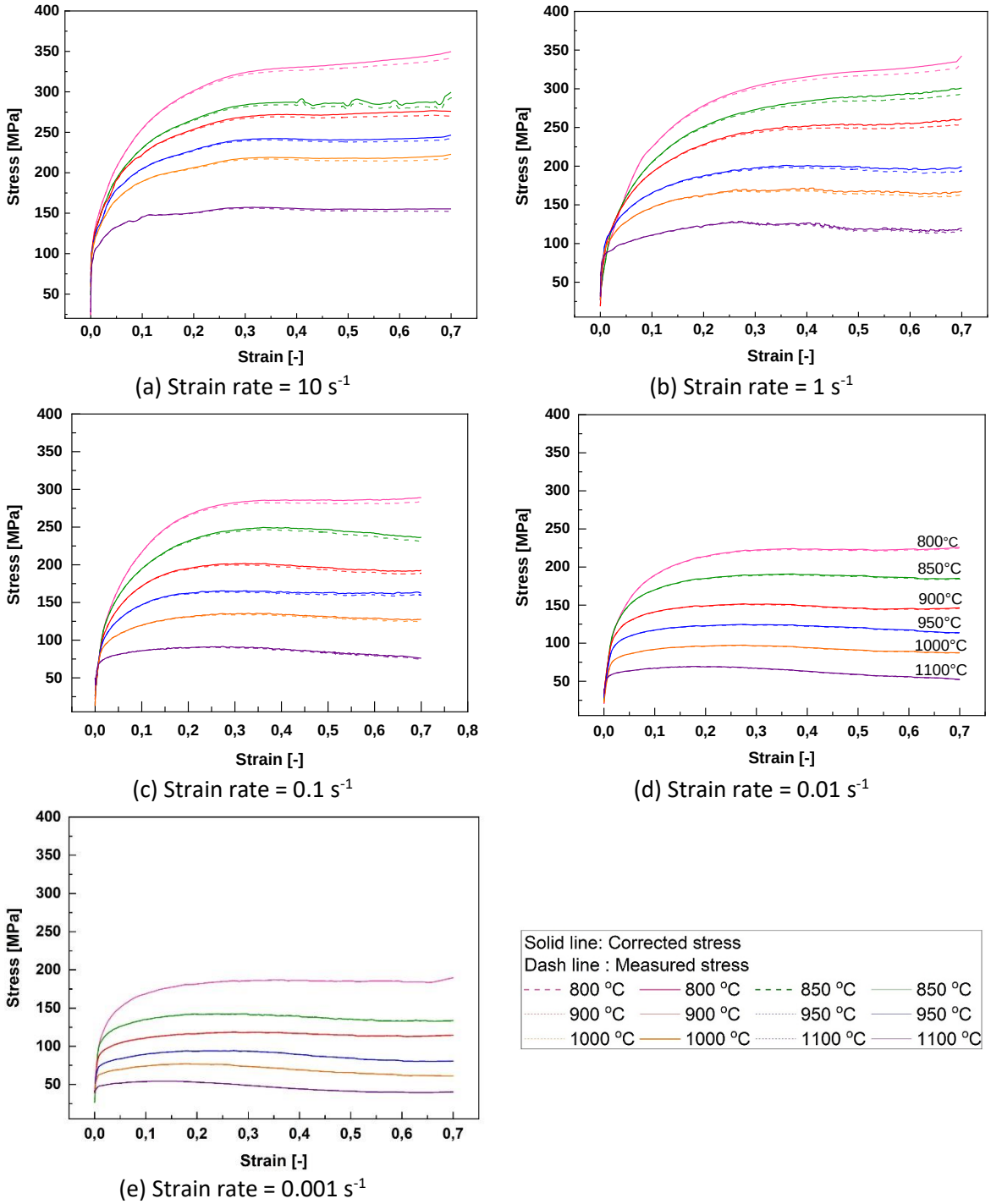

Figure 31: Measured and adiabatically corrected flow stress curves at different strain rates

The initial flow curves which are shown as dashed lines in the diagrams increased as a result of the adiabatic heating correction. The corrected curves are shown as full lines. The flow curves increase with increasing strain rate due to the dislocation accumulation during the hot compression test. Decreasing temperatures leads to a reduced dynamic recrystallization and

recovery, which means vice versa that a more pronounced work hardening occurs. Therefore, flow stress increases with decreasing temperature as visible in Figure 31 (a-e).

Figure 31 (e) shows the flow stress curves at a strain rate of 0.001 s^{-1} and at different temperatures. Here a maximum stress of about 200 MPa is reached at a temperature of 800°C during hot compression. The lowest flow stress with a value of about 50 MPa was measured at a hot compression temperature of 1100°C and a strain rate of 0.001 s^{-1}. In the diagram with a constant strain rate of 10 s^{-1} which is shown in Figure 31 (a) at a temperature of 800°C, a maximum value of roughly 350 MPa was measured.

5.1.2. ΔT of the adiabatic heating correction

Figure 31 shows, that at lower temperatures higher adiabatic heating is caused by the hot compression test, visible through the distance between the dashed line and full line of a flow curve. Therefore, also the correction of these values is higher at lower temperatures. The temperature variation (ΔT) due to adiabatic heating with the strain rate is visible in Figure 32.

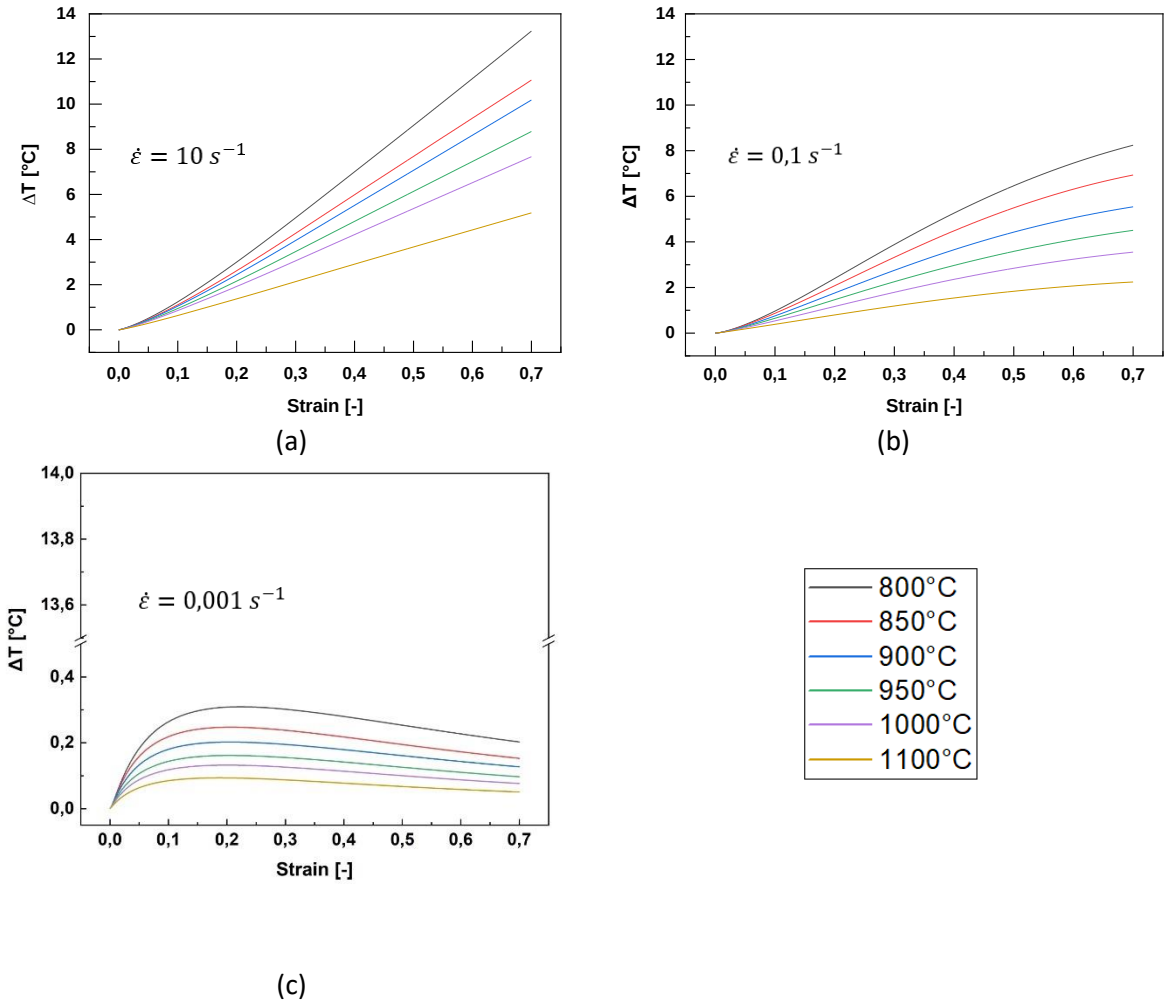

Figure 32: (a) shows the ΔT between the corrected- and the measured flow stress curve at a strain rate of 10 s^{-1} (b) shows the ΔT at a strainrate of 0.1 s^{-1} (c) shows the ΔT at a strainrate of 0.001 s^{-1}

Figure 32 (a-b) show an increasing temperature difference ΔT between the measured flow stress curves and the adiabatically corrected flow stress curve is present at increasing strain

rates. At a strain rate of 0.001 s^{-1} which is visible in (c), the temperature difference ΔT between the initial and the corrected flow curves is hardly present for all temperatures. These values show that nearly isothermal conditions occur at low strain rates. As the strain rate increases and the temperature decreases, more adiabatical heat is generated during the hot compression test. This leads to higher temperature difference.

5.1.3. Work hardening vs. recrystallization

The work hardening rate was calculated and plotted in Figure 33 (a-c). On the right side the flow stress curve is shown for the according strain hardening rate visualization which is present on the left side.

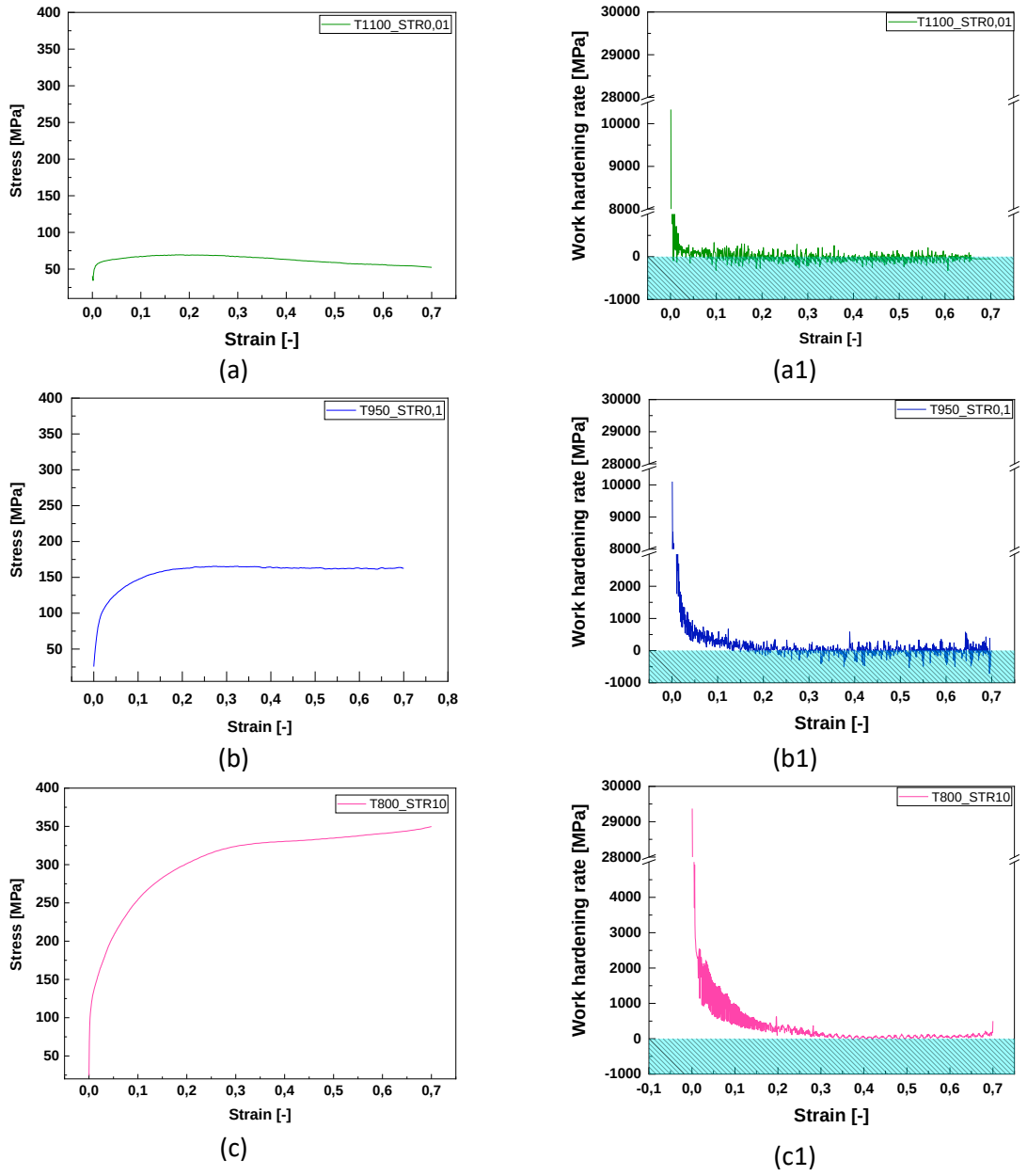

Figure 33: Work hardening rate at different temperatures and strain rates.

Figure 39 (a1) shows the strain hardening rate at a temperature of 1100°C and a strain rate of 0.01 s^{-1}. The dashed cyan area below the zero line indicates the negative range. A positive work hardening rate can be determined at the beginning at all hot compression parameters. In the flow stress diagram, this reflects the elastic deformation range at the beginning. In this area, the dislocation density is increased by work hardening until dynamic recrystallization takes place. Then work hardening and dynamic recrystallization compete as the compression continues. If the calculated work hardening rate is negative and therefore in the cyan colored area, dynamic recrystallisation is predominant.

Figure 33 (a1) and Figure 33 (b1) show similar work hardening rates of about 10000 MPa at the beginning of the hot compression, whereby it decreases faster at Figure 33 (a) where a higher temperature and lower strain rate was present. After the rapid decrease work hardening and flow softening compete. Figure 33 (c1), on the other hand, shows a significantly higher work hardening rate of about 29000 MPa at the beginning, which is due to the low temperature and the high strain rate during hot compression, which favors the formation of dislocations. As the flow curve at Figure 33 (c) rises, the work hardening rate exceeds the flow softening rate almost over the whole hot compression test. Therefore, most values in Figure 33 (c1) are positive.

5.2. Overall microstructure of deformed sample

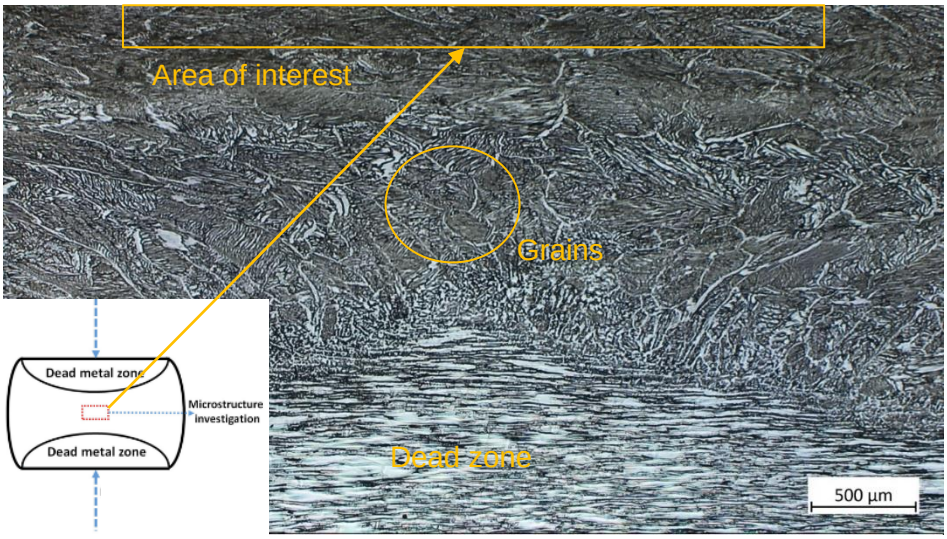

Figure 34: Microstructure of EBW melted AISI 304L austenitic stainless steel: Zones of hot compressed AISI 304L at 850°C with a strain rate of 0.001 s^{-1}

Figure 34 shows the microstructure of a sample that has been hot compressed. The dead zone is clearly visible on the bottom of the image. The sample was hot compressed at 850°C and a strain rate of 0.001 s^{-1}. Large grains are visible in the middle of the figure. Inside these yellow marked grains new strain free grains were formed due to dynamic recrystallization. On top of

the image, the area of interest is shown. There the maximum deformation occurred during the hot compression test. This led to a higher temperature as well as a higher real strain in this area.

5.3. δ-Ferrite

In this chapter the results of the δ-ferrite measurements are discussed. This includes the δ-ferrite fraction measured with image analysis and with feritoscope as well as the aspect ratio measurement.

5.3.1. δ- ferrite fraction by image analysis

Table 2 shows the results of the image analysis method. Depending on the magnification at which the image was taken, between 6 and 23 images were processed. The standard deviation was calculated from the results obtained. Due to the difficult etching method, not all images could be reliably analyzed. For samples that were deformed at high temperatures (1100°C) and at low strain rates (0.001 s^{-1}), the results correlate with each other. A trend can be identified. These results are marked in green in Table 2.

Table 2: δ-ferrite fraction by image analysis

δ-Ferrite fraction from image analysis [%]						
STR [s^{-1}]	**800°C**	**850°C**	**900°C**	**950°C**	**1000°C**	**1100°C**
0.001	9.5±1.4	7±2.3	4.7±1.1	3.9±1.1	3.3±1.9	1.6±0.8
0.01	6.2±1.5	10.2±1.3	12.4±1	7.4±1	9.9±1.6	3.9±1.5
0.1	5.4±1.4	8.1±2.9	11.9±1.6	8.9±1.5	5.4±1	6.4±1.3
1	9.8±1.4	10.3±1.5	11.2±1	6.4±1.4	9.2±1	6.8±2.3
10	12.9±2.4	5.5±1.5	5.4±1.3	9.3±2.1	11.3±2	9.2±1.2

The weld zone of the reference sample was further investigated. The results show a δ-ferrite fraction of 10.3%±1.2%. In Figure 35 the δ-ferrite content at different temperatures and strain rates is shown.

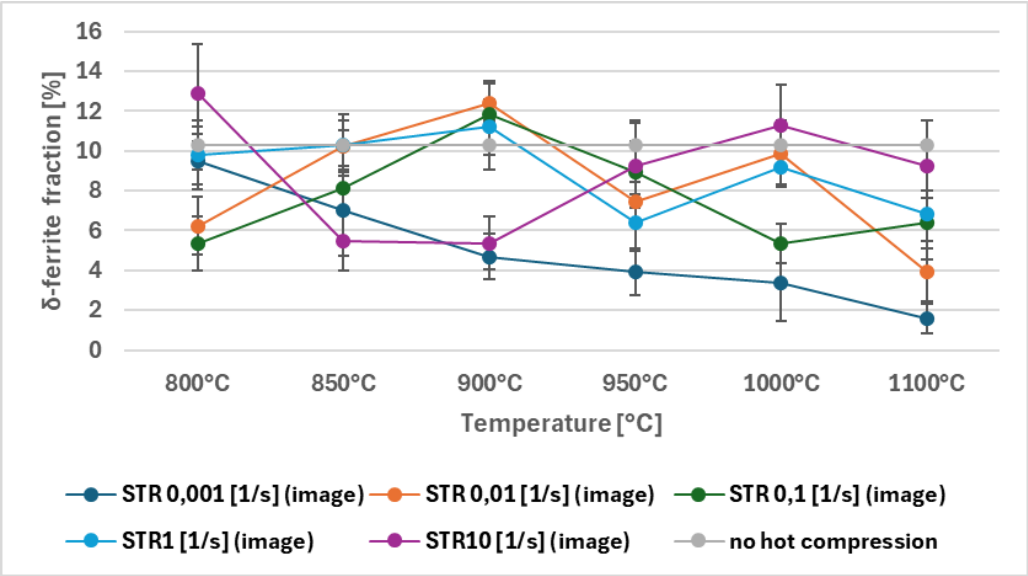

Figure 35: Distribution of δ-ferrite in the hot compressed AISI 304L austenitic stainless steel at different parameters determined by image analysis methode

Based on the measured values, the δ-ferrite content increases with decreasing temperature at a strain rate of 0.001 s^{-1}. The highest δ-ferrite fraction was measured at a temperature of 800°C and a strain rate of 10 s^{-1}, whereas the lowest fraction was found at hot compression parameters of 1100°C and a strain rate of 0.001 s^{-1}. The standard deviation of the measurements was between 1% and 3%. The δ-ferrite value of the not hot compressed sample is not related to the values of the hot compressed samples. It can be seen that the values do not follow a trend at higher strain rates (≥ 0.001 s^{-1}) and at lower temperatures (≤ 1100°C) at strain rates above 0.001 s^{-1} during hot compression. The values are chaotic, which means that no statement can be made from the available data which can be attributed to the partly bad image quality due to the difficult etching conditions.

Figure 36 shows the microstructure of the sample, which was hot compressed at 1100°C and a strain rate of 10 s^{-1}.

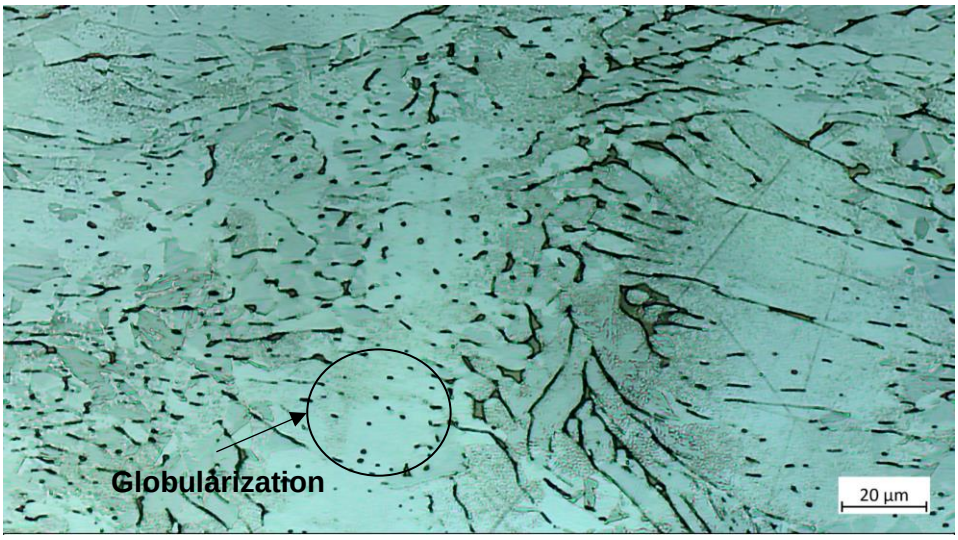

Figure 36: Microstructure of EBW melted AISI 304L, hot compressed at a temperature of 1100°C and a strain rate of 10 s^{-1}, wet etched with Beraha 2 showing globularization

The black and brown δ-ferrite phase in Figure 36 is clearly distinguishable from the brighter γ-austenite phase which is in the background. In the center of the image, globularization of the δ-ferrite phase due to the dissolution of the phase at high temperatures (≥1000°C) can be seen. Unfortunately, not all microstructures showed such a behavior. Figure 37, Figure 38 and Figure 39 show, that the image quality decreases rapidly with decreasing temperatures and increasing strain rates.

Figure 37: Microstructure of EBW melted AISI 304L, hot compressed at temperatures of 800°C and a strain rate of 0.01 s^{-1}, wet etched with Beraha 2 showing poor visibility of the δ-ferrite phase

In Figure 37 the tested sample was hot compressed at a temperature of 800°C and a strain rate of 0.01 s^{-1}. At several areas it is easy to distinguish between the δ-ferrite and the γ-austenite phase. In darker areas it is difficult to clearly differentiate between them.

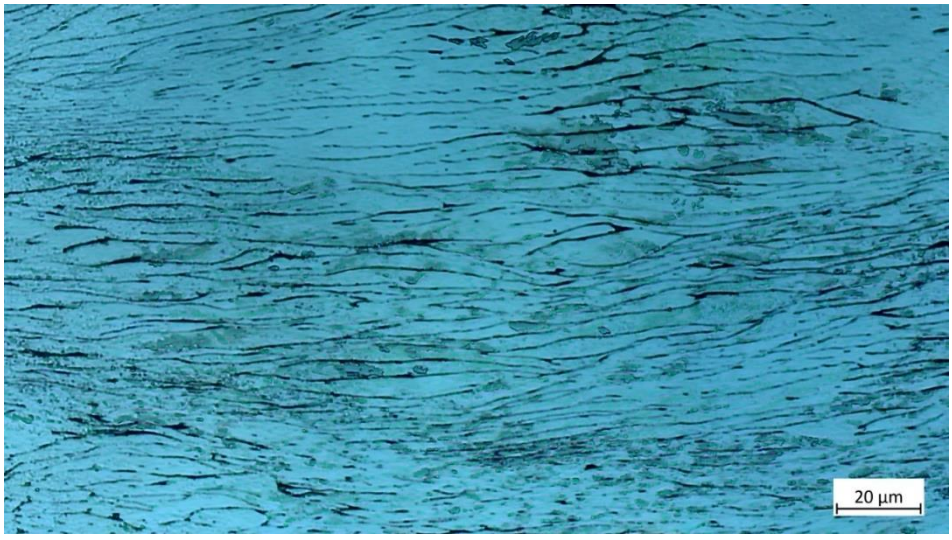

Figure 38: Microstructure of EBW melted AISI 304L, hot compressed at temperatures of 800°C and a strain rate of 10 s^{-1}, wet etched with Beraha 2

In Figure 38 the sample was exposed to a temperature of 800°C and a strain rate of 10 s^{-1} during the hot compression test. In the picture, the δ-ferrite can generally be easily differentiated from the δ-austenitic phase. However, the δ-ferrite needles are very thin, which means that they may not be completely etched during the etching-process. If the etching

process was extended, however, a black layer formed over the surface, which meant that no result was possible at all. Such a layer can be observed in Figure 39. This workpiece was compressed at a temperature of 950°C and a strain rate of 1 s^{-1}.

Figure 39: Microstructure of EBW melted AISI 304L, hot compressed at temperatures of 950°C and a strain rate of 1 s^{-1}, wet etched with Beraha 2

In Figure 39 the effect of compression on the δ-ferrite phase is visible. The δ-ferrite needles are reshaped like an accordion by the deformation.

5.3.2. δ- ferrite fraction measurement by feritoscope

A feritoscope was used as a second method to determine the δ-ferrite fraction. For each sample, 10 measurements were taken at the surface Previous etching made it possible to identify the area of interest. The measurements were carried out in this area. The standard deviation was also calculated from these measurement points.

Table 3: δ-ferrite fraction by feritoscope

δ-Ferrite fraction from feritoscope [%]						
STR [s^{-1}]	**800°C**	**850°C**	**900°C**	**950°C**	**1000°C**	**1100°C**
0.001	6.2±0.1	5±0.2	4.7±0.3	3.9±0.1	2.5±0.2	1.3±0.1
0.01	6.1±0.2	5.9±0.4	6.1±0.2	5.6±0.2	4.8±0.3	4.1±0.4
0.1	6±0.2	7.1±0.3	6.9±0.5	6.5±0.4	6.5±0.3	5.9±0.6
1	6.3±0.3	6.8±0.1	6.9±0.2	7.4±0.5	8±0.3	7±0.1
10	6.1±0.3	6.8±0.2	6.3±0.3	7.2±0.2	7.3±0.3	8±0.2

The measured fraction of the reference sample in the welded area was 9.6% ±1.6%. Compared with the matrix, it shows that the δ-ferrite fraction is highest, when no hot compression is carried out.

The standard deviation of the measured values for the samples in the tested matrix was between 0.1% and 0.6%.

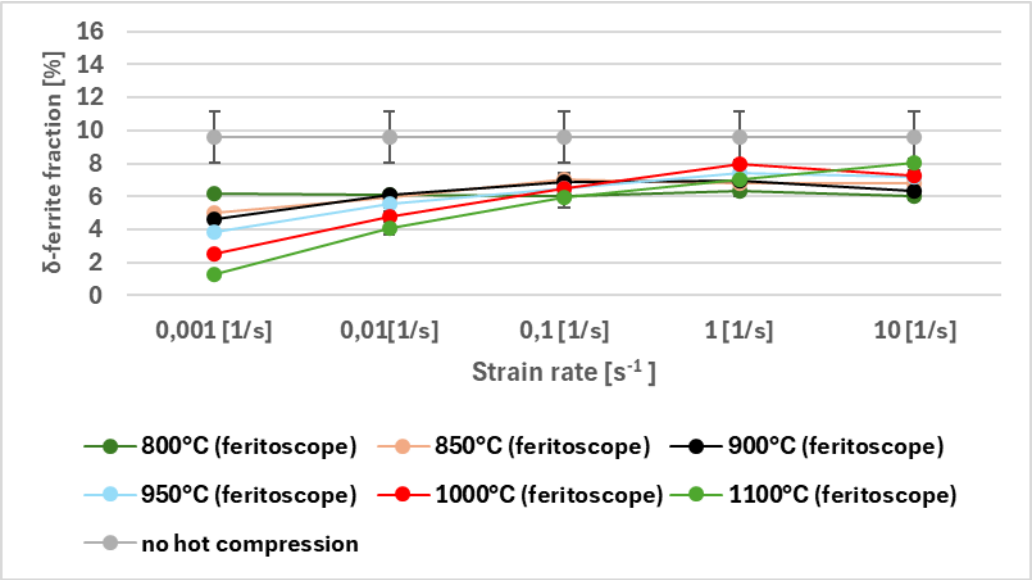

Figure 40: Distribution of δ-ferrite in the hot compressed AISI 304L austenitic stainless steel at different parameters determined by feritoscope at different strain rates

In Figure 40 it can be seen that the values correlate with each other, and trends can be identified. The δ-ferrite fraction at 1100°C and a strain rate of 0.001 s^{-1} is the lowest with a value of 1.3%±0.1%. The highest δ-ferrite fraction of the measured values was measured at 1100°C and a strain rate of 10 s^{-1} with a value of 8%±0.2%. Only the EBW welded, not hot compressed sample shows a higher value with 9.6% ±1.6%. It can be observed that with increasing temperatures the δ-ferrite fraction decreases more as the strain rate decreases. Further it is visible in Figure 41 that the δ-ferrite fraction is more constant as the temperature during hot compression decreases. At a temperature of 800°C nearly no change is visible at the measured data points.

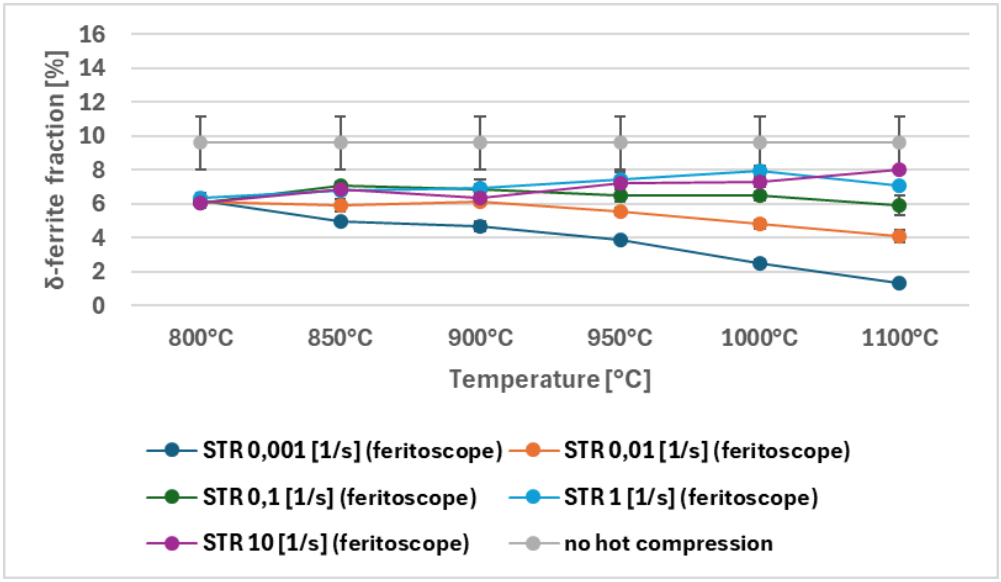

Figure 41: Distribution of δ-ferrite in the hot compressed AISI 304L austenitic stainless steel at different parameters determined by feritoscope at different temperatures

Table 4 and Table 5 show the measured values for the δ-ferrite fraction measured using the feritoscope and the image analysis method. Table 6 visualizes the percentage difference between the measured values.

Table 4: Comparison fraction from image analysis

δ-Ferrite fraction from feritoscope [%]						
STR [s^{-1}]	800°C	850°C	900°C	950°C	1000°C	1100°C
0.001	6.2±0.1	5±0.2	4.7±0.3	3.9±0.1	2.5±0.2	1.3±0.1
0.01	6.1±0.2	5.9±0.4	6.1±0.2	5.6±0.2	4.8±0.3	4.1±0.4
0.1	6±0.2	7.1±0.3	6.9±0.5	6.5±0.4	6.5±0.3	5.9±0.6
1	6.3±0.3	6.8±0.1	6.9±0.2	7.4±0.5	8±0.3	7±0.1
10	6.1±0.3	6.8±0.2	6.3±0.3	7.2±0.2	7.3±0.3	8±0.2

Table 5: Comparison fraction from feritoscope

δ-Ferrite fraction from image analysis [%]						
STR [s^{-1}]	800°C	850°C	900°C	950°C	1000°C	1100°C
0.001	9.5±1.4	7±2.3	4.7±1.1	3.9±1.1	3.3±1.9	1.6±0.8
0.01	6.2±1.5	10.2±1.3	12.4±1	7.4±1	9.9±1.6	3.9±1.5
0.1	5.4±1.4	8.1±2.9	11.9±1.6	8.9±1.5	5.4±1	6.4±1.3
1	9.8±1.4	10.3±1.5	11.2±1	6.4±1.4	9.2±1	6.8±2.3
10	12.9±2.4	5.5±1.5	5.4±1.3	9.3±2.1	11.3±2	9.2±1.2

Table 6: Percentage difference between the δ-ferrite fraction measured with feritoscope and image analysis method with the feritoscope measured values as initial values

Percentage difference [%]						
STR [s^{-1}]	800°C	850°C	900°C	950°C	1000°C	1100°C
0.001	42%	33%	<1%	2%	28%	19%
0.01	1%	53%	67%	29%	69%	4%
0.1	11%	14%	52%	31%	18%	7%
1	43%	41%	46%	15%	14%	3%
10	72%	14%	16%	24%	42%	13%

The green marked values show a percentage difference between 0% and 20%, the orange marked values a difference between 20% and 40% and the red marked values a percentage difference above 40%. For the not hot compressed reference sample, a δ-ferrite value of 9.6%±1.5% was measured with the feritoscope. Using the image analysis method, a value of 10.3%±1.2% was found for the δ-ferrite fraction. From this, a percentage difference of 7% between the methods could be determined.

It is visible that samples which were compressed at a low strain rate (0.001 s^{-1}) and also samples which were compressed at high temperatures (1100°C) have a good comparability and show a similar trend. Unfortunately, as visible in Table 6 especially at lower hot compression temperatures and high strain rates the values have a high percentage difference. However, because of the large fluctuation of the measurements done with image analysis as visible in Figure 35 it cannot be assumed that the values for these parameters are reliable. Compared to this the values for the δ-ferrite fraction seems stable and comprehensible as visible in Figure 40 and Figure 41.

5.3.3. Aspect ratio of δ-ferrite

The aspect ratio of δ-ferrite and the related deviation was measured from the images which were used for the determination of the δ-ferrite fraction.

Table 7: Aspect ratio of δ-ferrite

Aspect ratio						
STR [s^{-1}]	800°C	850°C	900°C	950°C	1000°C	1100°C
0.001	2.7±0.2	2.8±0.2	2.1±0.1	2.5±0.3	2.4±0.3	1.8±0.2
0.01	2.5±0.2	2.6±0.1	2.4±0.3	2.6±0.3	2.7±0.5	2.7±0.4
0.1	3.1±0.2	3.6±0.5	2.9±0.2	2.9±0.5	3.4±0.7	2.3±0.2
1	3.5±0.6	2.8±0.8	4±0.8	3±0.5	3.5±0.5	2.7±0.3
10	4.8±0.8	2.9±0.4	4.4±1.3	3±0.3	3.7±0.5	3.5±0.7

Table 7 shows the results from the aspect ratio calculations. The aspect ratio of the EBW-welded, not hot compressed part of the reference sample was 2.9±0.4.

As the results of the Table 7 are based on the results of the δ-ferrite fraction also only the blueish marked values were used for the analysis. This was done to ensure that only correct and with the δ-ferrite fraction, measured by the feritoscope comparable values are used. Table 7 also shows, that the standard deviation is generally higher at high strain rates. At these parameters, the δ-ferrite phase was kinked in some areas. This might have affected the results from the ellipse model used to determine the aspect ratio.

Figure 42 visualizes the course of the aspect ratio at different temperatures and different strain rates.

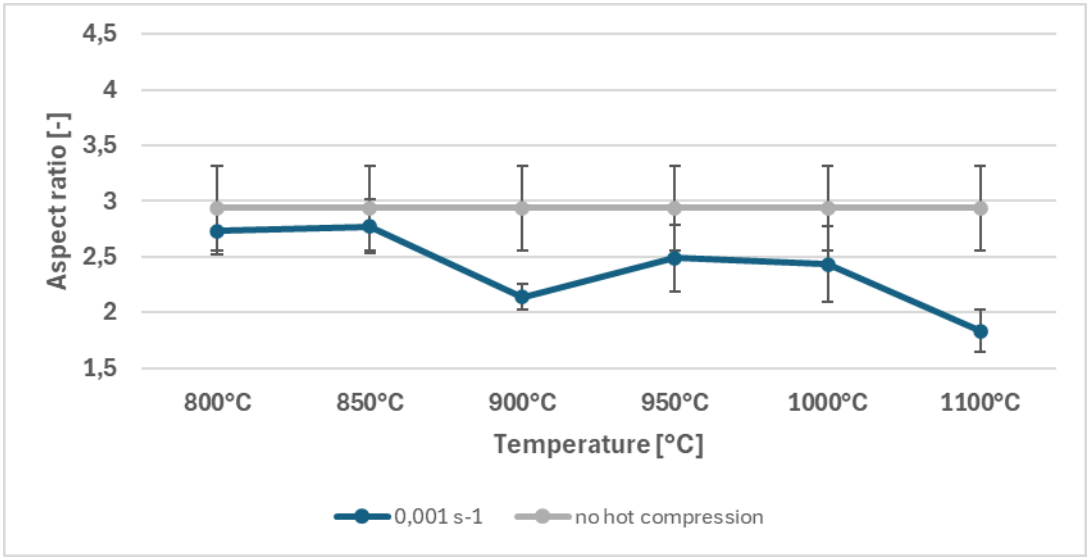

(a)

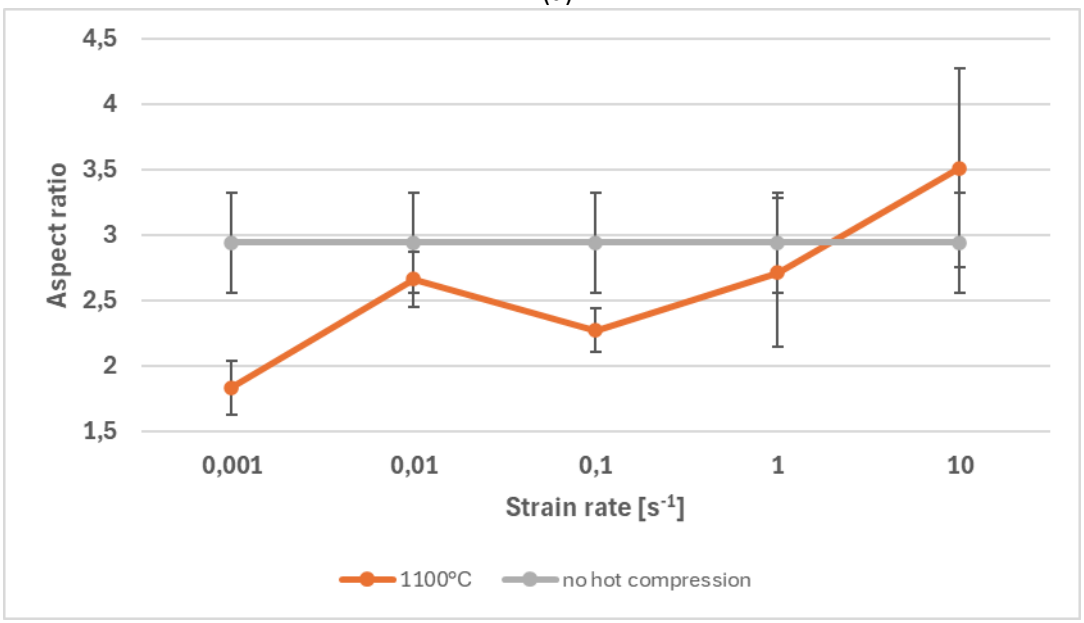

(b)

Figure 42: (a) Aspect ratio at a strain rate of 0.001 s^{-1} and different temperatures, (b) Aspect ratio at 1100°C and different strain rates

Figure 42 (a) shows the aspect ratio of the hot compressed samples at a strain rate of 0.001 s^{-1} and at different temperatures as well as the reference sample. At a temperature of 850°C the aspect ratio is highest with a measured value of 2.8±0.2 which shows, that the δ-ferrite dissolution and therefore globularization is weak at this compression parameters. On the other hand, the aspect ratio at high temperatures and low strain rate is low with a value of 1.8±0.2. This indicates that δ-ferrite dissolution is stronger at higher temperatures and longer deformation times. The morphology of δ-ferrite gets globular.

Figure 42 (b) shows the aspect ratio of samples which were compressed at a temperature of 1100°C and at different strain rates. The diagram indicates that the aspect ratio is higher at higher strain rates. When fast deformation due to high strain rates (≥ 1 s^{-1}) occurs, there is only a little time for the dissolution of the δ-ferrite phase. Even at high temperatures the

globularization is therefore weak. The standard deviation visualized in the diagram shows an increasing deviation with an increasing strain rate. It is low between 0.001 s^{-1} and 0.1 s^{-1} and increases strongly at 1 s^{-1} and 10 s^{-1}. This might be due to the more kinked δ-ferrite phases at higher strain rates. At a strain rate of 10 s^{-1}, the aspect ratio exceeds that of the not hot compressed, EBW-welded reference sample, which can also be attributed to the kinked δ-ferrite phase. To visualize the results, histograms were created with the data of the aspect ratio calculations at origin lab.

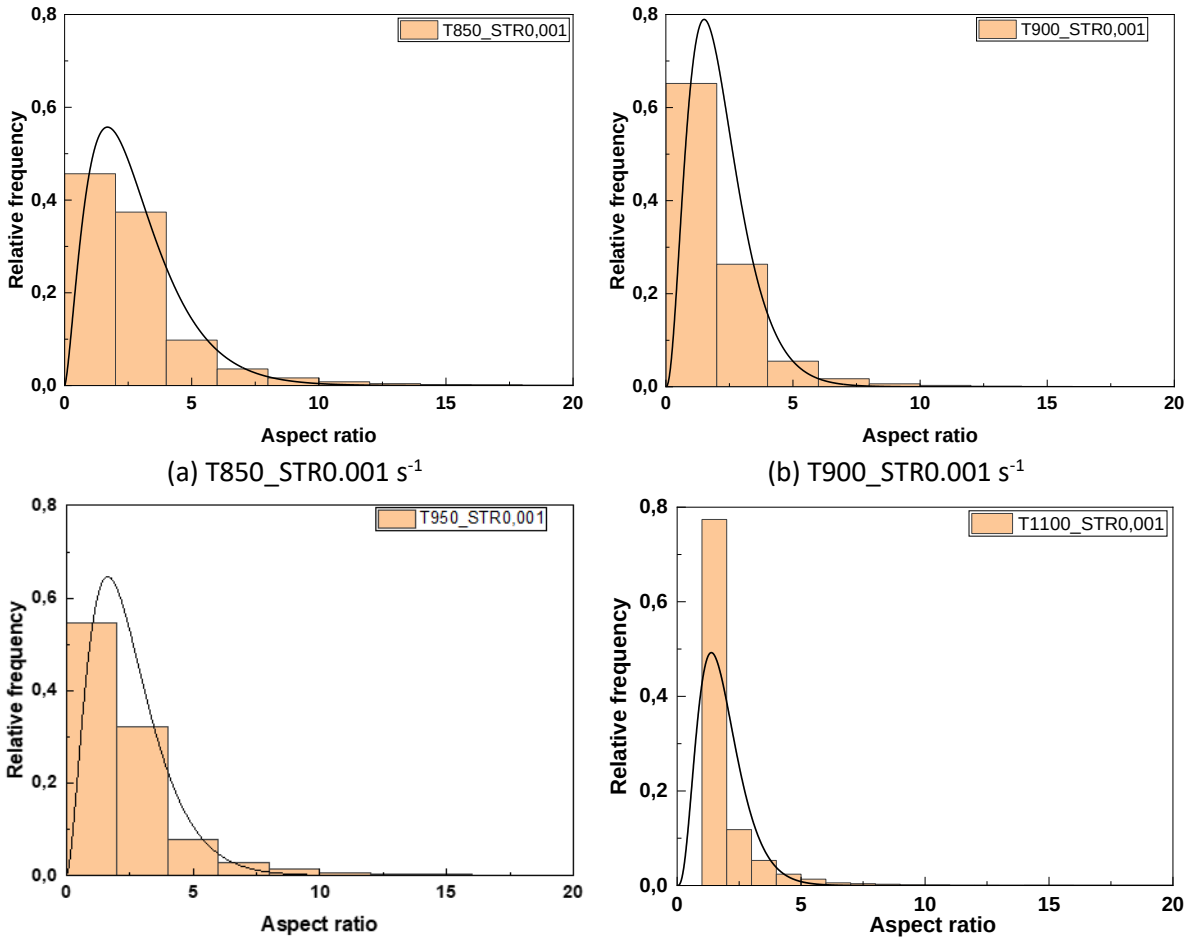

Figure 43: Aspect ratio of the δ-ferrite phase at different temperatures

The histograms in Figure 43 show the relative frequency of the δ-ferrite phases aspect ratios at varying temperatures and a constant strain rate of 0.001 s^{-1}. At low temperatures demonstrated in Figure 43 (a), the number of δ-ferrite phases with high aspect ratios is high. With increasing temperatures, the dissolution and the corresponding globularization becomes more pronounced, which leads to small round δ-ferrite phases. At 1100°C mostly globular phases are present in the microstructure as visible in Figure 43 (d).

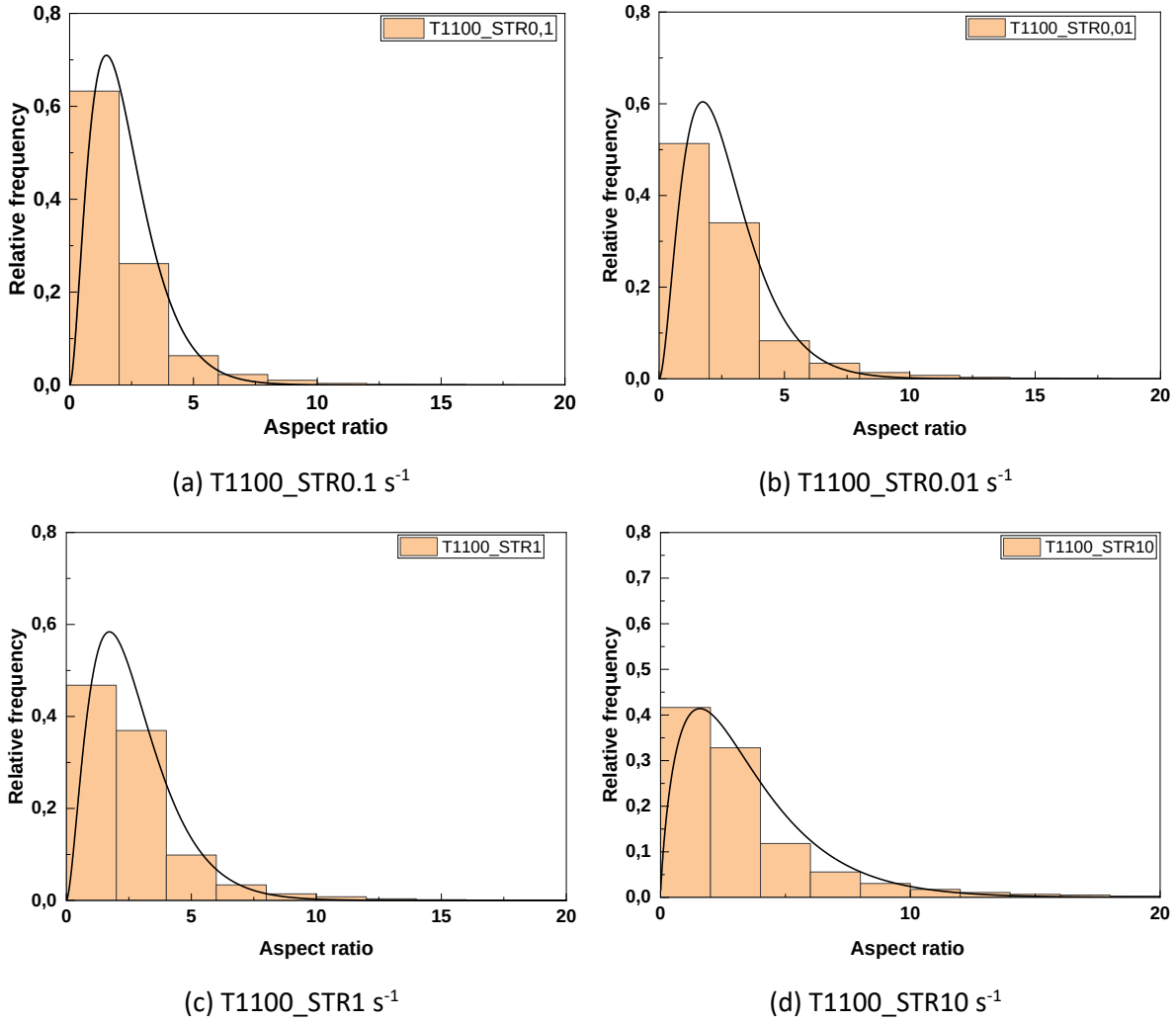

Figure 44: Histograms: Aspect ratio of the δ-ferrite phase at different strain rates

The histograms in Figure 44 show the relative frequency of the δ-ferrite phases aspect ratios at varying strain rates and a constant temperature of 1100°C. At high strain rates during hot compression the δ-ferrite phase gets a dendritic or vermicular morphology. Even if the temperature is high, the δ-ferrite phase has no time to dissolve into the γ-austenite phase. This leads to high aspect ratios of phases compressed at these parameters as visible in Figure 44 (d). As the strain rate decreases the aspect ratio decreases as well. The relative frequency and characteristics of the globularized phases are constantly increasing with decreasing strain rate. The lowest aspect ratio could be again observed at a temperature of 1100°C and a strain rate of 0.001 s^{-1} which is visualized in Figure 43 (d).

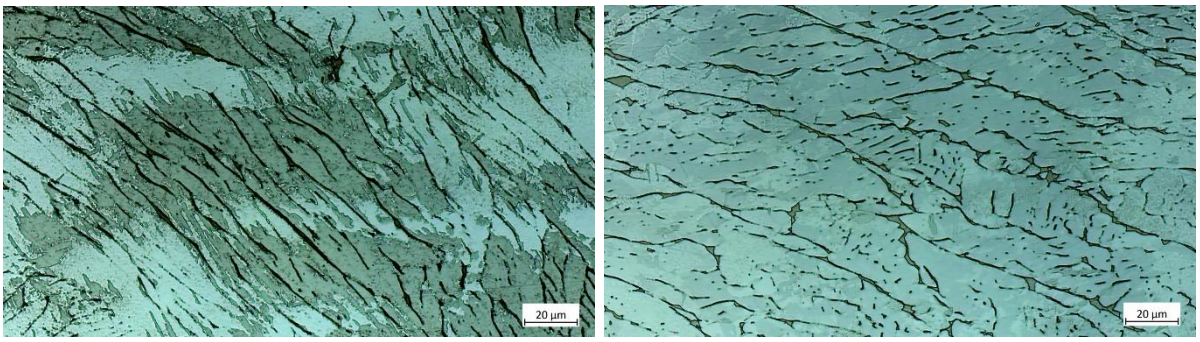

(a) (b)

Figure 45: (a) δ-ferrite phase at low temperatures of 850°C and low strain rates of 0.001 s^{-1}, (b) δ-ferrite phase at high temperatures of 1100°C and high strain rates of 10 s^{-1}.

Figure 45 (a) and Figure 45 (b) show the δ-ferrite phase and morphology of hot compressed samples at low temperatures (a) and high strain rates (b). It is visible, that the δ-ferrite phase after compression at high strain rates (a) is not shaped in the same way as the δ-ferrite phase after hot compression at low strain rates (b). At high strain rates, the phase deforms more due to the rapid deformation. The δ-ferrite phase exhibits a kinked morphology. At low strain rates on the other hand the shape of the phase has a lamellar morphology due to the hot compression.

5.3.4. Visualization of the dissolution and globularization of δ-ferrite

As already discussed in Chapter 4.5.6. Aspect ratio of δ-ferrite dissolution of δ-ferrite leads to a decrease of the aspect ratio of the δ-ferrite phase. Furthermore, the fraction of the δ-ferrite decreases as well due to dissolution of the δ-ferrite phase into the γ-austenite phase as the hot compression temperature increases and the strain rate during hot compression decreases.

Figure 46: Globularized microstructure of EBW melted AISI 304L, hot compressed at temperatures of 1100°C and a strain rate of 0.001 s^{-1}

To visualize the progress of dissolution and globularization at different hot compression parameters the orange marked values of Table 8 which shows the δ-ferrite fraction measured

by feritoscope were analyzed. The focus here was primarily on high temperatures and low strain rates, as the effect can be seen well at these hot compression parameters.

Table 8: Fraction of δ-ferrite for globularization

δ-Ferrite fraction from feritoscope [%]						
STR [s^{-1}]	800°C	850°C	900°C	950°C	1000°C	1100°C
0.001	6.2±0.1	5±0.2	4.7±0.3	3.9±0.1	2.5±0.2	1.3±0.1
0.01	6.1±0.2	5.9±0.4	6.1±0.2	5.6±0.2	4.8±0.3	4.1±0.4
0.1	6±0.2	7.1±0.3	6.9±0.5	6.5±0.4	6.5±0.3	5.9±0.6
1	6.3±0.3	6.8±0.1	6.9±0.2	7.4±0.5	8±0.3	7±0.1
10	6.1±0.3	6.8±0.2	6.3±0.3	7.2±0.2	7.3±0.3	8±0.2

The orange marked values in Table 8 are visualized in a plot diagram in Figure 47.

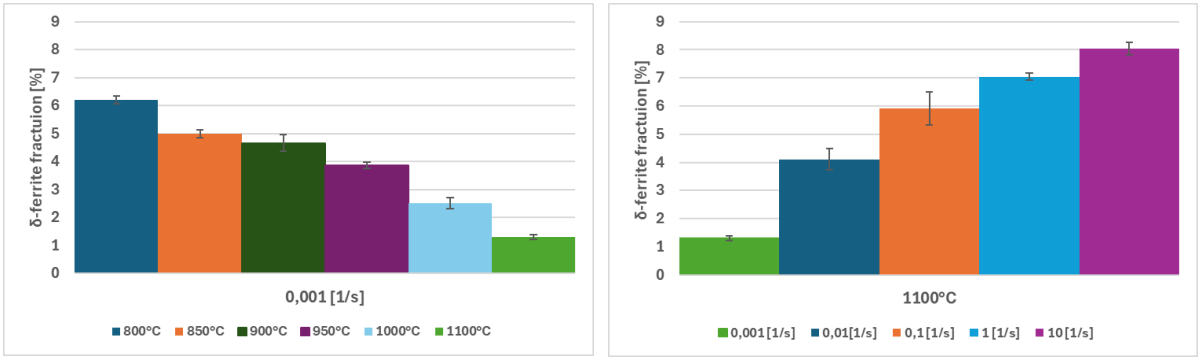

(a) (b)

Figure 47: (a) δ-ferrite fraction at different temperatures (b) δ-ferrite fraction at different strain rates

In Figure 47 (a) the fractions of the δ-ferrite phase at different temperatures are shown. In Figure 47 (b) the δ-ferrite fraction at different strain rates is visualized. The fraction of the δ-ferrite phase decreases with increasing temperatures and decreasing strain rate. The lowest value for the δ-ferrite fraction was found at hot compression parameters of 1100°C and a strain rate of 0.001 s^{-1} and is visualized in Figure 46 where the globularized δ-ferrite phase is clearly visible.

Figure 48: Microstructure of EBW melted AISI 304L, hot compressed at temperatures of 900°C and a strain rate of 0.001 s^{-1}, wet etched with Beraha 2

Figure 48 shows the δ-ferrite, where the sample was compressed at a temperature of 900°C and a strain rate of 0.001 s^{-1}. Here the dissolution process already occurs on a small scale, but due to the low temperature, mainly long δ-ferrite strings with a larger aspect ratio are present.

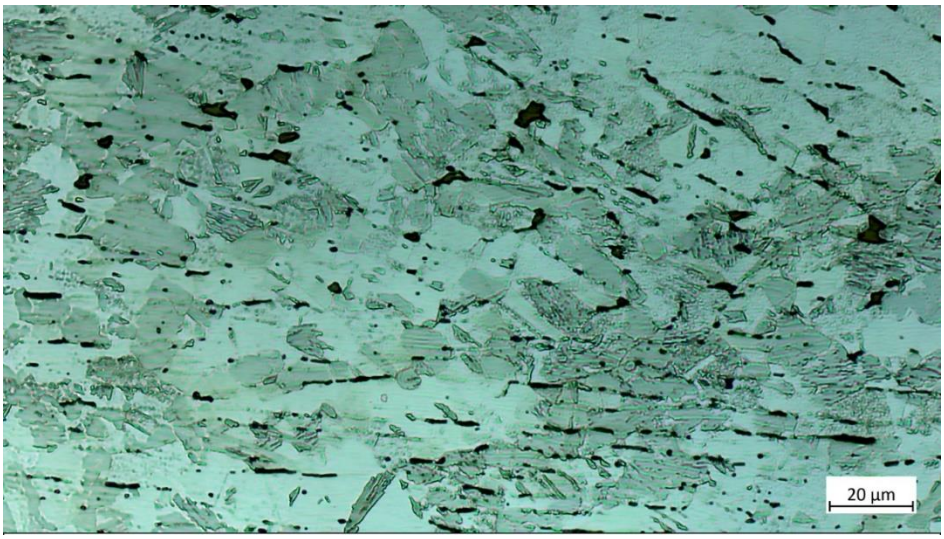

Figure 49: Microstructure of EBW melted AISI 304L, hot compressed at temperatures of 950°C and a strain rate of 0.001 s^{-1}, wet etched with Beraha 2

Figure 49 clearly shows how the dendritic or vermicular morphology ot the δ-ferrite phase splits and increasingly approaches a globular form. Several already globularized δ-ferrite phases can already be seen.

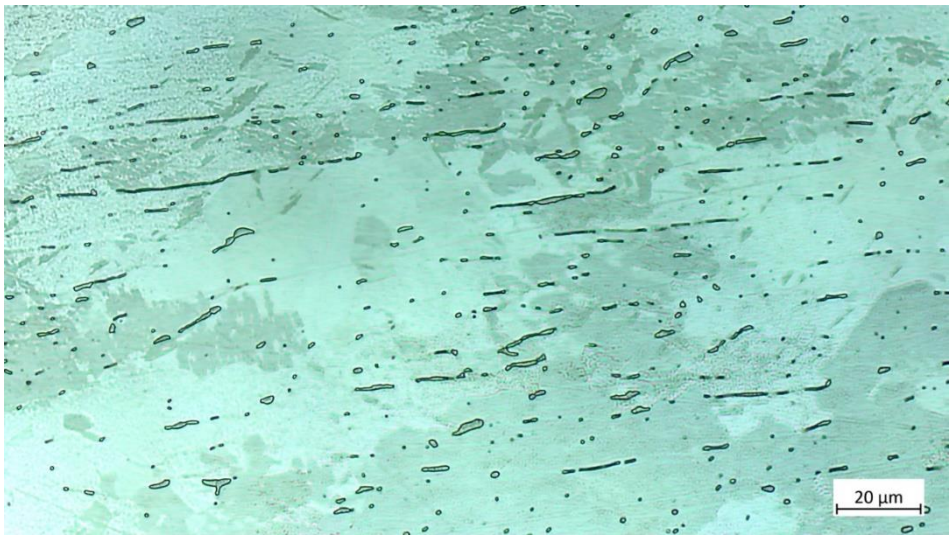

Figure 50: Microstructure of EBW melted AISI 304L, hot compressed at temperatures of 1000°C and a strain rate of 0.001 s^{-1}, wet etched with Beraha 2

In Figure 50 the hot compression temperature was 1000°C and the strain rate was at 0.001 s^{-1}. Here the globularization process is clearly visible. The δ-ferrite phase already shows a globularized structure. The remaining δ-ferrite phases start to split.

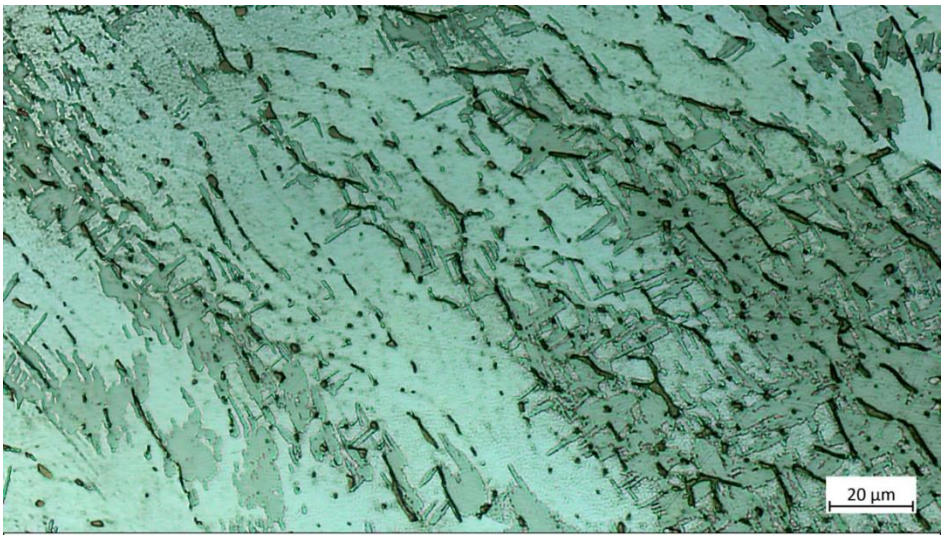

Figure 51: Microstructure of EBW melted AISI 304L, hot compressed at temperatures of 1100°C and a strain rate of 0.01 s^{-1}, wet etched with Beraha 2

In Figure 51 shows a sample which was hot compressed at a temperature of 1100°C and a higher strain rate of 0.01 s^{-1} it is also visible, that the lamellar and dendritic structures separate and the phase globularizes.

5.4. Average grain size

The average grain size and the number of grains of the hot compressed samples were investigated. Only the values for the average grains size and number of grains marked in green in Table 9 could be evaluated. For the unmarked values the evaluation was not possible because the recrystallized grainsize was not sufficient for the matlab script which was used to

analyze the images. It was not possible to investigate the samples even with the highest magnification of X1000.

Table 9: Grain size measurement

Average grain size [µm]						
STR [s^{-1}]	800°C	850°C	900°C	950°C	1000°C	1100°C
0.001	Sample 37	9.2±8.1	5.7±,5.8	13.5+-8.1	14.3±8.7	26.6±14.2
0.01	Sample 14	Sample 15	5.3±4.3	7±5.3	8.9±6.8	22.1±14.3
0.1	Sample 25	Sample 24	Sample 23	Sample 22	6.7±4.9	7.4±5.1
1	Sample 26	Sample 56	Sample 29	Sample 28	10.1±7.4	10.1±7.2
10	Sample 39	Sample 53	Sample 41	Sample 42	Sample 44	12.3±7.1

Table 9 shows the results of the average grain size measurements. The average grain size for the EBW-welded, not hot compressed reference sample was measured with a value of 255 µm ± 7 µm. The standard deviation of the measured average grain sizes is high compared with the actual values. This suggests that a lot of small but also large grains are formed during the hot compression test. The highest measured value was determined at 1100°C and a strain rate of 0.001 s^{-1} where a grainsize of 26.6 µm was visible. The lowest value that was measurable was at 900°C and a strain rate of 0.01 s^{-1} with a value of 5.7 µm.

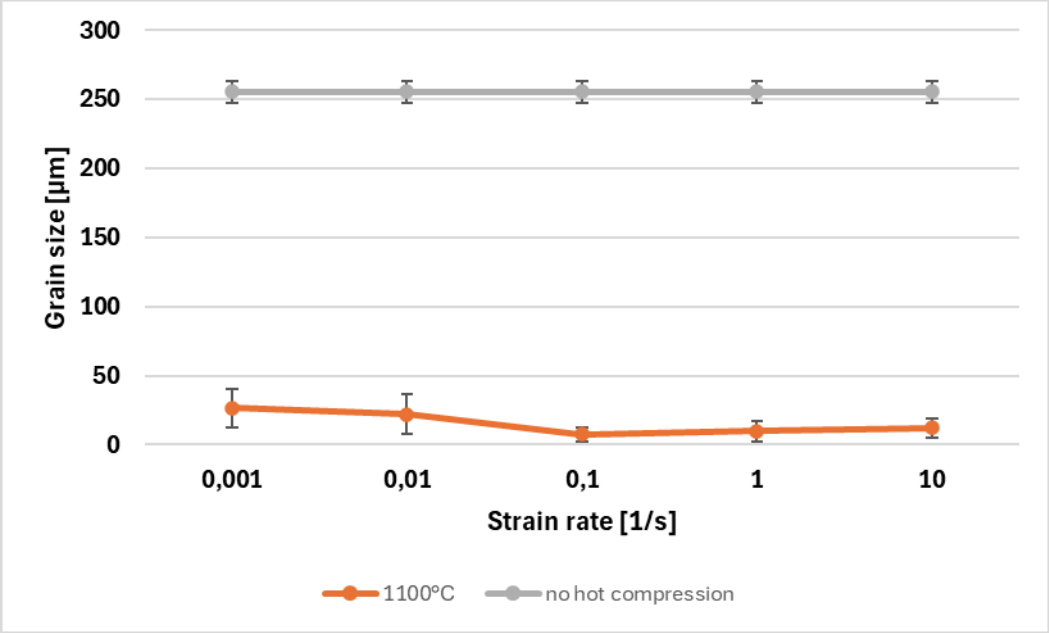

Figure 52: Grain size evolution at different strain rates and constant temperature of 1100°C

Figure 52 shows the progression of grain size at a temperature of 1100°C and different strain rates as well as the average grain size of the not hot compressed sample. At a strain rate of 0.001 s^{-1} the average grain size is at its highest and decreases as the strain rate increases to 0.1 s^{-1} where the minimum is reached with a value of 7.4 µm. The average grain size increases again between 0.1 s^{-1} and 10 s^{-1}. A large difference of the average grain size can be seen

between the hot compressed and the reference sample. This can be attributed to the recrystallization where new small strain free grains are generated.

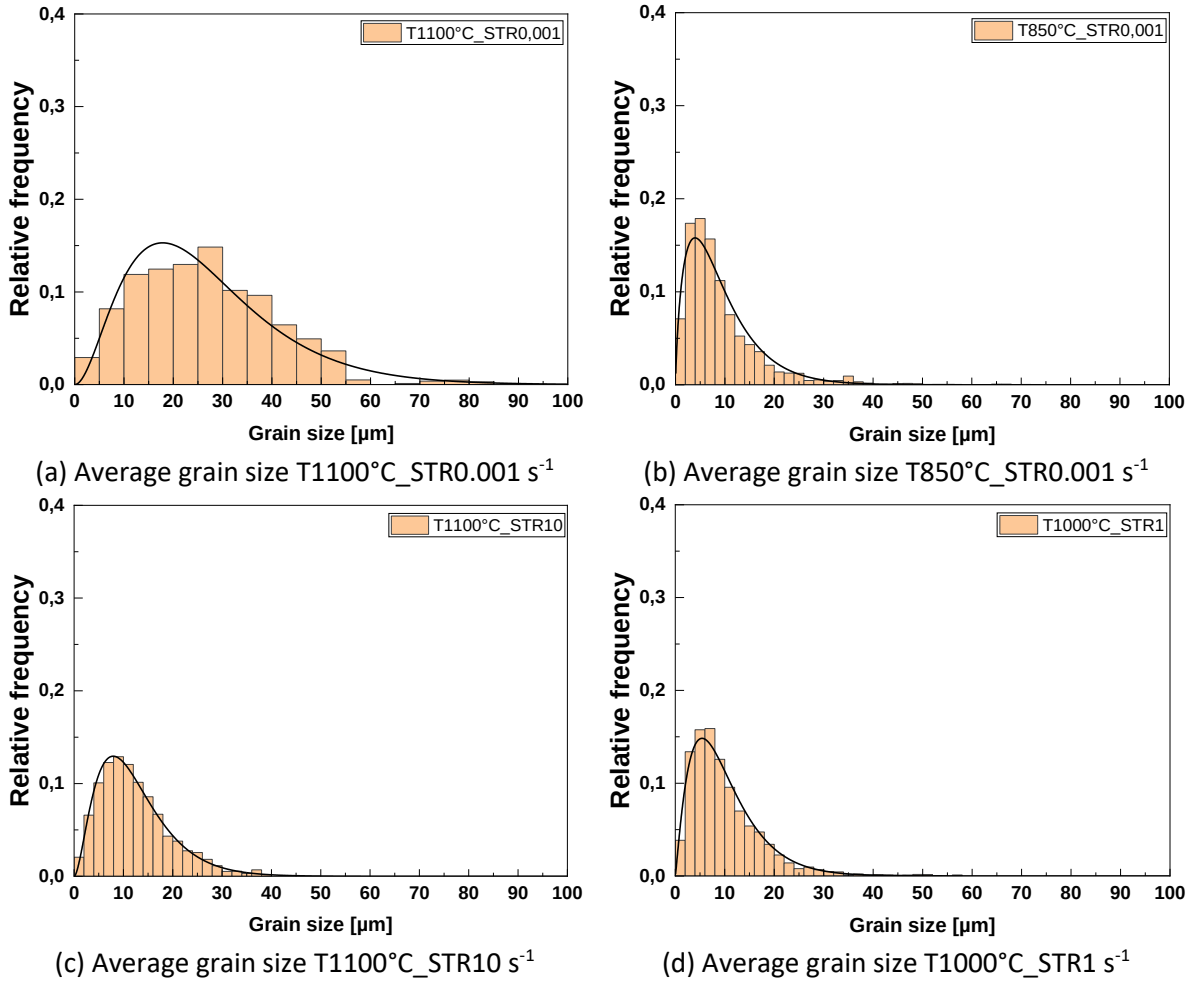

Figure 53:Comparison of the average grain size

Figure 53 shows the relative frequency of grains with a specific average grain size. Figure 53 (a) shows the average grain size of samples which were hot compressed at 1100°C and a strain rate of 0.001 s^{-1}. At these parameters large average grain sizes are visible due to the high grain growth at these parameters. The samples in Figure 53 (b) and Figure 53 (c) are hot compressed at low temperatures (b) and high strain rates (c). At these hot compression parameters, a not fully recrystallized microstructure could be observed which is illustrated in Figure 55 and Figure 57. The increase of grains with a grain size between 30 µm and 50 µm at these histograms (Figure 53 (b-c)) might be related to the not recrystallized initial grains. Also, in Figure 53 (d), a few very large grains above 50 µm are visible. These few much larger grains might also indicate a not fully recrystallized microstructure.

Figure 54 shows the fully recrystallized microstructure from a sample which was hot compressed at a temperature of 1100°C and a strain rate of 0.001 s^{-1}.

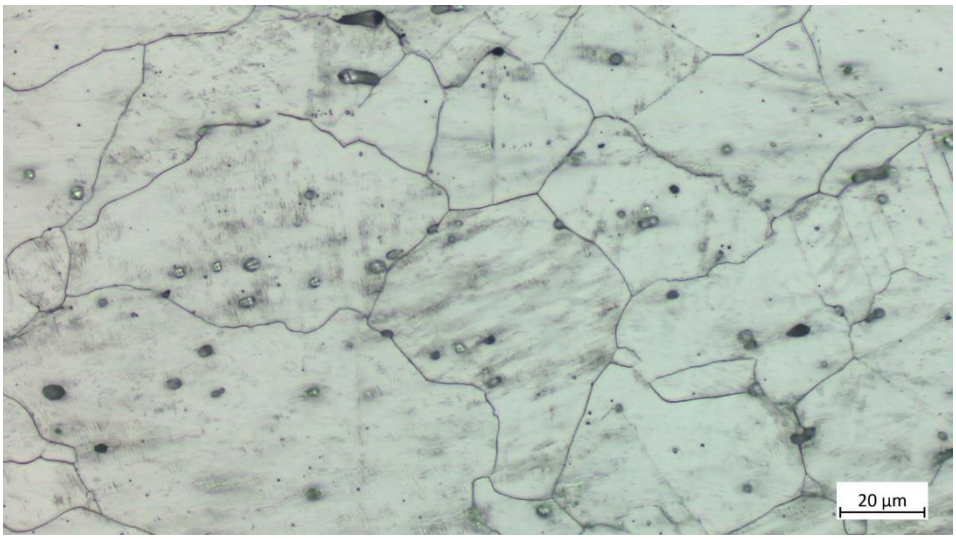

Figure 54: Microstructure of EBW melted AISI 304L, hot compressed at a temperature of 1100°C and a strain rate of 0.001 s^{-1}, electrolytic etched with 60%HNO_3 and 40%H_2O

Figure 54 shows the new formed grains after the dynamical recrystallization during hot compression. As already mentioned, the average grainsize decreases until a strain rate of 0.1 s^{-1} and increases again at higher strain rates as visible in Figure 52. This is due to the fact that at high strain rates (≥ 1) the microstructure did not have enough time to form a completely recrystallized microstructure during the hot compression test. Figure 55 shows a sample that was hot compressed at a strain rate of 10 s^{-1} and a temperature of 1100°C.

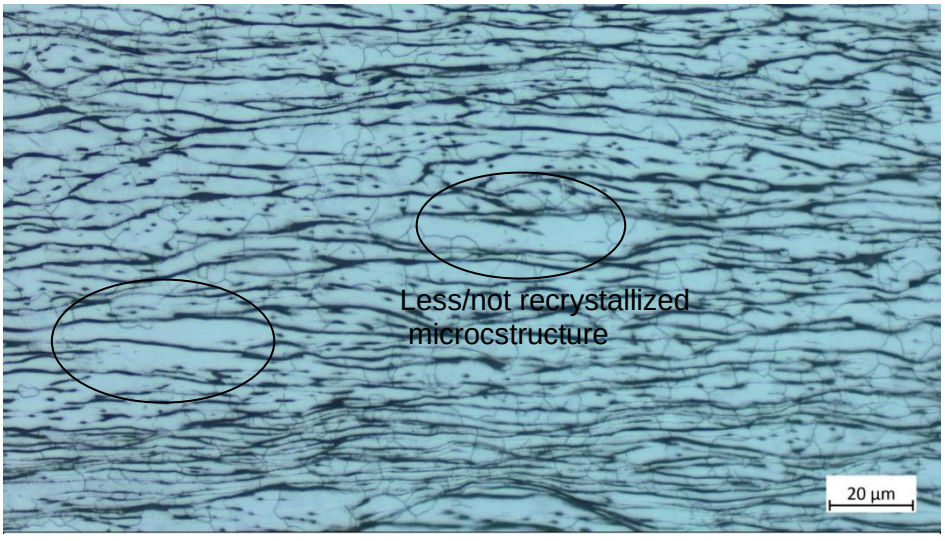

Figure 55: Microstructure of EBW melted AISI 304L hot compressed at a temperature of 1100°C and a strain rate of 10s^{-1}, electrolytic etched with 60%HNO_3 and 40%H_2O: Not fully recrystallized microstructure due to high strain rates

Zones are marked in Figure 55 where no new recrystallized grains can be found. These zones were also recognized as grains by the script and included as such in the calculation. This leads to the increasing grain size at high strain rates. These areas have a higher dislocation density than the recrystallized areas where new strain free grains can be found.

A similar behavior can be observed in Figure 56 whereby the grain size evolution at a constant strain rate of 0.001 s^{-1} and different temperatures was visualized.

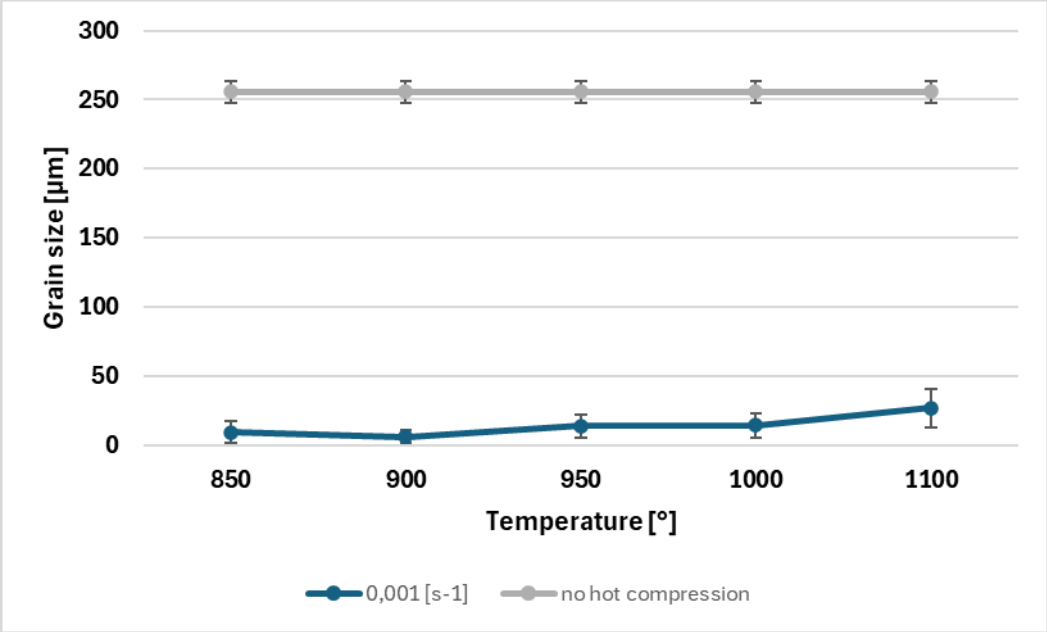

Figure 56: Grain size evolution at different temperatures and a constant strain rate of 0.001 s-1

A reduction in grain size can be observed between 850°C and 900°C. This might be attributed to the not fully recrystallized microstructure. The non-recrystallized regions are taken by the script as recrystallized regions which leads to a higher average grain size at a temperature of 850°C. Between 900°C and 1100°C the average grainsize increases again. The average grain size is at its highest at 1100°C. This can be attributed to the fact that the recrystallization and growth process is strong at high temperatures. It can also be seen in Figure 57 that at low temperatures not the entire microstructure is covered by new recrystallized grains. This further explains that an increase of the average grain size can be observed at a temperature of 850°C. The circled areas in Figure 57 shows the regions where no recrystallized grains are present.

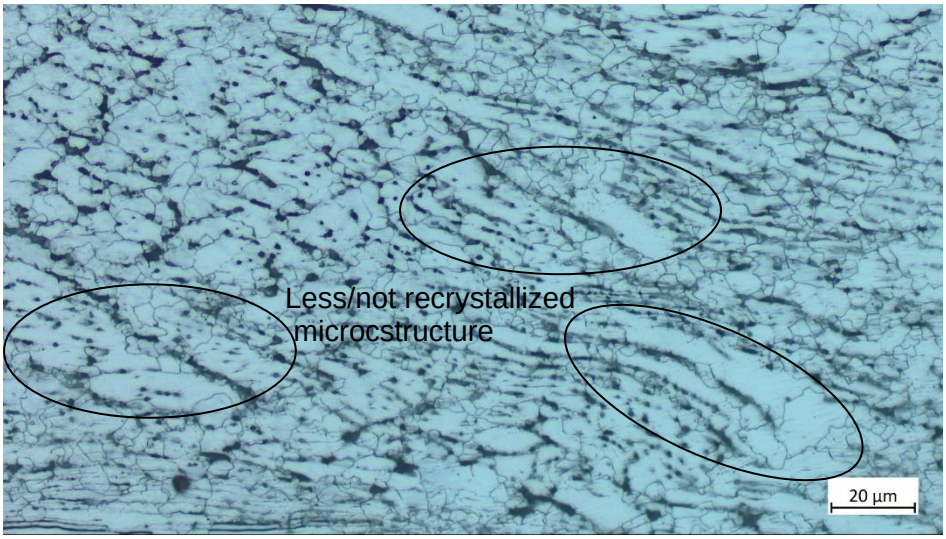

Figure 57: Microstructure of EBW melted AISI 304L hot compressed at a temperature of 900°C and a strain rate of 0.001s^{-1}, electrolytic etched with 60%HNO_3 and 40%H_2O: Not fully recrystallized microstructure due to low temperatures

Figure 58 shows a microstructure which was present after hot compression at a temperature of 850°C and a strain rate of 0.1 s^{-1}.

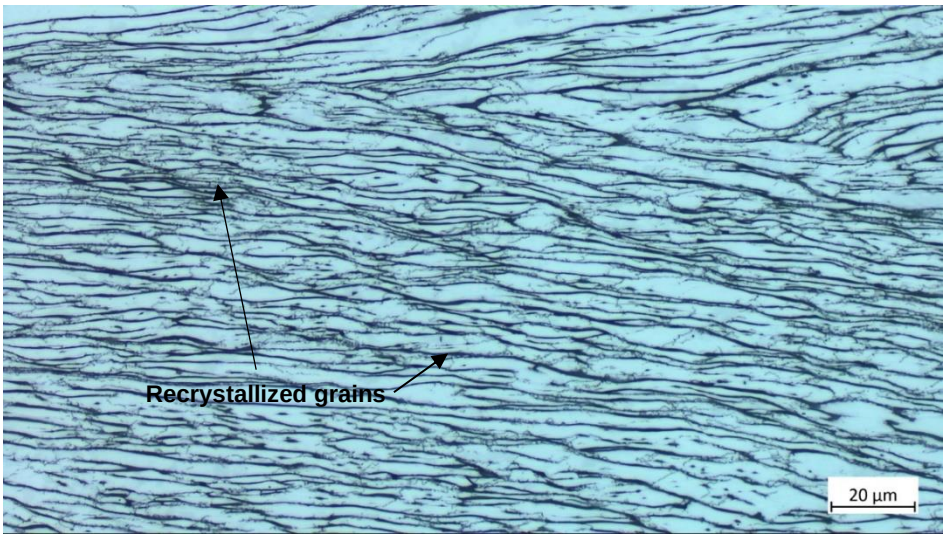

Figure 58: Microstructure of EBW melted AISI 304L hot compressed at a temperature of 850°C and a strain rate of 0.1s^{-1}, electrolytic etched with 60%HNO_3 and 40%H_2O: New dynamically recrystallized grains next to δ-ferrite due to higher dislocation density in that region

At such a small grain size, measurement using the script was not possible. New grains form mainly between the δ-ferrite and the austenitic phase. This can be attributed to the increased dislocation density in this area, which is essential for the nucleation and grain growth of the new strain free grains. In addition to the average grain size measurement, the number of grains after recrystallization was measured. The results are marked in Table 10.

Table 10: Number of grains

Number of grains						
STR [s^{-1}]	800°C	850°C	900°C	950°C	1000°C	1100°C
0.001	Sample 37	776	476	1247	269	67
0.01	Sample 14	Sample 15	1505	985	762	102
0.1	Sample 25	Sample 24	Sample 23	Sample 22	1007	305
1	Sample 26	Sample 56	Sample 29	Sample 28	511	574
10	Sample 39	Sample 53	Sample 41	Sample 42	Sample 44	291

Here also, only the results marked in green could be obtained. The measurable result correlates with the results of the average grain size measurement. Figure 59 compares the different grain sizes and the number of grains at different compression temperatures and the strain rates that are present during the hot compression test.

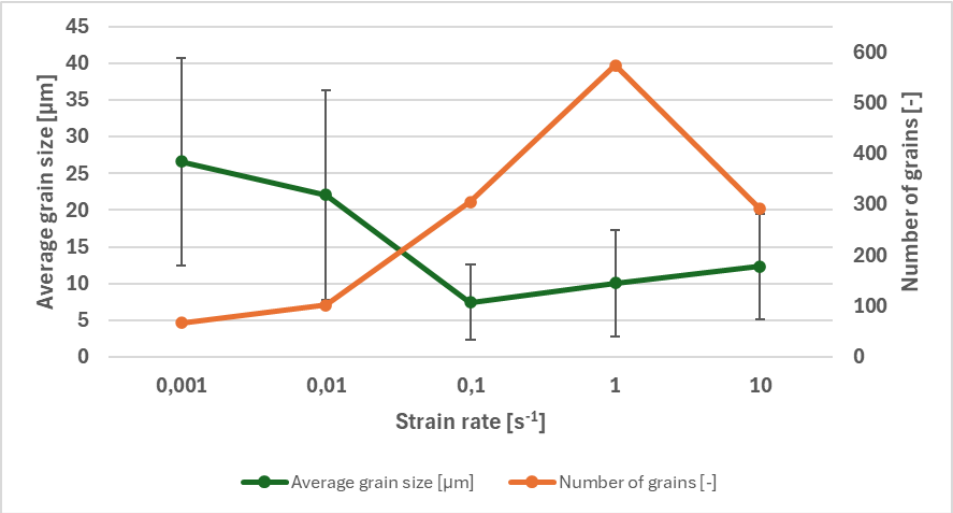

(a)

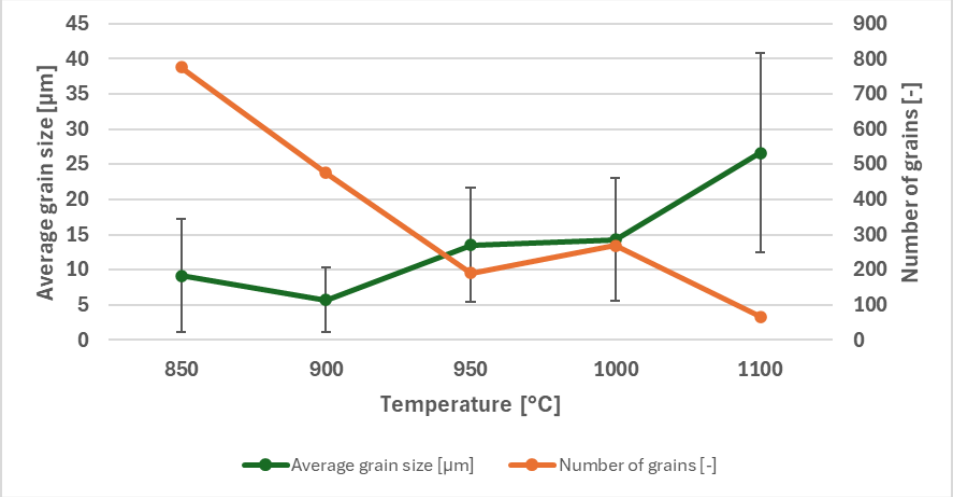

(b)

Figure 59: (a) Comparison of the average grain size with the number of grains at different strain rates and a temperature of 1100°C (b) Comparison of the average grain size with the number of grains at different temperatures at a strain rate of 0.001 s^{-1}

Figure 59 (a) shows the grain sizes and the number of grains in the observed microstructure at different strain rates at a temperature of 1100°C. At a strain rate of 0.001 s^{-1} the average grain size is large with a value 26.6±14.2 µm due to the strong recrystallization and growth process at that high temperatures and low strain rates. The number of grains in contrast is of course low at these parameters with a value of 67. With increasing strain rates, the number of grains increases whereby the average grain size decreases. At high strain rates the newly formed grains do not have enough time to grow by consuming the smaller grains during discontinuous dynamical recrystallization. At a strain rate of 1 s^{-1} the highest number of grains is present with a value of 597, while 291 grains are found at a strain rate of 10 s^{-1}. The reason for this is that the average grain size is growing again due to a not fully recrystallized microstructure.

Figure 59 (b) shows the average grain size and the number of grains at different temperatures and a constant strain rate of 0.001 s^{-1}. It can be seen, that at decreasing temperatures the

average grain size is also decreasing, and the number of grains is high with 776 grains with an average grain size of 9.2±8.1 µm. Between temperatures of 850°C and 900°C the average grain size decreases. This can be attributed to the microstructure which is not fully recrystallized due to the low temperatures. A certain temperature is needed for the dynamical recrystallization process. Between 900°C and 1100°C the grain size increases steadily while the number of grains decreases further. At a temperature of 1100°C and a strain rate of 0.001 s^{-1} the lowest number of grains with a value of 67 and the largest average grain size with a size of 26.6±14.1 µm is present. The standard deviation is large at samples which were hot compressed at high temperatures and low strain rate. Due to recrystallization and grain growth large grains are also present alongside new small grains. This leads to a large standard deviation of the measured values. At higher strain rates and lower temperatures, it is not changing significantly.

5.5. Hardeness test

The hardness was measured in the area of interest and the results are shown in Table 11.

Table 11: Hardness

Hardness [HV0.5]						
STR [s^{-1}]	**800°C**	**850°C**	**900°C**	**950°C**	**1000°C**	**1100°C**
0.001	279±12	239±7	223±6	204±5	196±5	186±7
0.01	294±10	261±9	247±9	228±7	223±6	191±6
0.1	288±12	258±9	262±8	253±9	299±13	209±5
1	240±6	294±9	280±11	260±8	252±7	228±5
10	278±9	282±13	282±9	272±9	264±8	218±7

Figure 60 visualizes the hardness at different strain rates and temperatures. The hardness of the not hot compressed reference sample was 195±10 HV 0.5.

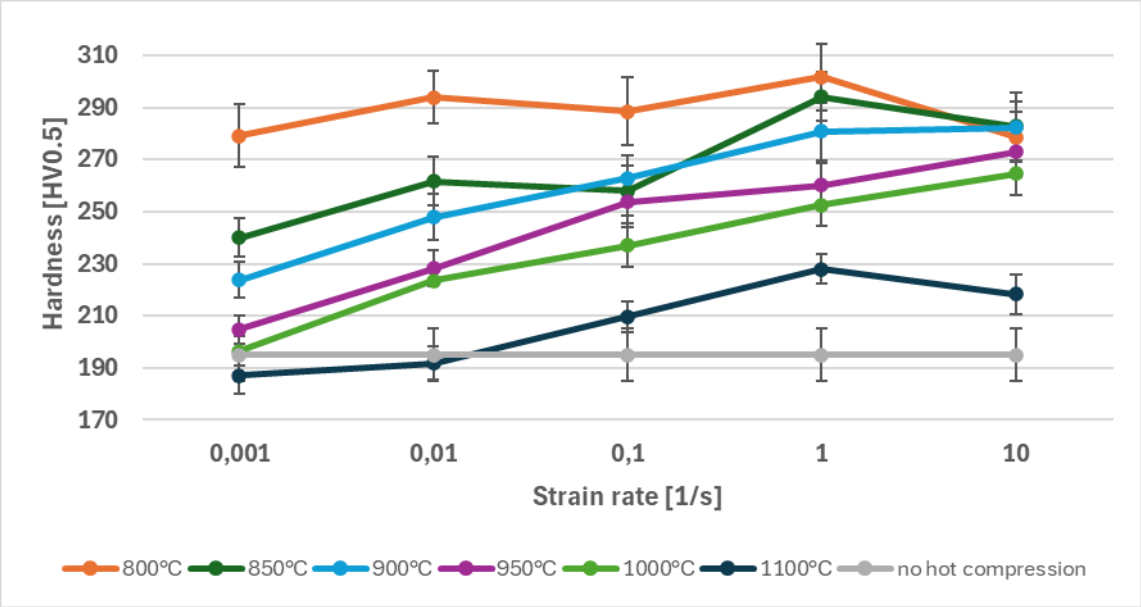

Figure 60: Hardness at different strain rates

Work hardening increases with increasing strain rate. This leads further to an increase of the dislocation density in the microstructure which additionally leads to a higher hardness of the material. At low strain rates the recrystallization phenomenon is more present and therefore flow softening increases. Further the δ-ferrite fraction decreases at decreasing strain rates due to the dissolution of the δ-ferrite phase, which promotes a softer material. The resulting reduction of the dislocation density rich interface between the δ ferrite phase and the γ-austenite phase also promotes softening. But the hardness also strongly depends on the deformation temperature as visible in Figure 61.

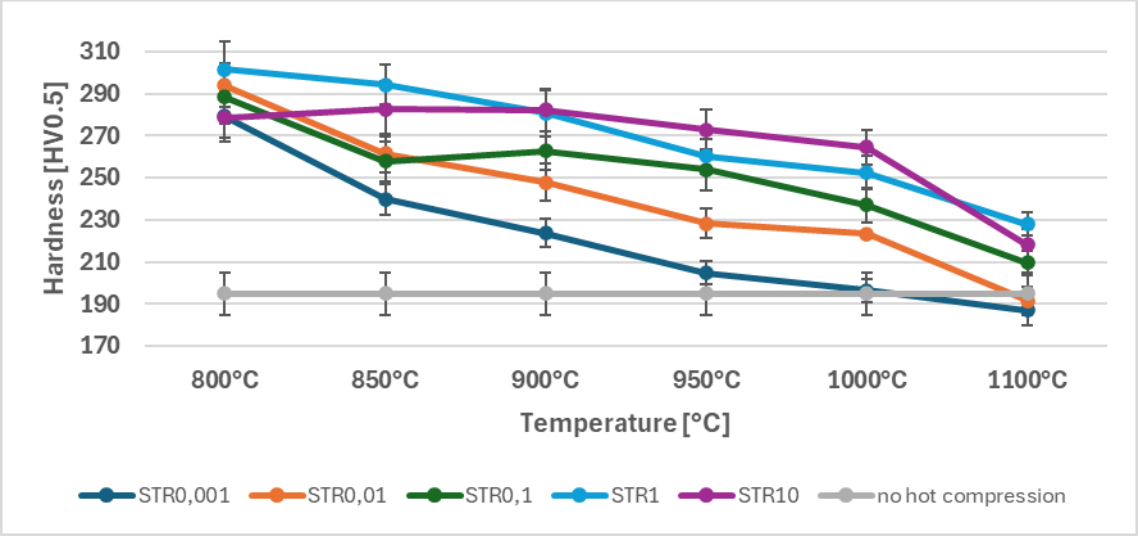

Figure 61: Hardness at different temperatures

Figure 61 shows that the hardness is decreasing with increasing temperatures. At lower temperatures the dislocation formation is higher and therefore the hardness also increases. Furthermore, the dissolution of the δ-ferrite phase at low temperatures is weak. This explains the high hardness at low temperatures and high strain rates.

By increasing the temperature recrystallization gets stronger. New strain free grains with a decreased dislocation density are present. High temperatures also promote the δ-ferrite dissolution, which results in a softer material. At hot compression parameters of 1100°C and strain rates of 0.001 s^{-1} and 0.01 s^{-1} the material is less hard than the reference sample.

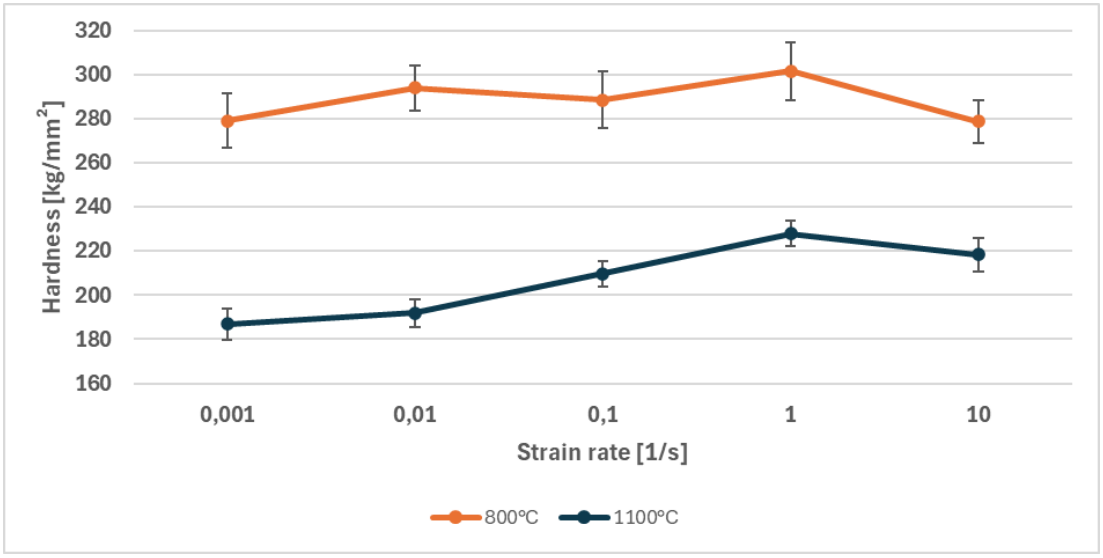

(a)

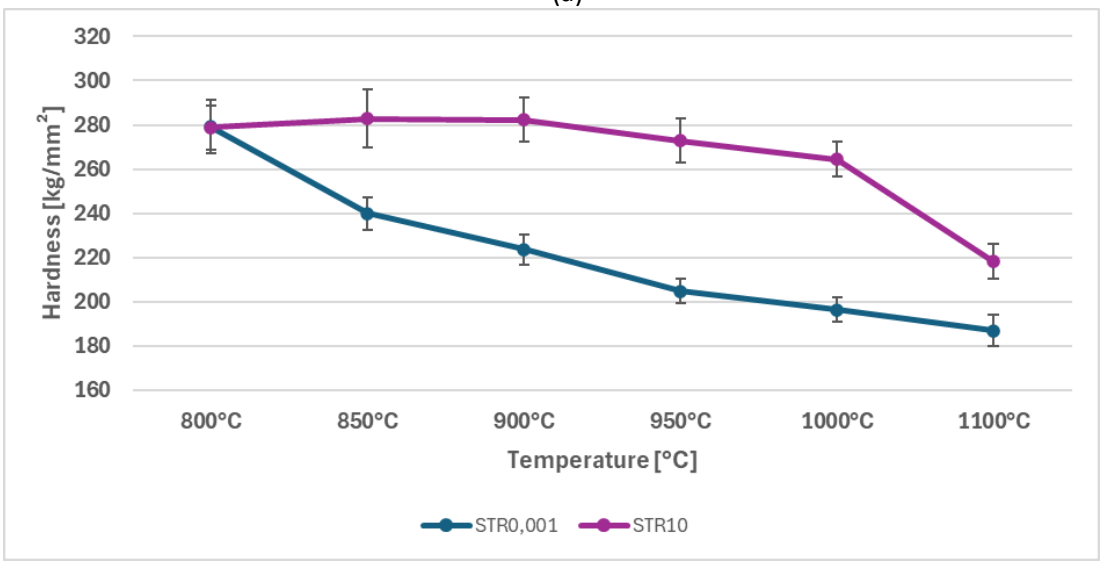

(b)

Figure 62: (a) Hardness with standard deviation at 800°C and 1100°C (b) Hardness with standard deviation at a strain rate of 0.001 s^{-1} and 10 s^{-1}

Figure 62 shows the Vickers hardness curves at different hot compression parameters with the calculated standard deviation. In Figure 62 (a) it is visible, that the standard deviation is generally higher at lower temperatures. Figure 62 (b) shows that the standard deviation is also higher at high strain rates. This can be attributed to the different phases present at these hot compression parameters whereby it is possible that measurement points were made at the harder δ-ferrite phase. Also, there is no fully recrystallized microstructure at low temperatures

and high strain rates. Due to that fact, regions with a high dislocation density are present which show a higher hardness.

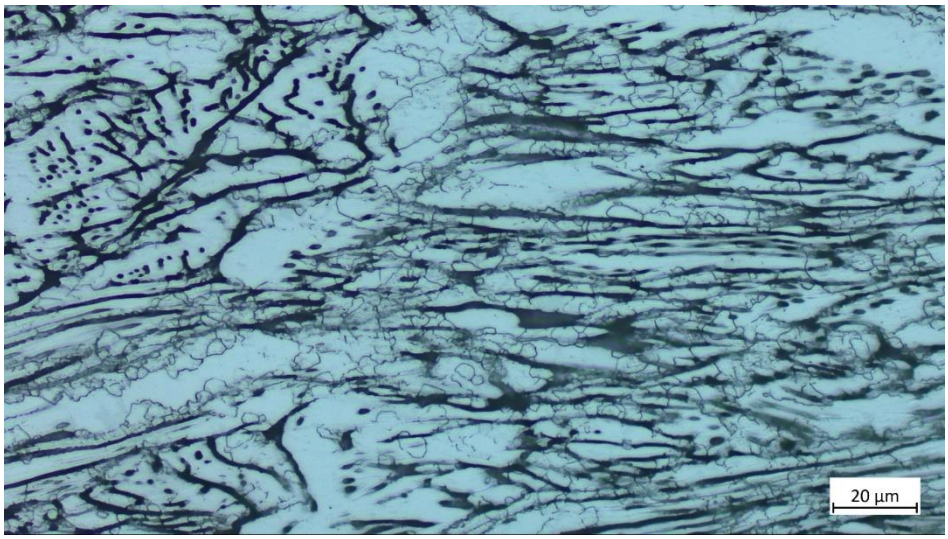

Figure 63: Microstructure of EBW melted AISI 304L hot compressed at a temperature of 1000°C and a strain rate of 0.1 s^{-1}, electrolytic etched with 60%HNO_3 and 40%H_2O

A not fully recrystallized microstructure is shown in Figure 63. The different phases are clearly visible. Also, the recrystallized zones and the initial microstructure are present.

5.6. Summary

Table 12 shows the properties of AISI 304L stainless steel at various strain rates and a hot compression temperature of 1100°C. The values for the temperature during hot compression were selected here, as the values of the δ-ferrite content measurement via image analysis and the grainsize measurement were successful at these parameters.

Table 12: Comparison of the fraction from image Analysis [%], fraction from Feritoscope [%], grain size [µ] and aspect ratio [-] at different strain rates

	Temperature 1100°C				
Strain rate [s^{-1}]	**Hardness [HV0,5]**	**Average grain size [µm]**	**Fraction from Feritoscope [%]**	**Fraction from image Analysis [%]**	**Aspect ratio [-]**
0.001	186±7	26.6±14.2	1.3±0.1	1.6±0.8	1.8±0.2
0.01	191±6	22.1±14.3	4.1±0.4	3.9±1.5	2.7±0.4
0.1	209±5	7.4±5.2	5.9±0.6	6.4±1.3	2.3±0.2
1	228±5	9.9±7.2	7±0.1	6.8±2.3	2.7±0.3
10	218±7	12.3±7.1	8±0.2	9.2±1.2	3.5±0.7

The properties listed in Table 11 are displayed in Figure 64. The δ-ferrite fraction from image analysis, δ-ferrite fraction from feritoscope, grain size and aspect ratio are shown on the primary axis. The vertical secondary axis shows the values for hardness.

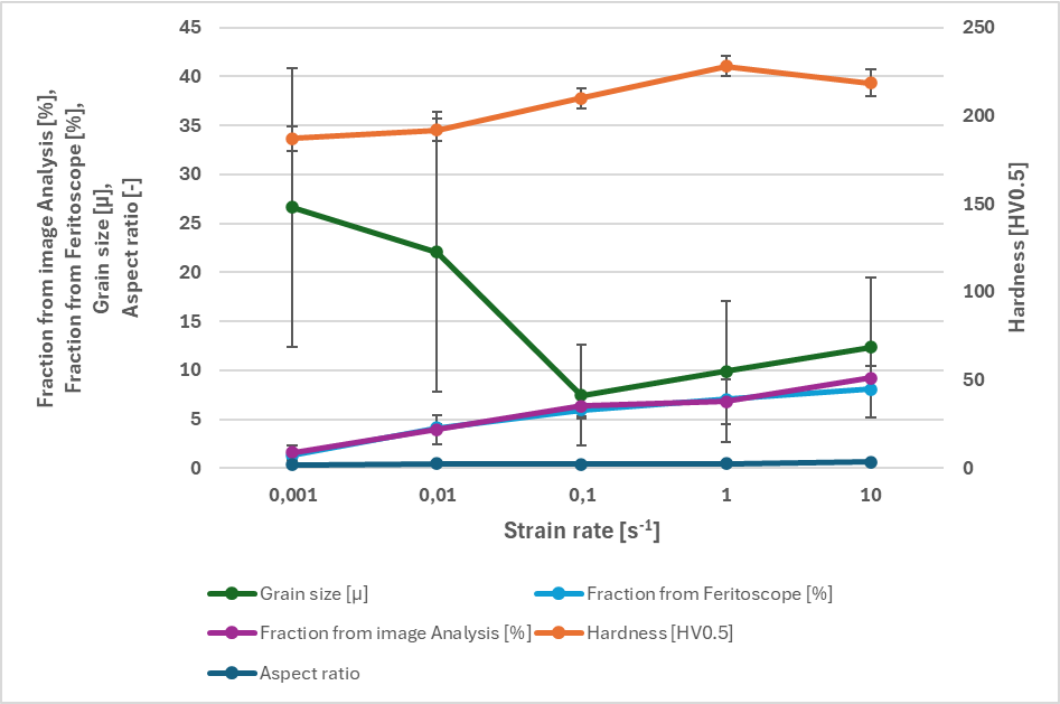

Figure 64: Result comparison at different strain rates and at a temperature of 1100°C

Higher strain rates (≥ 0.1 s^{-1}) lead generally to a higher formation of dislocations in the microstructure whereby work hardening plays a major role in the process. At low strain rates below 0.1 s^{-1} the recrystallization process was stronger as discussed in 5.1.1. This leads to a lower dislocation density in the material.

Figure 64 shows that the hardness is lowest with a value of 186±7.2 HV 0.5 at the lowest measured strain rate of 0.001 s-1. This is accompanied by a large recrystallized average grain size of 26.6±14.1 µm. Those annihilate the old dislocation-rich microstructure and thus form new grains. Due to the low strain rate, the dislocation density is only slightly increased by work hardening and recrystallization is stronger at these parameters. Dislocations are formed at interfaces between different phases and therefore the dislocation density is generally very high in this area. This means that the fraction and the aspect ratio of the δ-ferrite phase plays a major role in the interaction of the properties, as this is related to the dislocation density. It can be seen that the aspect ratio measured with image analysis method and the δ-ferrite fraction measured with feritoscope are also low with values of 1.3%±0.1% for the fraction and 1.8±0.2 for the aspect ratio at low strain rates. This is due to the globularization of δ-ferrite which can be recognized at increasing temperatures and at strain rates below 0.1 $s^{-1.}$

For the properties between the strain rates 0.001 s^{-1} and 0.1 s^{-1}, it can be seen that the hardness increases with increasing strain rate. The grain size decreases rapidly. The δ-ferrite value increases with increasing strain rates at these parameters. The δ-ferrite value obtained

with the help of image analysis and measured using a feritoscope increases in this range. The aspect ratio of the δ-ferrite also increases.

At high strain rates between 0.1 s^{-1} and 10 s^{-1}, an increase and a minimal drop in hardness can be observed between strain rate 1 s^{-1} and 10 s^{-1}. The grain size also increases in this range. As already discussed, this is due to the fact that not the entire microstructure is recrystallized which leads to larger grains with the initial strained microstructure. The δ-ferrite fraction value increases with increasing strain rate as well as the aspect ratio.

Table 13 shows the values of the measurements of the mentioned properties of the sample at a strain rate of 0.001 s^{-1}. This value was used since reliable results were only available for the δ-ferrite fraction image analysis and the grain size analysis at this strain rate.

Table 13:Comparison of the fraction from image Analysis [%], fraction from Feritoscope [%], grain size [µ] and aspect ratio [-] at different temperatures

	Strain rate 0.001 s^{-1}				
Temperature [°C]	**Hardness [HV0.5]**	**Average grain size [µm]**	**Fraction from feritoscope [%]**	**Fraction from image analysis [%]**	**Aspect ratio [-]**
850	239 ±7	9.2±8,1	5±0.2	7±2.3	2.8±0.2
900	223 ±6	5.-7±4.6	4.7±0.3	4.7±1.2	2.1±0.1
950	204 ±5	6.7±5.2	3.9±0.1	3.9±1.2	2.5±0.3
1000	196±5	14.3±8.7	2.5±0.2	3.4±1.9	2.4±0.3
1100	186 ±7	26.6±14.2	1.3±0.1	1.6±0.8	1.8±0.2

The values of Table 13 are now plotted in a line diagram which is visible in Figure 65. Again, the fraction from image analysis, fraction from feritoscope, grain size and aspect ratio are displayed on the primary vertical axis. The hardness is shown on the secondary axis.

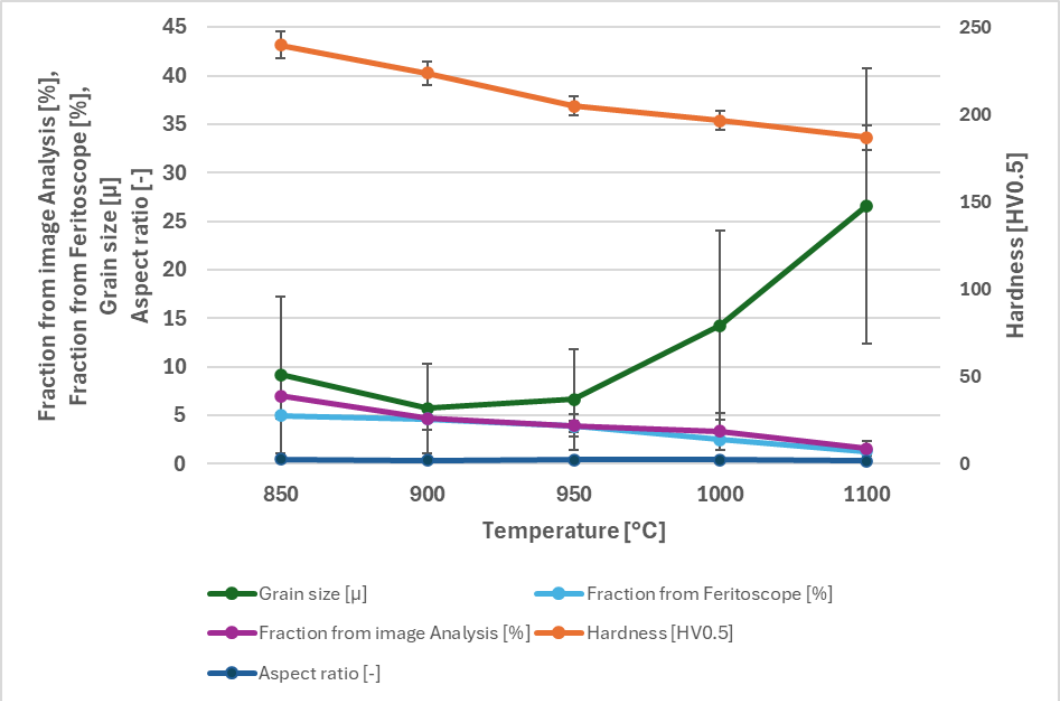

Figure 65: Result comparison at different temperatures and at a strain rate of 0.001 s^{-1}

At low temperatures of 850°C, a high hardness value of 239±7 HV 0.5 can be determined. At hot compression temperatures below 1000°C, there is only a weak recrystallization and recovery process. If a workpiece is now hot compressed, dislocation formation due to work hardening predominates. More dislocation in the microstructure means more hardness.

The grain size is also influenced by this. It can be seen that it decreases in the range between 850°C and 900°C. Due to the low temperatures during the hot compression test, not all of the observed surface was recrystallized, similar to high strain rates. In some cases, the initial, non-recrystallized microstructure can still be seen. The δ-ferrite content is highest at 850°C with a value of 239.9±7.3%. It can also be seen here that the deviation of the values at low temperatures between the δ-ferrite fraction measured with the image analysis method and the feritoscope differs the most. The aspect ratio of the δ-ferrite is also high with a value of 2.8±0.2 at 850°C.

Due to recrystallization, the grain size also increases with increasing temperatures, with the strongest increase measured between 950°C and 1100°C. At this hot compression parameter the grain size was 26.6±14.2 µm.

Due to the increasing globularization of the δ-ferrite, the fraction and the aspect ratio of the δ-ferrite decreases with increasing temperatures.

At temperatures of 1100°C during hot compression, a comparatively soft microstructure consisting of large new grains is obtained, with a low δ-ferrite fraction which is globularized.

6. Conclusions

Based on the results, the following conclusions can be derived.

(I) Flow stress curves

- The flow stress curves show a higher flow stress at increasing strain rates and decreasing temperatures. At a temperature of 800°C and a strain rate of 10 s^{-1} the flow stress was highest. This leads to the conclusion that work hardening increases with decreasing hot compression temperatures and increasing strain rates.
- With increasing deformation temperatures and decreasing strain rates, the dominance of recrystallisation over work hardening increases.
- At high strain rates of 10 s^{-1} which lead to short deformation times, the adiabatic heating during deformation was stronger with values between 5°C to 13°C than at samples, which were hot compressed at lower strain rates. This indicates that the accumulated adiabatic heat could not be transferred to the surrounding area at too high strain rates. At low strain rates of 0.001 s^{-1} the ΔT was between 0 and 0.35 °C.

(II) δ-ferrite

- The δ-ferrite fraction changes strongly with the temperature and strain rate during the hot compression test. This can be attributed to the dissolution of the δ-ferrite phase into the austenitic phase. At increasing temperatures and decreasing strain rates during hot compression, the dissolution is strong.
- The form of the δ-ferrite changes drastically at high temperatures (≥ 1000°C) and low strain rates (≤ 0.01 s^{-1}). The lamellar, vermicular and dendritic shaped changes with a decreasing δ-ferrite phase due to the dissolution to a globular morphology.
- The highest δ-ferrite value was observed at the EBW welded not hot compressed reference sample with a value of 9.6% ±1.6%.
- 8.04% of δ-ferrite were observed at high deformation temperatures (1100°C) and high strain rates (10 s^{-1}). Low values of 1.3% of the δ-ferrite fraction were found at high temperatures (1100°C) and low strain rates (0.001 s^{-1}).
- At high temperatures of 1100°C the δ-ferrite fraction changes strongest over the different strain rates. At 800°C on the other hand no drastic change in the δ-ferrite fraction is visible.
- The determination of the δ-ferrite fraction and the aspect ratio measured with image analysis method is difficult at samples which were hot compressed at high strain rates and low temperatures. The measurement with the feritoscope showed more trustworthy results for these parameters.

(III) Average grain size

- New recrystallized strain free grains with a decreased dislocation density are mainly present in samples which were hot compressed at temperatures ≥ 950°C. At low strain rates below 0.1 s^{-1} during hot compression the grain size increases. This can be attributed to the long exposure time to the increased temperatures, whereby the microstructure had more time for the grain growth process.
- At hot compression temperatures below 950°C, the dynamic recrystallization is also low. A certain thermal energy is needed for the discontinuous dynamic recrystallization process to occur. Recrystallization increases with increasing temperatures.
- The newly dynamically recrystallized grains are particularly visible in the dislocation-rich interface between the δ-ferrite phase and the austenitic phase.
- In samples which are hot compressed at high strain rates above 1 s^{-1} or low temperatures below 900°C it can be seen that not the full microstructure is recrystallized. There parts of the microstructure did not recrystallize whereby the initial microstructure is present.

(IV) Hardness

- The hardness increases with decreasing temperatures and increasing strain rates. The highest hardness with a value of 264.5±8 HV 0.5 was measured at a temperature of 800°C and a strain rate of 1 s^{-1}. At these hot compression parameters, the dislocation density is high due to the lack of dynamic recrystallization.
- On the other hand, the lowest hardness with a value of 187±7.1 HV was measured at 1100°C and a strain rate of 0.001 s^{-1} where a fully recrystallized microstructure was present. Furthermore, a δ-ferrite fraction with a value of 131% also contributed to the low hardness value.

7. Outlook

In the δ-ferrite measurements to determine the aspect ratio and the δ-ferrite fraction, but also in the determination of the grain size via the image analysis method, measured values could not be obtained at low temperatures and high strain rates due to the difficult etching method.
In the grain size measurement, the newly recrystallized grains were too small for the evaluation script used at low temperatures and high strain rates.
In order to obtain reliable values for these problems, an Electron backscatter diffraction (EBSD) measurement must subsequently be carried out. This makes it possible to accurately measure the δ-ferrite phase. Even the smallest newly dynamically recrystallized grains can be detected with this measurement method.

8. References

1. Humphreys, F.J., Hatherly, M.: Chapter 13 - Hot Deformation and Dynamic Restoration. In: Humphreys, F.J. and Hatherly, M. (eds.) Recrystallization and Related Annealing Phenomena (Second Edition). pp. 415–V. Elsevier, Oxford (2004)
2. Liss, K.-D., Xu, P., Shiro, A., Zhang, S., Yukutake, E., Shobu, T., Akita, K.: Abnormal Grain Growth: A Spontaneous Activation of Competing Grain Rotation. Adv Eng Mater. 26, 2300470 (2024). https://doi.org/https://doi.org/10.1002/adem.202300470
3. Burke, J.E., Turnbull, D.: Recrystallization and grain growth. Progress in Metal Physics. 3, 220–292 (1952). https://doi.org/https://doi.org/10.1016/0502-8205(52)90009-9
4. Knipschildt, E.F.F.: Nucleation of recrystallization. Materials Science and Technology. 38, 765–779 (2022). https://doi.org/10.1080/02670836.2022.2065054
5. Zhang, S., Wang, Q., Cheng, X., Han, J., Zhang, W., Zhang, C., Wu, J.: Static Recrystallization Behavior and Texture Evolution during Annealing in a Cold Rolling Beta Titanium Alloy Sheet. Metals (Basel). 12, (2022). https://doi.org/10.3390/met12060899
6. Grätz, K.: The Transient to Steady-State: A Mobility Based Approach on Dynamic Recrystallization, (2015)
7. Goetz, R.L., Seetharaman, V.: Static recrystallization kinetics with homogeneous and heterogeneous nucleation using a cellular automata model. Metallurgical and Materials Transactions A. 29, 2307–2321 (1998). https://doi.org/10.1007/s11661-998-0108-z
8. Huang, K., Logé, R.E.: A review of dynamic recrystallization phenomena in metallic materials. Mater Des. 111, 548–574 (2016). https://doi.org/https://doi.org/10.1016/j.matdes.2016.09.012
9. Zhong, X., Huang, L., Wang, L., Liu, F., Dong, X., Zhang, Z.: A discontinuous dynamic recrystallization model incorporating characteristics of initial microstructure. Transactions of Nonferrous Metals Society of China. 28, 2294–2306 (2018). https://doi.org/https://doi.org/10.1016/S1003-6326(18)64874-5
10. Material Data Sheet Stainless Steel 1.4307 - 304L. (2017). Thyssenkrupp
11. Bijish Babu: Physically Based Model for Plasticity and Creep of Ti-6Al-4V, 25
12. Shirdel, M., Mirzadeh, H., Parsa, M.H.: Abnormal grain growth in AISI 304L stainless steel. Mater Charact. 97, 11–17 (2014). https://doi.org/https://doi.org/10.1016/j.matchar.2014.08.022
13. Dutta, S.: Different Types and New Applications of Stainless Steel. 62, 86–91 (2018). Iron & Steel Review
14. Jeong, J., Lee, Y., Park, J.M., Lee, D.J., Jeon, I., Sohn, H., Kim, H.S., Nam, T.-H., Sung, H., Seol, J.B., Kim, J.G.: Metastable δ-ferrite and twinning-induced plasticity on the strain hardening behavior of directed energy deposition-processed 304L austenitic stainless steel. Addit Manuf. 47, 102363 (2021). https://doi.org/https://doi.org/10.1016/j.addma.2021.102363
15. Lothongkum, G., Viyanit, E., Bhandhubanyong, P.: Study on the effects of pulsed TIG welding parameters on delta-ferrite content, shape factor and bead quality in orbital welding of AISI 316L stainless steel plate. J Mater Process Technol. 110, 233–238 (2001). https://doi.org/https://doi.org/10.1016/S0924-0136(00)00875-X
16. Kim, S.H., Moon, H.K., Kang, T., Lee, C.S.: Dissolution kinetics of delta ferrite in AISI 304 stainless steel produced by strip casting process. Materials Science and Engineering: A. 356, 390–398 (2003). https://doi.org/https://doi.org/10.1016/S0921-5093(03)00152-7
17. Rezayat, M., Mirzadeh, H., Namdar, M., Parsa, M.H.: Unraveling the Effect of Thermomechanical Treatment on the Dissolution of Delta Ferrite in Austenitic Stainless Steels. Metallurgical and Materials Transactions A. 47, 641–648 (2016). https://doi.org/10.1007/s11661-015-3242-4
18. Arh, B., Tehovnik, F., Vode, F.: Transformation of the δ-Ferrite in SS2343 Austenitic Stainless Steel upon Annealing at 1050 °C, 1150 °C and 1250 °C. Metals (Basel). 11, (2021). https://doi.org/10.3390/met11060935
19. de Souza Ciacco, P.: Study of the Formation and Dissolution of δ-ferrite During High Temperature Forging Processing of Austenitic, Martensitic and PH Stainless Steels, (2023). Master Thesis. University of Pittsburgh https://d-scholarship.pitt.edu/44265/1/DF_Pedro%20MS%20Thesis%20FINAL%20After%20Corrections.pdf

20. P N, S., Sathiya Narayanan, C.: A review on Electron Beam Welding process. J Phys Conf Ser. 1706, 12208 (2020). https://doi.org/10.1088/1742-6596/1706/1/012208
21. Węglowski, M.St., Błacha, S., Phillips, A.: Electron beam welding – Techniques and trends – Review. Vacuum. 130, 72–92 (2016). https://doi.org/https://doi.org/10.1016/j.vacuum.2016.05.004
22. Dr. G. Schubert: Electron Beam Welding - Process, Application and Equipment. PTR-Precision Technologies Inc.
23. Guo, J., Tang, C., Rothwell, G., Li, L., Wang, Y.-C., Yang, Q., Ren, X.: Welding of High Entropy Alloys—A Review. Entropy. 21, (2019). https://doi.org/10.3390/e21040431
24. Ho, K.H., Newman, S.: State of the art electrical discharge machining (EDM). Int J Mach Tools Manuf Des Res Appl. Int J Mach Tools Manuf. 43, 1287–1300 (2003). https://doi.org/10.1016/S0890-6955(03)00162-7
25. Arun Babu, K., Athreya, C.N., Mozumder, Y.H., Subramanya Sarma, V., Mandal, S.: A Comprehensive Study on Texture Development and Twin-Related Domain Evolution Following Hot Compression in a Super Austenitic Stainless Steel. Metallurgical and Materials Transactions A. 51, 3535–3551 (2020). https://doi.org/10.1007/s11661-020-05763-8
26. Goetz, R.L., Semiatin, S.L.: The adiabatic correction factor for deformation heating during the uniaxial compression test. J Mater Eng Perform. 10, 710–717 (2001). https://doi.org/10.1361/105994901770344593
27. Abd El-Aty, A., Xu, Y., Zhang, S.H., Guo, X., Tao, J., Lee, M.: Phenomenological-based constitutive modelling of warm deformation behavior of high-Strength lightweight AL-Li alloy sheets. IOP Conf Ser Mater Sci Eng. 1238, 12017 (2022). https://doi.org/10.1088/1757-899X/1238/1/012017
28. Chen, H., Qin, H., Qin, F., Li, B., Yu, Y., Li, C.: Hot Deformation Behavior and Microstructure Evolution of Ti–6Cr–5Mo–5V–4Al–1Nb Alloy. Crystals (Basel). 13, (2023). https://doi.org/10.3390/cryst13020182
29. Darvell, B.W.: Chapter 19 - Casting Alloys. In: Darvell, B.W. (ed.) Materials Science for Dentistry (Tenth Edition). pp. 499–514. Woodhead Publishing (2018)
30. Ferreira, R., Silva, E., Nascimento, C., Rodrigues, S., Aranas Jr., Leal, V., Reis, G.: Thermomechanical Behavior Modeling of a Cr-Ni-Mo-Mn-N Austenitic Stainless Steel. In: Materials Sciences and Applications. pp. 803–822 (2016)
31. Xiong, Zhi-ping & Kostryzhev, Andrii & Stanford, N.E. & Pereloma, E.. Microstructures and mechanical properties of DP and TRIP steels after laboratory simulated strip casting. (2014).
32. Petzow, G.: Metallographisches, keramographisches, plastographisches Ätzen. Gebrüder Borntraeger Berlin, Stuttgart (1994)
33. Lehto, P., Remes, H., Saukkonen, T., Hänninen, H., Romanoff, J.: Influence of grain size distribution on the Hall–Petch relationship of welded structural steel. Materials Science and Engineering: A. 592, 28–39 (2014). https://doi.org/https://doi.org/10.1016/j.msea.2013.10.094
34. Arh, B., Tehovnik, F., Vode, F.: Transformation of the δ-Ferrite in SS2343 Austenitic Stainless Steel upon Annealing at 1050 °C, 1150 °C and 1250 °C. Metals (Basel). 11, (2021). https://doi.org/10.3390/met11060935
35. Struers: Metallic Preperation of Stainless Steel. (2016)
36. Di Schino, A.: Manufacturing and Applications of Stainless Steels. Metals (Basel). 10, (2020). https://doi.org/10.3390/met10030327
37. Kah, P., Layus, P., Martikainen, J.: Influence of alloying elements on the low-temperature properties of steel. Presented at the April (2015)
38. Ahssi, M.A.M., Erden, M.A., Acarer, M., Çuğ, H.: The Effect of Nickel on the Microstructure, Mechanical Properties and Corrosion Properties of Niobium–Vanadium Microalloyed Powder Metallurgy Steels. Materials. 13, (2020). https://doi.org/10.3390/ma13184021
39. Wegertseder GmbH: Zusammensetzung von Edelstählen
40. Joy, D.: The aberration corrected SEM. In: AIP Conference Proceedings. pp. 107–127 (2007)

9. Appendix

9.1. List of abbreviations

AISI American iron steel institute

TMW. Thermo Mechanical Welding

DRX: Dynamic recrystallization

DDRX: Discontinuous dynamic recrystallization

CDRX: Continuous dynamic recrystallization

GDRX: Geometric dynamic recrystallization

DRV: Dynamic recovery

TMP: Thermo-mechanical processes

SFE: Stacking fault energy

FCC: Face centered cubic

BCC: Body centered cubic

V2A: Versuchsschmelze 2 Austenit

OPS: Oxid polishing suspension

EBSD: Electron backscatter diffraction

SEM: Scanning electron microscope

LOM: Light optical microscope

EBW: Electron beam welding

SIBM: Strain induced boundary migration

9.2. List of Figures

9.3. List of tables

Material investigation

Austenitic Stainless Steel - Production

Stainless steel is produced in a two-stage process. First scrap and alloys are melted in an electric arc furnace. Included in the first step is also argon oxygen decarburization (AOD) whereby the carbon content can be adjusted, and impurities can be removed. In the second stage, the molten material is brought into basic mill forms. For example, sheets, stripes, plates or bars. The raw material can then be processed and is used in areas such as the pulp and paper industry, electrical power plants, for furnance parts and many more. (ASM International (2000), p.1f).

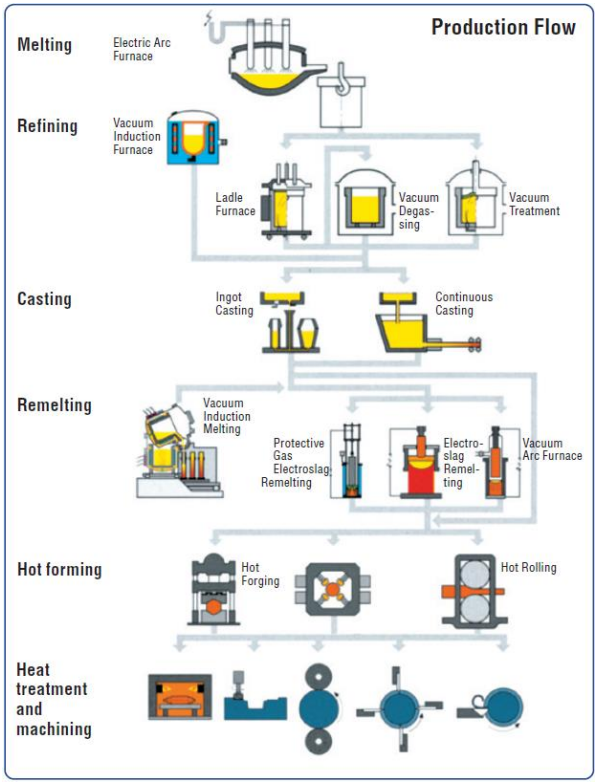

Figure 66: Production Flow of Stainless steel [35]

In addition, there is a secondary steel making process in which the previously produced ingots are melted again in a furnace. This is done first in a vacuum induction furnace and then vacuum arc remelting or electroslag remelting. This additional process step is carried out in order to remove the impurities and thus to obtain steels of high quality [35].

Stainless steels are notable for their good weldability, formability, work hardening and corrosion resistance [36].

Effect of alloys on the structure and the properties

Different alloying elements have different influences on the steel. The combination of different alloying elements results in different steel grades [1].

A few possible alloys used and their impact on the steel:

- **Carbon:**

Carbon plays a decisive role as an alloying element in the alloying of steel, as the percentage content of carbon has a significant influence on the notched impact strength, tensile strength and hardness of the steel.

Steels with a higher carbon content are characterized by increased hardness, but at the same time have a lower notched impact strength.however, the strength is reduced. A carbon content of more than 0.3 % leads to unweldability and increased brittleness of the steel [37]:

- **Managnese:**

The addition of manganese to steel serves to improve the hot forming properties and increase strength, toughness, hardenability and wear resistance. Like nickel, manganese is an element that promotes the formation of γ-austenite.

- **Nickel:**

Nickel acts as an austenite stabilizer, expanding the austenite region and reducing the ferrite region in the steel. These properties lead to improved corrosion and oxidation resistance at elevated temperatures. By refining the grain size, nickel also helps to increase the toughness and strength of the material [38]:

- **Chromium:**

As an alloying element, chromium is responsible for the corrosion resistance of stainless steels. Therefore, stainless steels are by definition those alloyed with at least 13% chromium by mass. In fact, the alloying element chromium in this minimum proportion leads to the formation of a very thin but firmly adhering chromium oxide layer, which protects the underlying metal from attack by the surrounding media [39].

Types of stainless steel

Stainless steels can be classified as following:

- **Austenitic:**

More than two thirds of stainless steels are austenitic stainless steels. Alloying with nickel and/or manganese and nitrogen gives this steel its austenitic microstructure. This austenitic microstructure gives the steel the property that the microstructure remains an austenitic microstructure at all temperatures from the cryogenic region to the melting temperature.

The metal can be strengthened by cold forming but due to the unchanging microstructure at high temperatures the steel is not hardenable by heat treatment.

Austenitic steels can be divided into groups:

  - Stainless steels that get their austenitic microstructure due to nickel addition. These steels are in the 300 series.

    The best known austenitic stainless steel of the 300 series is the type 304 with a composition of 18% chromium and 8% or 10% of Nickel. This steels also has a low carbon version 304L which is used in the experimental part of the thesis.

It prevents corrosions problems during the welding process and The “L” in 304L symbolizes the low carbon version where the alloy is below 0,03%.

- Stainless steel that gets their austenitic microstructure due to manganese and nitrogen instead of nickel. These steels are in the 200 series.

- **Ferritic:**

Consists of a ferritic microstructure and contains between 10,5% and 27% chromium with a low amount of nickel. Also, ferritic steels are not hardenable by heat treatment. As like austenitic steels the microstructure doesn’t change at low or high temperatures and ferritic stainless steel also can’t be hardened by cold working in such a extend as it is possible with austenitic stainless steel. Due to the microstructure of ferrite, it is magnetic. Due to microstructural problems during the welding process of ferritic steels only allows thin walled vessels or tanks. An increased content of chromium and molybdenum improves corrosion resistance, which is also typical of austenitic stainless steels. However, this high alloy composition leads to the formation of an intermetallic phase during welding, which results in increased brittleness.

- **Martensitic:**

The ferromagnetic steel is mainly used as tool steel. Due to its composition of 12-15% chromium, 0.2-1% molybdenum and 0.1-1% carbon, it is a very creep resistant steel. Due to its ferromagnetic properties, the magnetic properties can adapt to the properties of the given magnetic field.

- **Duplex:**

Is a mixture of ferritic and austenitic steels with a high chromium content of 19% to 32%, a molybdenum content of 5% and a lower nickel content then austenitic stainless steel. They have a very high strength, improved resistance to chloride stress corrosion cracking [13].

Scanning Electron Microscopy

In the next step, but no longer within the scope of this work, the remaining grain size measurements were to be carried out using ebsd.

Scanning Electron Microscopy (SEM) uses a focused electron beam to generate a topographical image, to give insight into the chemical composition, to give information about the electrical behavior and the crystalline structure of a conductive specimen under investigation (Cf. Vernon-Parry 2000, p.1). The electron beam is focused on the bulk sample, where the electrons hit the atoms of the sample. Secondary electrons (SE) as well as backscattered electrons (BSE) are leaving the sample. These are captured by a detector and then displayed as an image.

In addition, X-rays are generated which provide information about the chemical composition of the observed material [1].

Sample-Electron Beam Interaction

Electrons collide with the sample and interact with the outer shell electrons which have similar energies or with the nucleus of an atom. Elastic or inelastic scattering can occur.

- **Elastic interactions**
  Incoming electrons which are deflected by the atomic nucleus or outer shell electrons with similar energy are elastically scattered. During this scattering process, a negligible amount of energy is lost. Incident electrons from the electron beam that are deflected over an angle of 90° are called backscattered electrons. (Cf. Zhou W., Apkarian R.P., Wang Z.L., Joy D (n.d.), p.2f)
- **Inelastic interactions**
  Inelastic scattering occurs, due to interactions with the incoming electrons from the beam and the sample. In inelastic scattering energy transfer between the electrons of the electron beam and the electrons of the sample occurs. The energy of the beam electrons is transferred to the energy of the atom. Due to that energy transfer the sample gets ionized and therefore the atom gets excited. Secondary electrons are generated. These electrons can be used to image or analyze the sample. (Cf. Zhou W., Apkarian R.P., Wang Z.L., Joy D (n.d.), p.3)

Secondary electrons, backscattered electrons, auger electrons, characteristic X-rays and other electrons can be released from the sample.
The signal received by the detector depends on the atomic number of the sample and the electron acceleration of the incoming beam. The signal is stronger with increasing electron acceleration and with decreasing atomic number. The higher the acceleration voltage, the deeper the electrons from the electron beam penetrate into the sample. If this is too high, no useful signal can be achieved. (Cf. Zhou W., Apkarian R.P., Wang Z.L., Joy D (n.d.), p.2f)

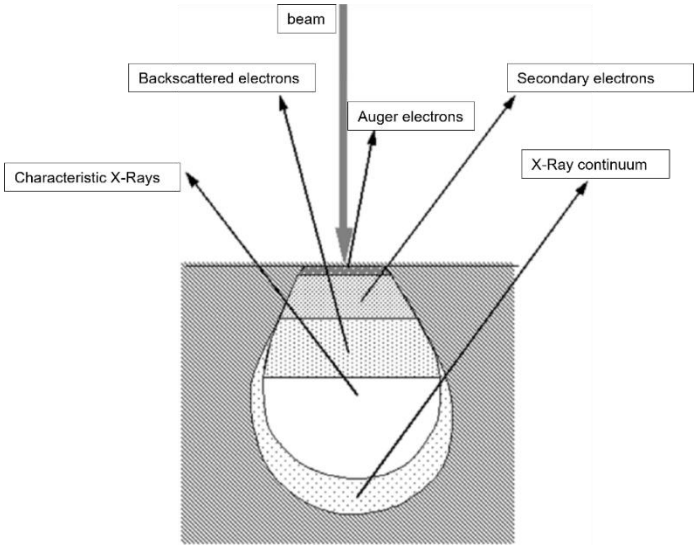

Figure 67: (Zhou W., Apkarian R.P., Wang Z.L., Joy D (n.d.), p.2f) Electron - matter interactions

- **Secondary Electrons (SE)**

For imaging samples in SEM the most frequently used mode uses low-energy secondary electrons. As already mentioned electrons from the incoming beam are scattering into the first few nanometres of the sample and interact with the electrons of the atoms. Also, secondary electrons can be released by the interaction between high-energy backscattered electrons and the atom and due to the interaction between the high-energy backscattered electrons and objects in the specimen chamber [1].

- **Backscattered Electrons (BSE)**

Back scattered electrons are generated due to elastically scattering on the atomic nuclei of the atoms of the sample. The incoming electrons get deflected by the atoms of the sample surface. If there is a material with a high atomic number, the image looks brighter in comparison with materials with low atomic numbers.

- **X-Ray emission**

When high-energy electrons interact with electrons from the inner shells, the electrons from the inner shell can be kicked out. Electrons from outer orbitals may fall into inner orbitals to re-establish charge balance. Ionization occurs. The ionized atom returns to the ground state by emission of an X-ray photon. In SEM this microanalytical technique is used to provide chemical information about a sample. Further Bremsstrahlung is emitted which emits a characteristic background noise by decelerated electrons when they interact with the electron cloud. (Cf. Zhou W., Apkarian R.P., Wang Z.L., Joy D (n.d.), p.7f)

SEM Structure

A SEM consists of several components that focus the high energy electron beam onto the workpiece.

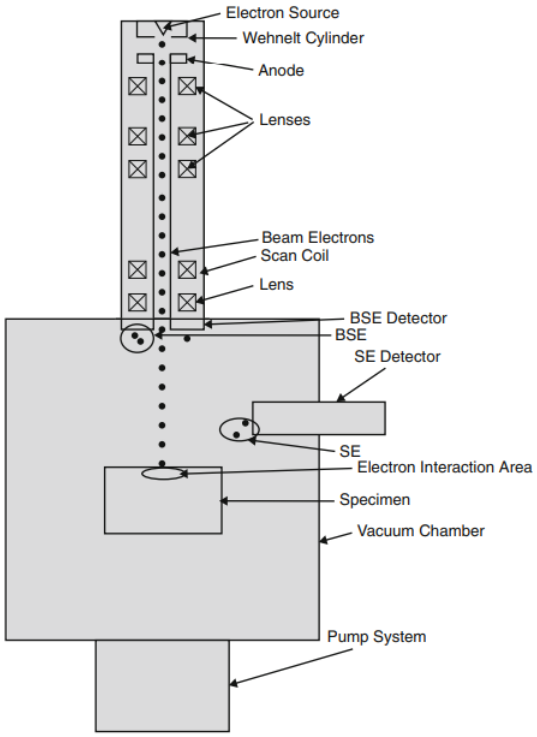

Figure 68: Scanning Electron Microscope [1]

- **Electron gun**

In SEM a stable electron beam with high current, small spot size, adjustable energy and small energy dispersion is needed.

  - **Tungsten Electron gun**

To generate the electron beam, the anode, cathode and the Wehnelt cylinder are necessary. In the anode the electrons from the tungsten filament are released by applying a heating voltage. More than 2800K are needed, so that the electrons can escape from the material. The higher the filament current the more electrons are released from the filament. This is possible until a certain saturation point is reached. Above this point the emission only increases slightly. An accelerating voltage between the anode and the cathode accelerates the electrons towards the cathode. This voltage is between 0,1 and 30 kV. The electron beam trajectories from the filament tip is controlled by the Wehnelt cylinder. A coarse focusing of the electron beam is realized by a small negative bias between the anode and the Wehnelt cylinder [40].

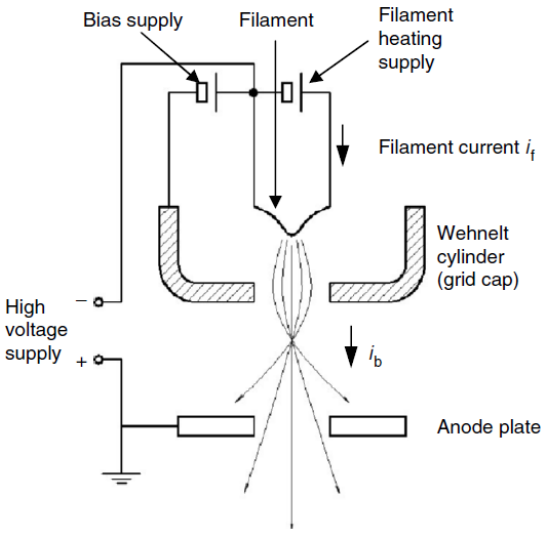

Figure 69: Electron gun [40]

- **Magnetic Lens**

In order to focus and indicate the direction of the electron beam electron lenses are used (Cf. ebd. 2019, p.1505).

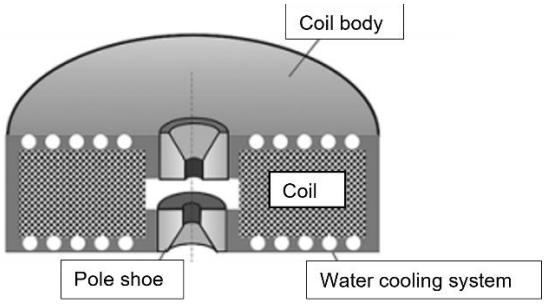

Figure 70: Electron Lens

The coil current can be up to 30 A. Due to the water cooling a constant temperature is achieved. The pole shoe shapes and concentrates the magnetic field.

To get the focused as wished all electrons, which are not pass trough the center of the axis of the lens need to experience a force that will lead them to this. This force is called Lorenz Force.

$$F = -e * v \times B$$

-e represents the electron with the charge -e. F is the force, v is the speed and B is the magnetic induction. The formular indicates the direction of the Lorenz force F on an electron with the charge -e, which moves with a speed v in a magnetic field with the induction B. It is strong near the lens border and there is no force at the centre of the lens.

To bring the specimen into focus, the magnetic field must be adjusted accordingly.

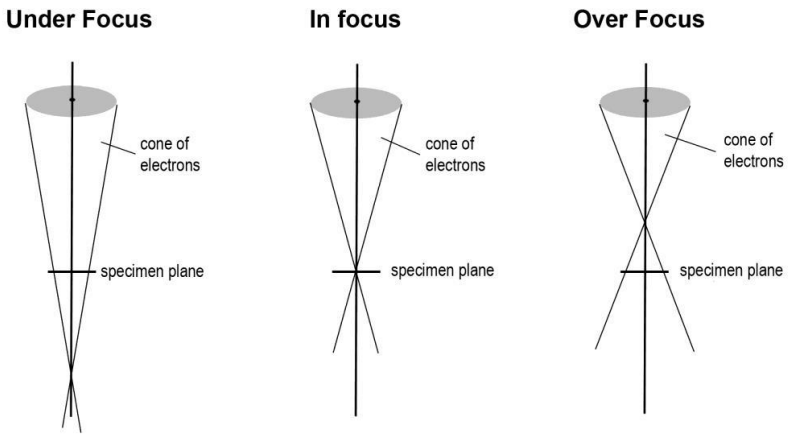

Figure 71: [3]Focus

If the magnetic field is too weak, the beam is under focused. However, if the magnetic field is too strong, the focus will be below the specimen. The magnetic field must therefore be adjusted in such a way that the focus lies exactly on the specimen plane. Furthermore, there are lens aberrations with electron lenses. In this thesis, spherical aberration, chromatic aberration, and astigmatism are discussed

- **Spherical aberration**

If the field homogeneity does not meet the requirements, the spherical aberration occurs. The weaker the rotationally symmetric magnetic field, the greater the deviation from the desired result [2].

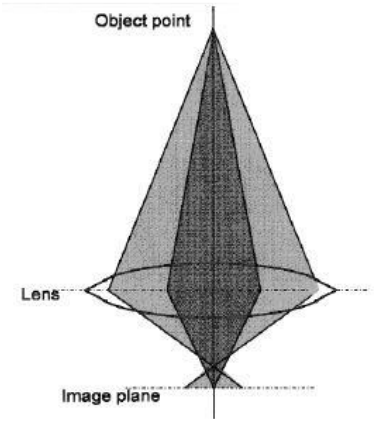

Figure 72: (Cf. Joy D.C. 2005, p.537) Spherical Aberration

It occurs because the focus of the electron is not on the image plane but on a point, which is further away from it [40].

- **Chromatic aberration**

The electron beam of the electron source is not always mono energetic. Due to temperature changes of the energy of the electrons occurs.

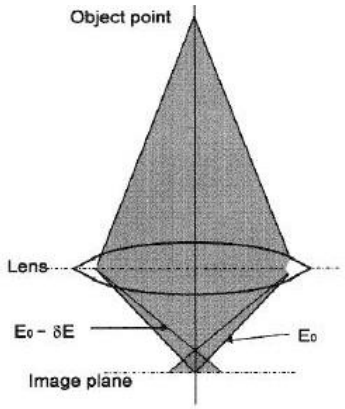

Figure 73: Chromatic Aberration [40]

Chromatic aberration occurs because the focal length of the objective lens is changing with the energy of the electrons. The focal length is getting longer when high energies occur und smaller for small energies (Cf. Joy D.C. 2005, p. 536).

Change of properties of the material during SRX

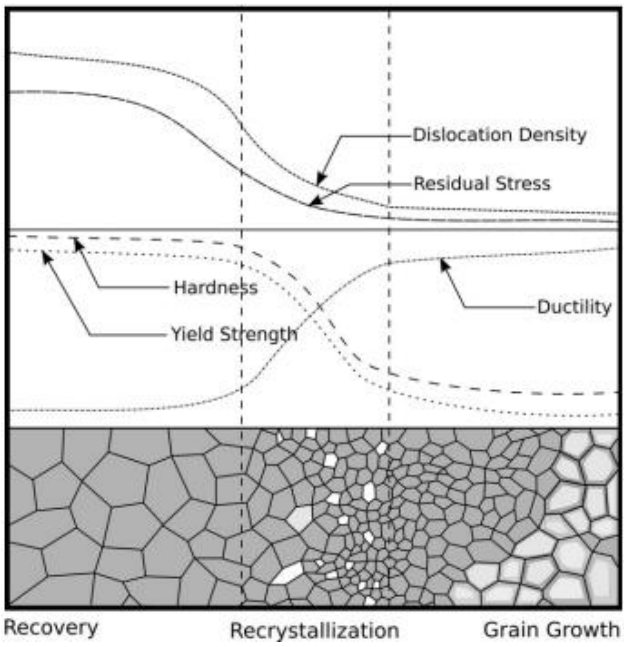

Figure 74: Change of properties between recovery, recrystallization and grain growth [11]

Figure 74 describes the change in the properties of a material due to recrystallization. Since the recrystallization process occurs in areas with high dislocations, recrystallization and grain growth lead to a reduction in these dislocations. The residual stress in the material also decreases during the processes. This is accompanied by an increase in ductility due to the decrease in dislocation density and residual stress. Hardness and yield strength drop sharply due to recrystallization [11].

Flow stress data

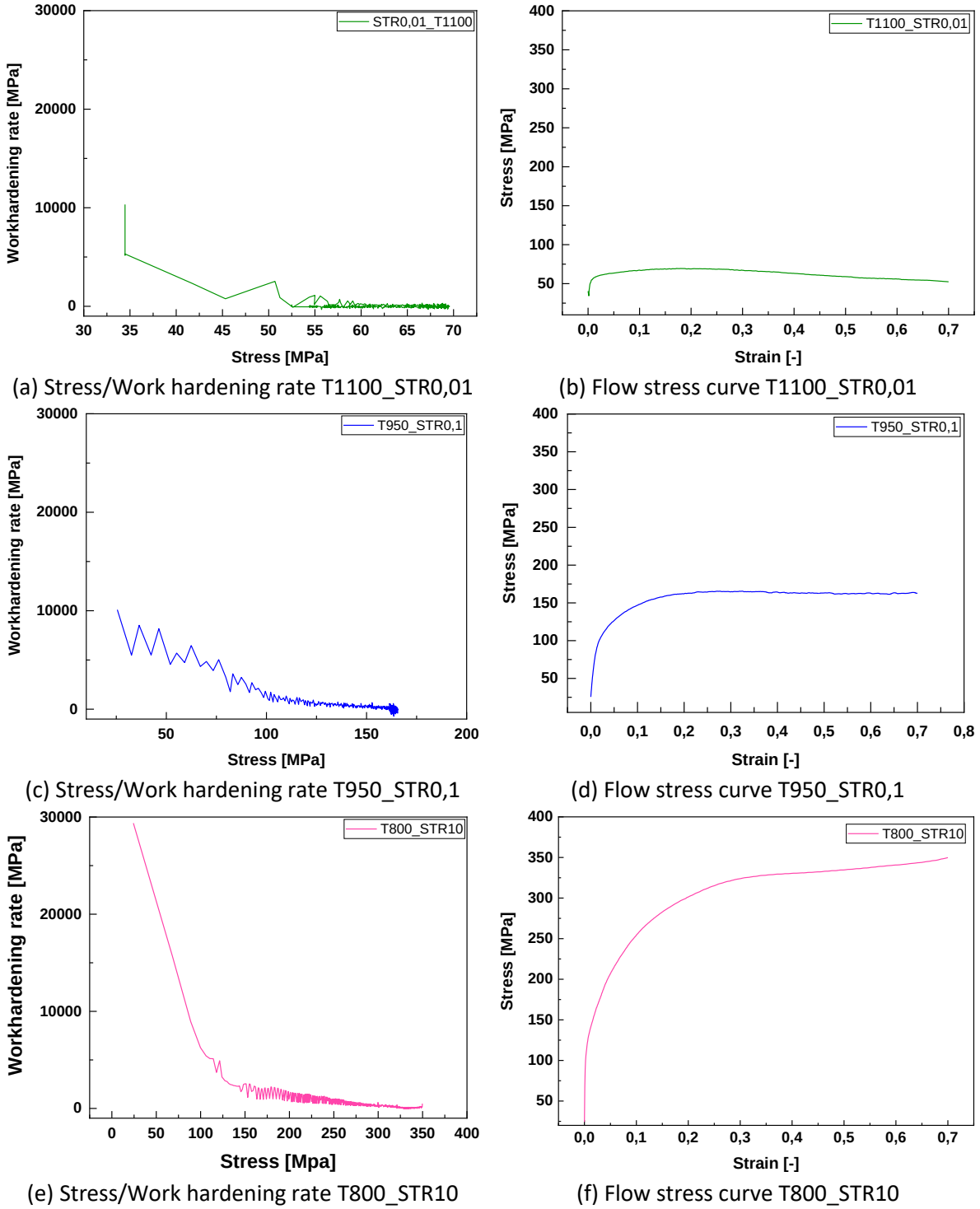

Figure 75: Stress/Work hardening rate curves

Figure 75 shows the progression of the work hardening rate in relation to the applied stress. In Figure 75a, you can see that the work hardening rate increases up to about 69 MPa. Figure 75b shows that the peak of the stress can be found at around this value. After that, the work hardening rate and the stress decrease again. It can be seen that the recrystallization in this area of the diagram is higher than the dislocation formation due to work hardening.

Figure 75d shows that the flow stress curve is quite constant after the peak. Here, recrystallization and work hardening roughly balance each other out. Figure 75c reflects this behavior.

Figure 75e shows the curve with a continuously increasing flow stress curve.

Figure 76shows the different flow stress curves at different strain rates at one temperature.

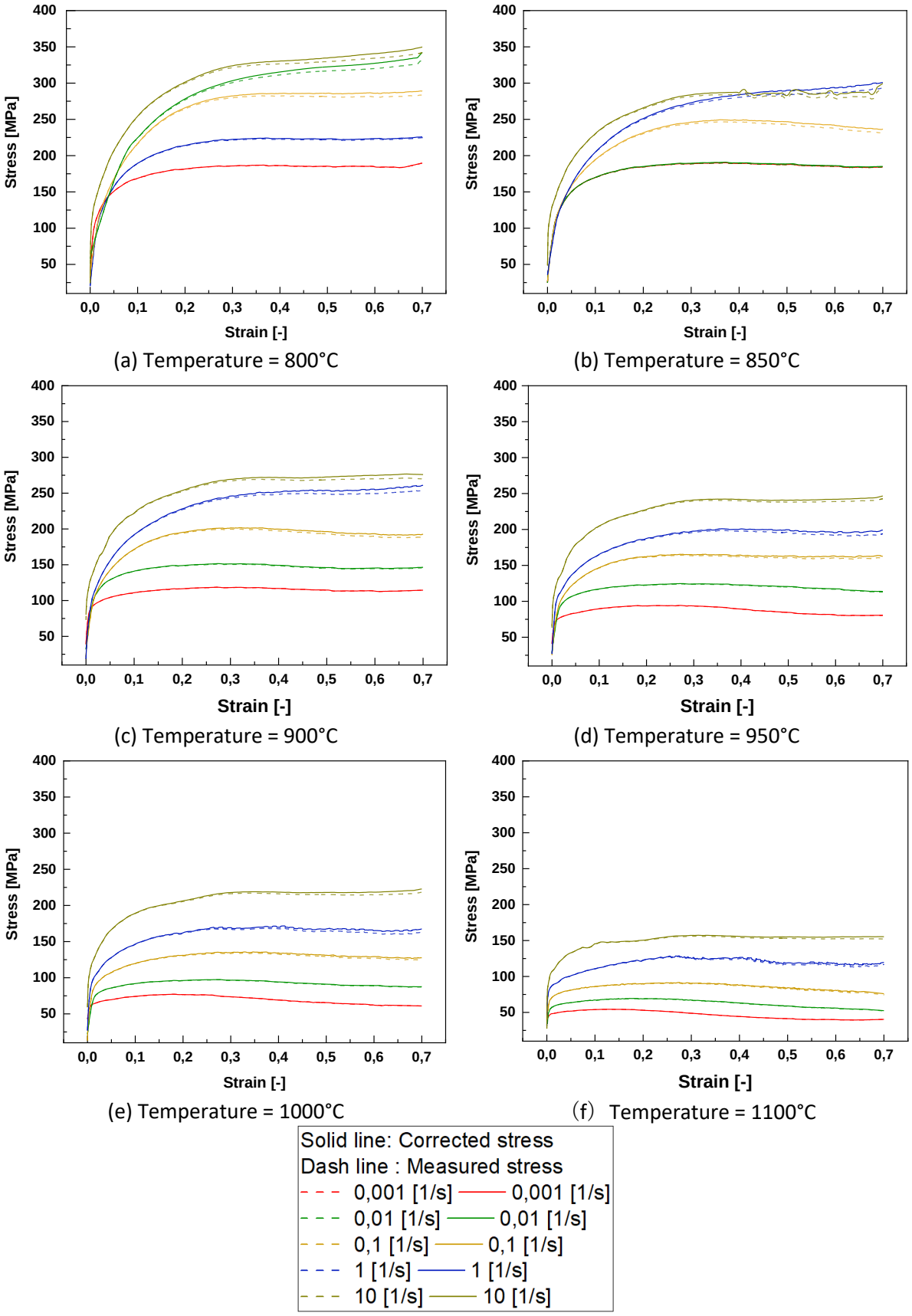

Figure 76:Measured and adiabatically corrected flow stress curves at different temperatures

Here, too, it can be seen that the flow stress curves are higher at lower temperatures than for flow stress curves that were compressed at a higher temperature. Figure 76a shows that the

value for the strain rate is 0.01 s^{-1} too high. Figure 76b also shows that the value for a strain rate of 1 s^{-1} is too high. This exceeds the flow stress curve, which was measured for a strain rate of 10 s^{-1}. The flow stress curves for the strain rates 0.001 s^{-1} and 0.01 s^{-1} also overlap.

These errors could be due to a faulty hot compression test.

Grain size histograms

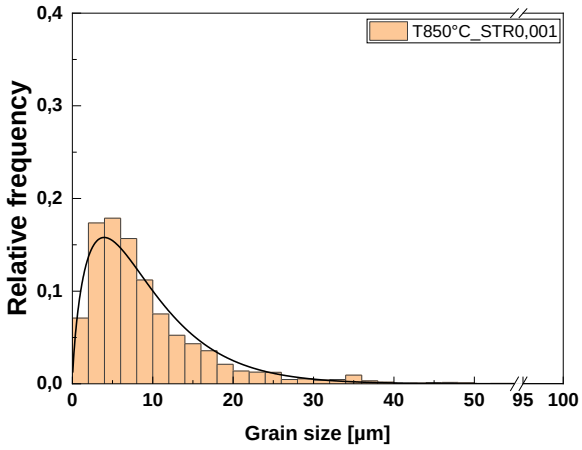

(a) Average grain size T850_STR0,001

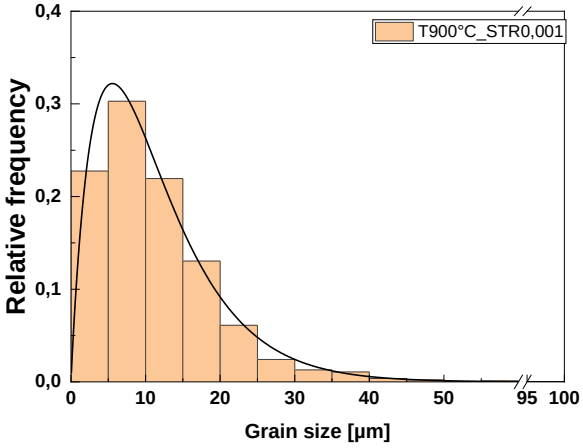

(b) Average grain size T900_STR0,001

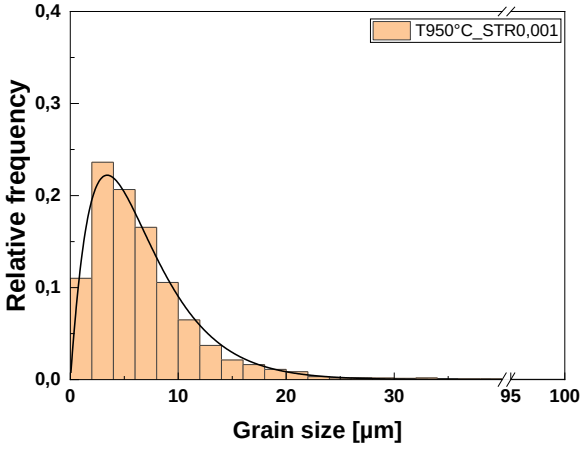

(c) Average grain size T950_STR0,001

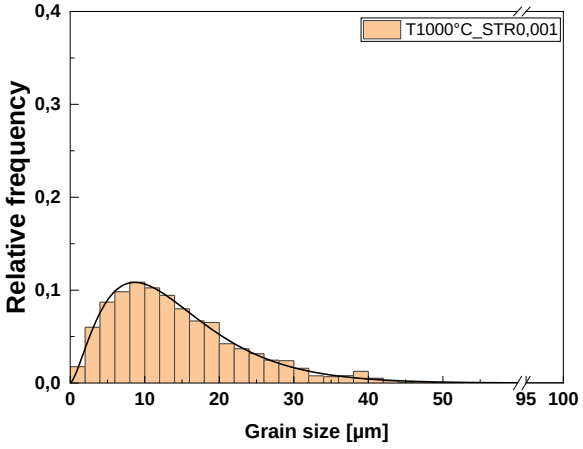

(d) Average grain size T1000_STR0,001

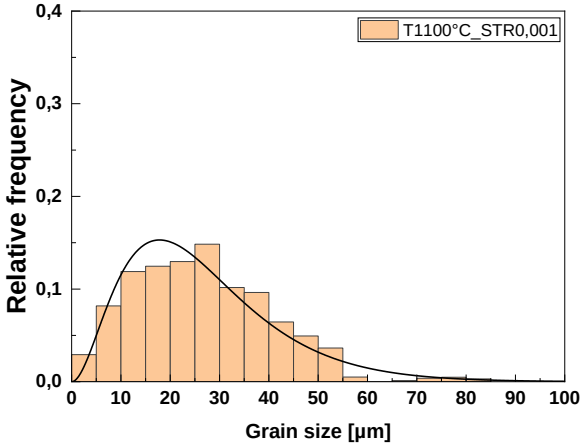

(e) Average grain size T1100_STR0,001

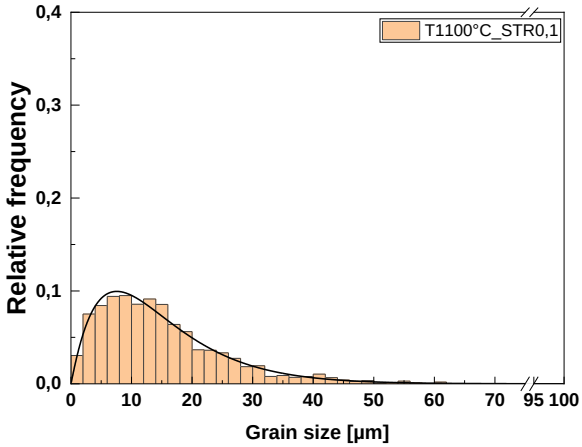

(a) Average grain size T1100_STR0,1

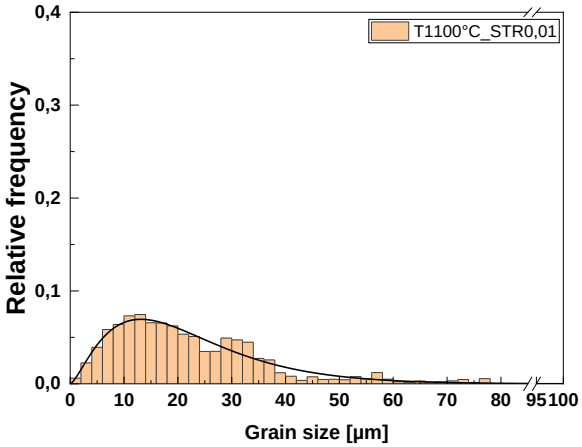

(b) Average grain size T1100_STR0,01

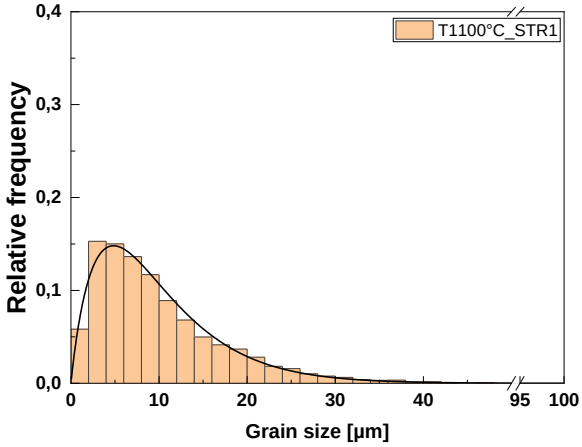

(d) Average grain size T1100_STR1

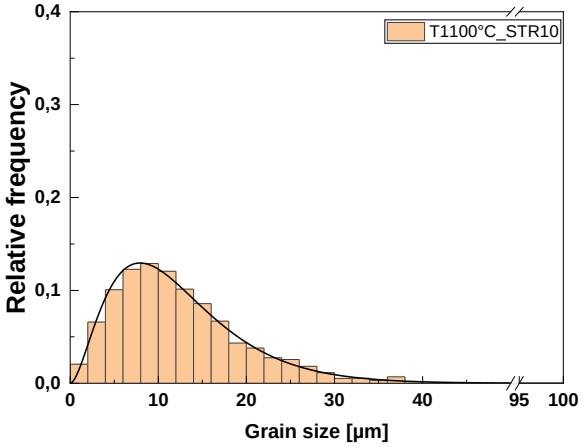

(e) Average grain size T1100_STR10

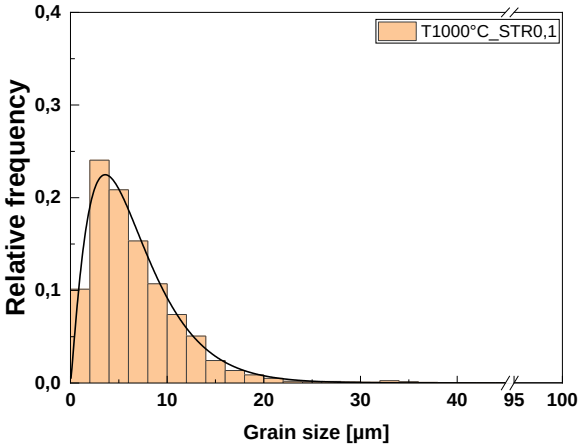

(c) Average grain size T1000_STR0,1

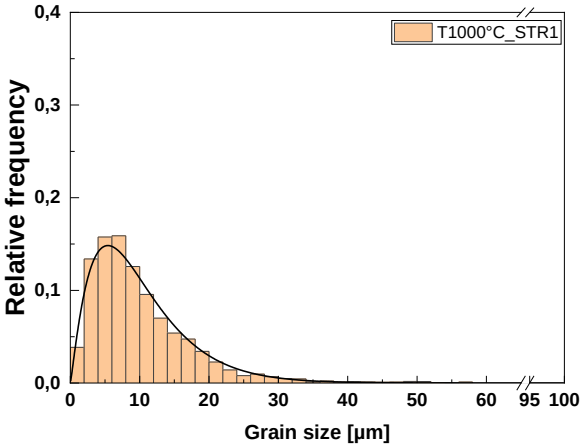

(d) Average grain size T1000_STR1

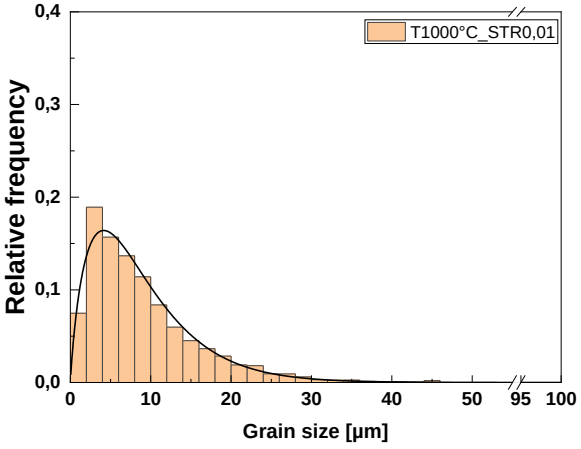

(e) Average grain size T1000_STR0,01

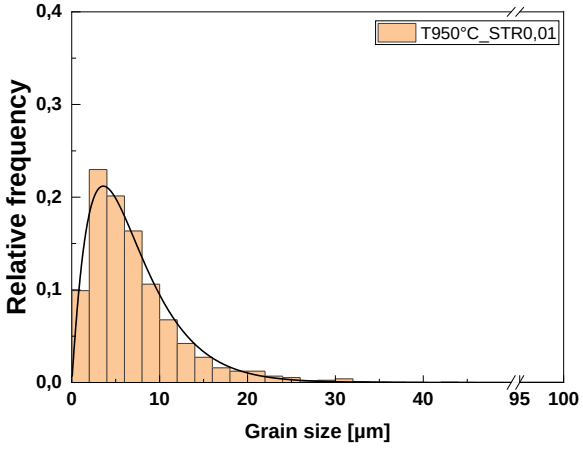

(f) Average grain size T950_STR0,01

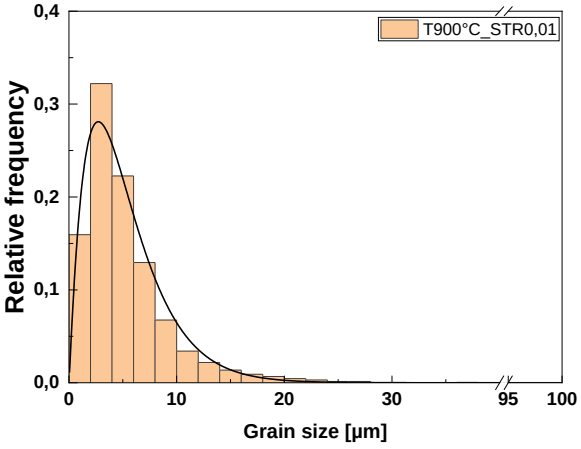

(g) Average grain size T900_STR0,01